

C3N5: A Low Bandgap Semiconductor Containing an Azo-linked Carbon Nitride Framework for Photocatalytic, Photovoltaic and Adsorbent Applications

Pawan Kumar, Ehsan Vahidzadeh, Ujwal Kumar Thakur, Piyush Kar, Kazi Mohammad Alam, Ankur Goswami, Najia Mahdi, Kai Cui, Guy M Bernard, Vladimir K. Michaelis, and Karthik Shankar

J. Am. Chem. Soc., **Just Accepted Manuscript** • DOI: 10.1021/jacs.9b00144 • Publication Date (Web): 14 Feb 2019

Downloaded from <http://pubs.acs.org> on February 14, 2019

Just Accepted

"Just Accepted" manuscripts have been peer-reviewed and accepted for publication. They are posted online prior to technical editing, formatting for publication and author proofing. The American Chemical Society provides "Just Accepted" as a service to the research community to expedite the dissemination of scientific material as soon as possible after acceptance. "Just Accepted" manuscripts appear in full in PDF format accompanied by an HTML abstract. "Just Accepted" manuscripts have been fully peer reviewed, but should not be considered the official version of record. They are citable by the Digital Object Identifier (DOI®). "Just Accepted" is an optional service offered to authors. Therefore, the "Just Accepted" Web site may not include all articles that will be published in the journal. After a manuscript is technically edited and formatted, it will be removed from the "Just Accepted" Web site and published as an ASAP article. Note that technical editing may introduce minor changes to the manuscript text and/or graphics which could affect content, and all legal disclaimers and ethical guidelines that apply to the journal pertain. ACS cannot be held responsible for errors or consequences arising from the use of information contained in these "Just Accepted" manuscripts.



C₃N₅: A Low Bandgap Semiconductor Containing an Azo-linked Carbon Nitride Framework for Photocatalytic, Photovoltaic and Adsorbent Applications

Commented [A1]: We modified the manuscript title slightly in response to the suggestion from Reviewer#1.

Pawan Kumar,^{1*} Ehsan Vahidzadeh,¹ Ujwal K. Thakur,¹ Piyush Kar,¹ Kazi M. Alam,¹ Ankur Goswami,¹ Najia Mahdi,¹ Kai Cui,² Guy M. Bernard,³ Vladimir K. Michaelis³ and Karthik Shankar^{1*}

¹*Department of Electrical and Computer Engineering, University of Alberta, 9211 - 116 St, Edmonton, Alberta, Canada T6G 1H9*

²*Nanotechnology Research Centre, National Research Council of Canada, Edmonton, Canada T6G 2M9*

³*Department of Chemistry, University of Alberta, Edmonton, Alberta, Canada, T6G 2G2*

*Email: Pawan Kumar (pawan@ualberta.ca); Karthik Shankar (kshankar@ualberta.ca)

Abstract

Modification of carbon nitride based polymeric 2D materials for tailoring their optical, electronic and chemical properties for various applications has gained significant interest. The present report demonstrates the synthesis of a novel modified carbon nitride framework with a remarkable 3:5 C:N stoichiometry (C₃N₅) and an electronic bandgap of 1.76 eV, by thermal deammoniation of melem hydrazine precursor. Characterization revealed that in C₃N₅ polymer, two *s*-heptazine units are bridged together with azo linkage, which constitutes an entirely new and different bonding fashion from g-C₃N₄ where three heptazine units are linked together with tertiary nitrogen. Extended conjugation due to overlap of azo nitrogens and increased electron density on heptazine nucleus due to the aromatic π network of heptazine units lead to an upward shift of the valence

band maximum resulting in bandgap reduction down to 1.76 eV. XRD, He-ion imaging, HR-TEM, EELS, PL, fluorescence life-time imaging, Raman, FTIR, TGA, KPFM *etc* clearly show that the properties of C₃N₅ are distinct from pristine carbon nitride (g-C₃N₄). When used as an electron transport layer (ETL) in MAPbBr₃ based halide perovskite solar cells, C₃N₅ outperformed g-C₃N₄, in particular generating an open circuit photovoltage as high as 1.3 V, while C₃N₅ blended with MA_xFA_{1-x}Pb(I_{0.85}Br_{0.15})₃ perovskite active layer achieved a photoconversion efficiency (PCE) up to 16.7 %. C₃N₅ was also shown to be an effective visible light sensitizer for TiO₂ photoanodes in photoelectrochemical water splitting. Due to its electron-rich character, the C₃N₅ material displayed instantaneous adsorption of methylene blue from aqueous solution reaching complete equilibrium within 10 min, which is significantly faster than pristine g-C₃N₄ and other carbon-based materials. C₃N₅ coupled with plasmonic silver nanocubes promotes plasmon-exciton co-induced surface catalytic reactions reaching completion at much low laser intensity (1.0 mW) than g-C₃N₄ which showed sluggish performance even at high laser power (10.0 mW). The relatively narrow bandgap and 2D structure of C₃N₅ make it an interesting air-stable and temperature-resistant semiconductor for optoelectronic applications while its electron-rich character and intra-sheet cavity make it an attractive supramolecular adsorbent for environmental applications.

KEYWORDS: carbon nitride, melem, *s*-heptazine, dye adsorption, photocatalysis, water splitting, solar cells, plasmonic photocatalysis.

Formatted: Highlight

1. Introduction

The last few decades have witnessed the rise of semiconducting, all-organic polymers as excellent metal-free and visible light-active materials for various optoelectronic and energy harvesting applications.¹ Although impressive improvements in performance have been achieved, particularly

for plastic solar cells, the synthesis procedures for semiconducting polymers are cumbersome and difficult to scale up,² and the organic semiconductors themselves are unstable under the action of heat, light and/or ambient air.³ Consequently, there are scalability concerns related to semiconducting polymers,⁴ and requirement of heavy encapsulation to achieve even modest durability in the photovoltaic application. The same concerns, related to oxidative stability and durability, have also ruled out the use of semiconducting polymers in photocatalytic applications.

A very different approach toward forming and exploiting all-organic, polymeric semiconductors in optoelectronic and energy harvesting applications consists of using doped and substituted graphenic frameworks as building blocks to achieve two-dimensional (2D) semiconductors with well-defined bandgaps and structural motifs.^{5, 5-6} The major advantages of graphenic semiconductors are their chemical robustness, and the simplicity of synthesis. Several graphenic semiconductors are synthesizable using solvothermal synthesis and/or solid-state reactions, and graphenic semiconductors are perfectly stable in ambient conditions up to temperatures of several hundred degrees Ceelsius. As a result of this exceptional stability, almost no structural or chemical degradation of photocatalytic action is observed even after several re-use cycles.⁷

Among graphenic semiconductors, graphitic carbon nitride (g-C₃N₄), composed of tris-*s*-triazine (*s*-heptazine, C₆N₇) units bridged together with nitrogen atoms to give a 2D graphitic structure has gained significant interest due to its astonishing electronic, optical, and physicochemical properties.⁸ Continuous repetition of the heptazine motif leads to a bandgap- of 2.7 eV with band edge positions (E_{CB}, -1.1 eV and E_{VB}, +1.6 eV) that render it compatible with sunlight-driven water splitting, CO₂ photoreduction and the photooxidation of a number of organic compounds.⁹ Further, the plentiful presence of electron rich sites and basic nitrogens in the g-C₃N₄ scaffold

enables the promotion of various catalytic reactions *i.e.* alkylation, esterification, oxidation, *etc* and pollutant removal (dye adsorption).^{6a, 10} The somewhat wide bandgap of g-C₃N₄ means that it can absorb only the ultraviolet and blue fraction of solar spectrum ($\lambda < 450$ nm) which limits its performance in photocatalytic and photovoltaic applications. Doping with various heteroatoms such as P, F, B, and S has been utilized to improve the visible light absorption profile and photoefficiency.¹¹ Like all semiconductors, g-C₃N₄ suffers the innate drawback of carrier recombination detrimental to catalytic and photocatalytic processes. Many surface modification approaches such as increasing the surface area *via* soft and hard templating, using two or more precursors, transformation of bulk material into sheets, doping with metals (Ag, Cu, Rh, Pt, Na, *etc*) and metal oxides (CoO_x) for electron and hole capture, coupling with other semiconductors/metal complexes to form heterojunctions, and blending with graphene have been employed to improve the photocatalytic and catalytic performance of g-C₃N₄.¹² However, less attention has been paid to chemical structure modification which can lead to the generation of a more robust, band edge tuned g-C₃N₄ framework with entirely new physicochemical properties for efficient catalytic/photocatalytic applications. It has been found that addition of extra nitrogen-rich moieties in the g-C₃N₄ scaffold to increase the N:C ratio from 4:3 ratio in CN can reduce the bandgap significantly, due to a more extended conjugated network and the participation of the lone pair on the N atom with the π conjugated system of heptazine motif. Vinu et al. demonstrated the synthesis of N-rich carbon nitride (MCN-8) using 3-amino-1,2,4-triazole to afford C₃N₅ stoichiometry resulting in a significant decrease in bandgap (2.2 eV) due to extended conjugation.¹³ However, this increase in N:C ratio to 5:3 (from the 4:3 ratio in g-C₃N₄) was due to the presence of the N-rich 1,2,4-triazole moiety linked to the heptazine motif and not because of the direct incorporation of the extra N atom in the heptazine nucleus. The same group has also

reported the synthesis of mono/and di-amino-s-tetrazine based carbon nitride materials (i.e. MCN-ATN, MCN-4, and MCN-9) with C_3N_5 to C_3N_6 stoichiometry using 3-amino-1,2,4-triazine/aminoguanidine hydrochloride precursor and SBA-15/KIT-6 templating material.¹⁴ The N rich 1,2,4-triazine or 1,2,4,5-tetrazine moieties were bridged together with tertiary nitrogen in a similar fashion to triazine-based carbon nitride and a significant decrease in band gap was observed due to the addition of extra nitrogens. In a recent report, mesoporous triazole and triazine framework modified carbon nitride materials with $C_3N_{4.8}$ empirical formula synthesized by using 5-amino-1H-tetrazole (5-ATTZ) precursor and their hybrid with graphene displayed excellent performance in the oxygen reduction reaction.¹⁵ Fang et al. reported the synthesis of nitrogen self-doped graphitic carbon nitride (C_3N_{4+x}) by heating hydrazine treated melamine in a sealed ampoule. In C_3N_{4+x} , the excess N atoms replace terminal C atoms in the heptazine nucleus and the excess charge on the N atom gets redistributed leading to electron rich heptazine motifs due to which C_3N_{4+x} possessed a narrower bandgap (2.65 eV) with concomitant shifts in the conduction and valence band edge positions (E_{CB} , -0.98 eV and E_{VB} , +1.67 eV).¹⁶ In these N rich carbon nitrides, the N rich triazine or heptazine based unit remains linked together with tertiary nitrogen, $N(C)_3$ and increased stoichiometric N:C ratio was due to the replacement of C via N in triazine or heptazine ring system. Similarly, carbon-rich C_3N_4 network also facilitates bandgap narrowing and efficient charge separation due to the extended conjugated network. Zhang et al. reported the hydrothermal synthesis of low bandgap, C rich C_3N_4 materials with extended conjugated networks using melamine (as heptazine ring source) and glucose (as carbon source) precursors.^{12c, 17} However, the use of melamine and other C and N sources can afford only C_3N_4 structures possessing randomly distributed domains within the C_3N_4 framework due to the uncontrolled reaction and these regions work as trap centers. Melem (2,5,8-triamino-s-heptazine) considered

Formatted: Font: Italic

the smallest monomeric unit of g-C₃N₄ framework, provides the opportunity to manipulate chemical structure by incorporating other units in the C₃N₄ framework in a more controlled fashion.¹⁶⁻¹⁸ Shiraishi *et al.* reported the synthesis of modified CN-polydiimide framework (g-C₃N₄/PDI_x) by solid-state reaction between melem and electron deficient pyromellitic dianhydride (PMDA), and demonstrated that the band edge positions of g-C₃N₄/PDI_x could be tuned by limiting the number of PDI units in the framework.¹⁹ Heterostructured (C_{ring}-C₃N₄) embodiments of conductive, in-plane, π conjugated carbon rings incorporated in the C₃N₄ matrix were prepared by thermal dehydrogenation reaction between glucose and melem, and the obtained C_{ring}-C₃N₄ heterostructure achieved fast spatial charge transfer from g-C₃N₄ to C_{ring} motif facilitating efficient water splitting.^{18d, 20} The replacement of amino functionalities on melem/melamine by nitrogen-rich functionalities *i.e.* azide (-N₃) expedited the synthesis of N-rich carbon nitride *i.e.* 2,5,8-triazido-*s*-heptazine, (C₆N₇)(N₃)₃ which after thermal heating, afforded N-rich carbon nitride.²⁰⁻²¹ Likewise, triazine containing N-rich CN was also synthesized by thermal annealing of 2,4,6-triazido-1,3,5-triazine [cyanuric triazide, (C₃N₃)(N₃)₃].^{20, 22} However, the synthesis procedure involved sodium azide and concomitant shock sensitive explosion hazards; furthermore, azide intermediates are highly undesirable.

Herein, we demonstrated the synthesis of novel modified carbon nitride framework with a C₃N₅ stoichiometry by thermal deammoniation of 2,5,8-trihydrazino-*s*-heptazine, also known as melem hydrazine (MH), as a safe and environmentally benign precursor (Figure 1). The obtained carbon nitride modified framework was denoted as C₃N₅ due to its 3:5 C:N stoichiometric ratio. Characterization studies revealed that the C₃N₅ framework contains heptazine moieties bridged together by azo linkage (-N=N-). The presence of azo linkage extends the π conjugated network due to overlap between the *p* orbitals on N atoms constituting the azo bond and π system of

Formatted: Highlight

heptazine motif which resulted in the reduction of the electronic bandgap to 1.76 eV. C_3N_5 displayed improved photosensitization properties at longer wavelengths for solar water splitting. Further, due to the increased electron charge density on the ring nitrogen, C_3N_5 exhibited instantaneous adsorption of methylene blue from aqueous solution. Solar cell devices fabricated using low band-gap C_3N_5 , as an electron transporting layer (ETL) in $MAPbBr_3$ based perovskite solar cells demonstrated improved power conversion efficiency (PCE), open circuit voltage (V_{oc}) *etc.* compared to solar cells made from g- C_3N_4 based ETL due to tuned band alignment. Blending a small amount of C_3N_5 (4.0 wt%) with $MA_xFA_{1-x}Pb(I_{0.85}Br_{0.15})_3$ perovskite active layer led to an increase in PCE up to 16.68% with V_{oc} of 1.065V and J_{sc} of 22.87 mA/cm^2 higher than conventional and g- C_3N_4 blended solar cell architectures. Compared to g- C_3N_4 , C_3N_5 exhibited a remarkably enhanced performance in the plasmon-exciton co-driven photoreduction of 4-nitrobenzenethiol to 4,4'-dimercaptoazobenzene.

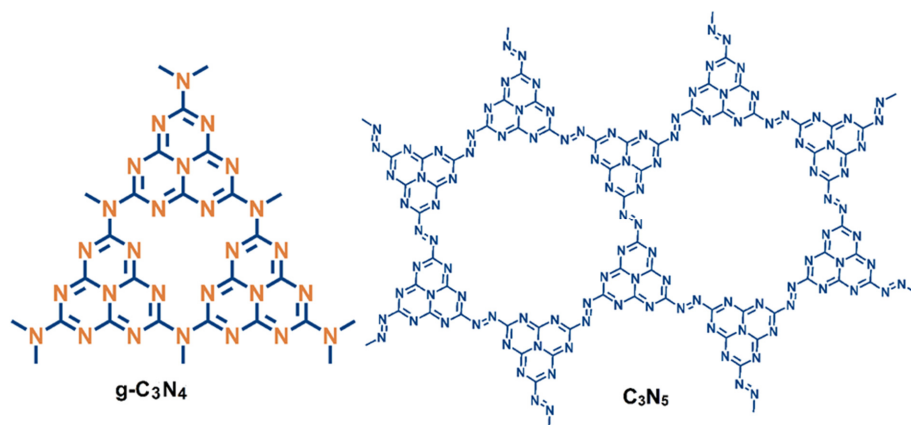


Figure 1. Chemical structure of g- C_3N_4 and carbon nitride modified C_3N_5 framework.

2. Results and discussion

Melem (2,5,8-triamino-*s*-heptazine) served as the precursor monomeric unit for the synthesis of C_3N_5 polymer. Melem was synthesized by heating melamine at 425 °C overnight followed by purification in boiling water. The obtained melem was treated with hydrazine hydrate ($NH_2NH_2 \cdot H_2O$, 55% in water) in an autoclave at 140 °C for 24 h. The treatment of melem with hydrazine hydrate transformed amino ($-NH_2$) functionalities into hydrazino ($-NH-NH_2$) functionalities which afforded melem hydrazine, MH (2,5,8-trihydrazino-*s*-heptazine).²³ The obtained white melem hydrazine was subjected to programmed heating at 450 °C for 2 h to obtain orange colored C_3N_5 polymer (Figure 2) (See supporting information for experimental details). Melem hydrazine has a highly hydrogen bonded structure which facilitates the formation of an azo-bridged heptazine framework by thermal condensation. Previously, Gillan also reported the formation of similar azo-bridged functionalities by heating nitrogen-rich 2,4,6- cyanuric triazide or triazido-1,3,5-triazine (C_3N_3)(N_3)₃ to form differential composition triazine-based carbon nitride.^{22, 24} In the same report Gillan suggested that transformation of cyanuric triazide into azo-bridged triazine carbon nitride framework proceeded through the nitrene intermediate ($C_3(N_3)_2N:$) and that the formation of C_3N_5 from melem hydrazine might proceed *via* a similar intermediate due to the thermolabile nature of hydrazine functionalities. The structures of melem, melem hydrazine and hydrogen bonded melem hydrazine are given in supporting information (Figure S1).

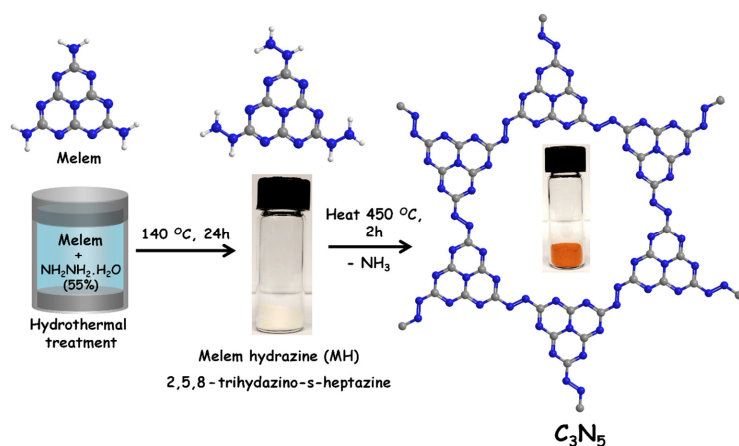


Figure 2. Synthesis schematic of C_3N_5 from melem *via* melem hydrazine (Atom color: N - blue, C - gray and H - white). The vials show the distinct color of the reaction product contrasted with that of the precursor.

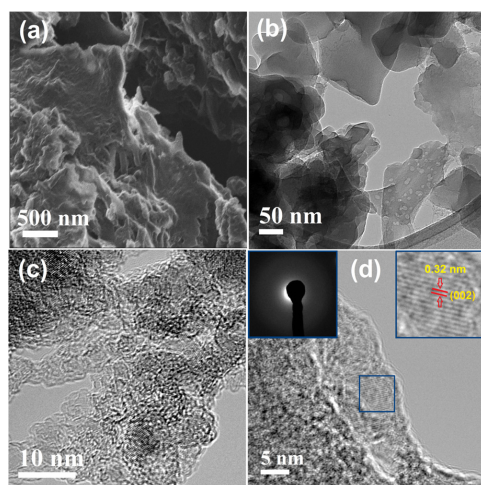


Figure 3. (a) He-ion image of C_3N_5 , and HR-TEM images of C_3N_5 (b) at 50 nm, (c) at 10 nm- and (d) at 5 nm scale bar; left and right insets showing SAED diffraction pattern and interplanar d spacing, respectively.

The surface morphology of the C_3N_5 polymer was investigated using a He-ion microscope equipped with an electron flood gun to facilitate positive charge neutralization accumulated from the He-ion beam (Figure 3a). The He-ion images of MHP show a rough, crumpled graphenic scaffold with some erupted morphologies which indicate that the high temperature treatment of MH monomeric unit facilitated polymerization into an irregular sheet-like structure. The fine structure of C_3N_5 material was determined using high resolution transmission electron microscopy (HR-TEM) (Figure 3b-d). The carbon nitride like layered sheet architecture is clearly evident in the TEM image of C_3N_5 at 50 nm scale bar (Figure 3b). Under long duration exposure of the electron beam, C_3N_5 starts to degrade and shrink which likely resulted due to high energy electrons breaking the $-N=N-$ linkage. HR-TEM images at 10 nm and 5 nm scale bar show crystallite fringes of nanoporous multilayered sheets with an interplanar d -spacing of 0.32 nm, corresponding to the 002 plane of the graphitic structure (Figure 3c, 3d, and inset). The observed d -spacing in C_3N_5 was identical to g- C_3N_4 from which we infer that during the thermal polymerization step, the stacking pattern of sheets in C_3N_5 remains similar to that in bulk g- C_3N_4 . The broad, less intense ring in the selected area electron diffraction (SAED) pattern was attributed due to diffraction of electrons by the 002 plane; however, the low intensity of the ring suggests amorphous nature of the material (inset of Figure 3d).

Formatted: Highlight

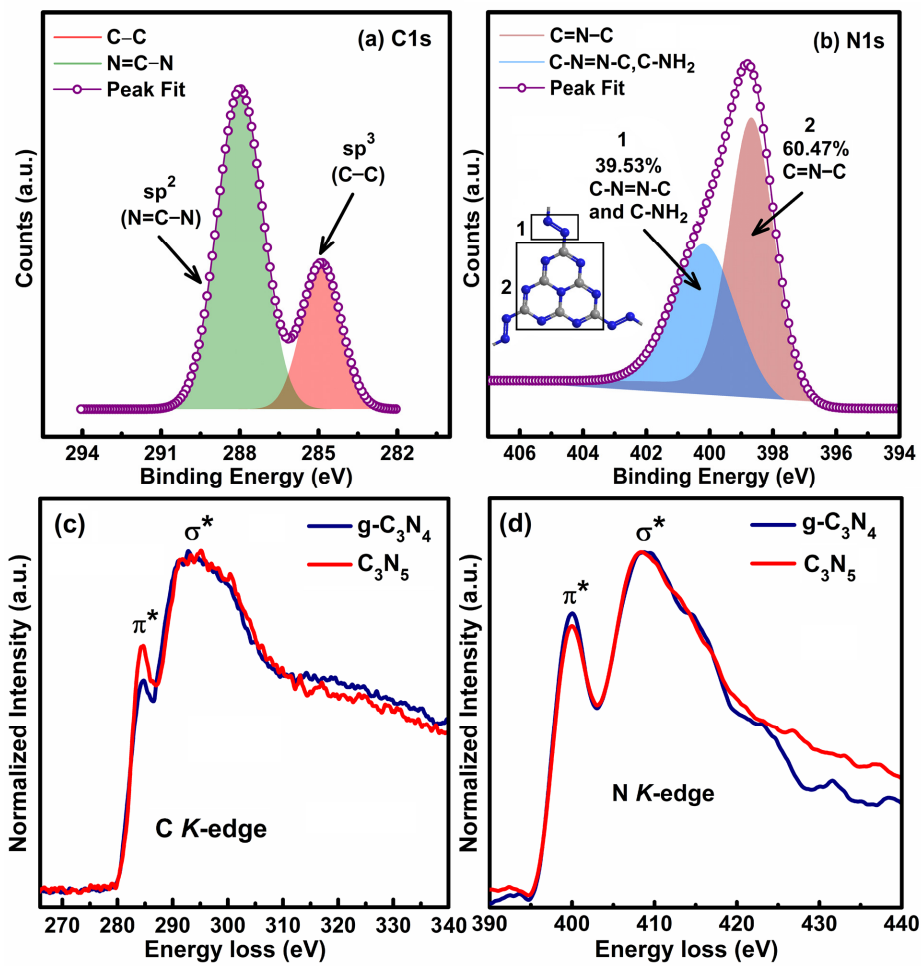
The surface chemical composition of the synthesized material was investigated using X-ray photoelectron spectroscopy, XPS (Figure 4). The XPS elemental survey scan of C_3N_5 shows peaks corresponding to C1s, N1s, Na1s, Cl2p, and O1s (Figure S2a). The presence of Na1s and Cl2p is due to intercalated Na^+ ions in the supramolecular cavity of the polymeric motif (Figure 1) and the residual NaCl formed during the purification step of MH. After excluding Na1s, Cl2p and O1s peaks, the at% of C and N in the C_3N_5 were found to be 36.76 63.24 % and 63.24 36.76 %

Formatted: Highlight

respectively, which represent an empirical formula of $C_3N_{5.16}$ for the C_3N_5 polymer (Table 1). The obtained composition matched well with theoretical C_3N_5 (N-62.50 at% and C-37.50 at%) stoichiometric carbon nitride materials. The high resolution XPS spectrum of C_3N_5 in C1s region was deconvoluted into two peak components at binding energies of 284.8 eV and 287.9 eV corresponding to the presence of sp^3 and sp^2 hybridized carbons, respectively (Figure 4a). The sp^3 carbon peak originated from adventitious carbons, edge group carbons and turbostratic carbons present in the scaffold of C_3N_5 polymer while the relatively stronger sp^2 peak appeared due to N=C–N type aromatic carbons which constitute the carbon nitride like framework of C_3N_5 .²⁵ The core level HR-XPS in N1s after deconvolution gave two peak components located at 398.7 eV and 400.2 eV. The peak at a binding energy of 398.7 eV was assigned to tertiary N–(C)₃ and secondary C=N–C nitrogens present in the aromatic ring structure while another peak at 400.2 eV was due to the presence of primary residual –NH₂ and bridging C–N=N–C type nitrogens (Figure 4b).²⁵⁻²⁶ From the N1s XPS spectrum, the at % of N present in aromatic ring (N_{ring}) and bridging (N_{bridging}) were found to 60.47 % and 39.53 % respectively and the at% ratio obtained was 3:2, which strongly supports the proposed structure in which two heptazine units are interconnected with the azo (–N=N–) motif and is also consistent with the theoretical C_3N_5 azo linked structure (Table 1). Furthermore, HR-XPS in Na1s region gave a peak at 1071.9 eV due to the presence of Na⁺ ions in the polymeric skeleton and residual NaCl (Figure S2b). The two peak components in Cl2p XPS, at binding energy values of 198.7 eV and 200.2 eV ascribed to Cl2p_{3/2} and Cl2p_{1/2} further validated the presence of Cl[–] in the form of NaCl (Figure S2c). Two XPS peaks in the O1s region located at 531.6 eV and 532.4 eV were associated with surface adsorbed adventitious oxygens and –OH groups (Figure S2d). The nature of C and N bonding in g- C_3N_4 and C_3N_5 was elucidated with electron energy loss spectroscopy (EELS) (Figure 4c,d and Figure S3+2). The normalized EELS

Formatted: Highlight

spectra of g-C₃N₄ and C₃N₅ exhibited two major symmetric peaks due to ~~the~~ contribution of C-K and N-K edge loss. The C K-edges signal of both g-C₃N₄ and C₃N₅ was composed of two peaks located at 284.6 and 293.2 eV corroborated to 1s- π^* and 1s- σ^* electronic transition of sp² hybridized carbons trigonally coordinated with nitrogens in s-heptazine nucleus (Figure 4c).^{14a, b, 27} The relative intensity of π^* C K-edge signal and π^*/σ^* peak area ratio of C₃N₅ was higher than g-C₃N₄ suggesting increased conjugation in C₃N₅ due to extended π orbitals overlap between bridging azo functionalities and heptazine motifs.²⁸ The formation of extended π conjugated network in C₃N₅ was also supported by increased UV-Vis absorption profile and shorter TRPL lifetime decay (Figure 7 and 8). The N K-edges energy loss peaks for g-C₃N₄ and C₃N₅ located at 399.8 and 408.5 eV, assigned to 1s- π^* and 1s- σ^* electronic transition of sp² hybridized nitrogens in heptazine ring and bridging N, further verify sp² hybridized nitrogen-rich carbon nitride framework (Figure 4d).¹³ Absence of any new peak in N K-edge loss of C₃N₅ demonstrate bridging nitrogens in C₃N₅ have almost identical electronic environment like N(C)₃ nitrogens in g-C₃N₄.²⁹ The relative peak intensity of N K-edge π^* signal of C₃N₅ was slightly lower than g-C₃N₄ demonstrating enhanced contribution of azo motifs in 1s- σ^* transition. The replacement of tertiary bridging nitrogens, N(C)₃ in g-C₃N₄ via azo nitrogens, C-N=N-C render lone pair on azo nitrogens which contribute to σ^* signal and relative intensity of π^* signal was suppressed. However, total peak area of N K-edge peak for C₃N₅ was increased which demonstrate addition of extra nitrogens in carbon nitride framework. The N:C atomic ratio of C₃N₅ was calculated to be 1.62 which was in close agreement with theoretical value (1.66) and C:N value obtained from CHNS analysis (1.65). Slightly lower N content might be due to cleavage of azo bond resulting in loss of some nitrogens under high energy electron beam.



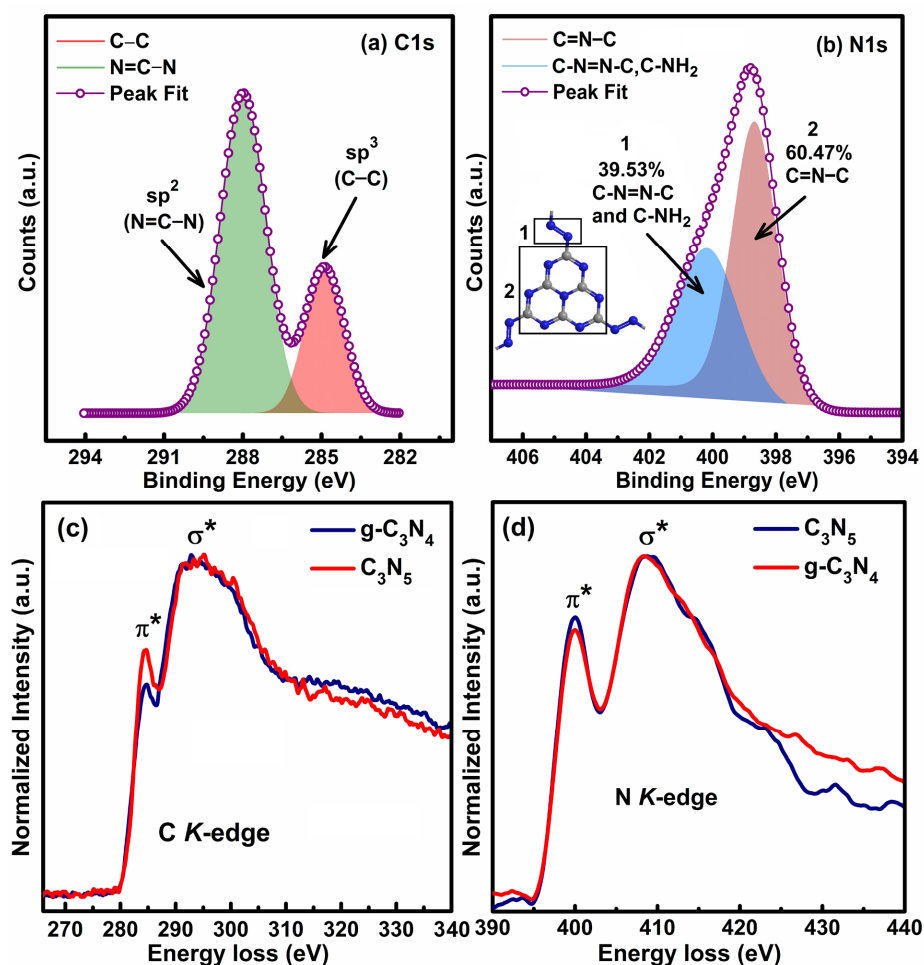


Figure 4. The core level HR-XPS spectra of C_3N_5 in (a) C1s region, (b) N1s region and normalized EELS spectra of $g-C_3N_4$ and C_3N_5 showing relative intensity of π^* and σ^* peaks for (c) C K-edge and (d) N K-edge loss.

Table 1. (a) Elemental analysis of C_3N_5 showing C, H, and N wt% and empirical formula and (b) XPS elemental analysis of C_3N_5 showing at% and empirical formula and their comparison with theoretical C_3N_5 composition.

(a) Elemental analysis						
Serial. No.		N (wt%)	C (wt%)	H (wt%)	Empirical formula	N _{ring} :N _{bridging} (at% ratio)
1.	CHN analysis	61.27	31.81	2.68	C ₃ N _{4.95} H _{1.01}	-
2	Theoretical wt% value	66.02	33.98	-	C ₃ N ₅	3:2 (60:40)
(b) XPS elemental analysis						
		N (at%)	C (at%)	H (at%)	Empirical formula	N _{ring} :N _{bridging} (at% ratio)
3.	XPS analysis	63.24	36.76	-	C ₃ N _{5.16}	~ 3:2 (60.47:39.53)
4.	Theoretical at% value	62.50	37.50	-	C ₃ N ₅	3:2 (60:40)

To probe the proposed composition and structure of the synthesized C₃N₅ material, CHNS elemental analysis was performed which gave 61.27 wt% N, 31.81 wt% C and 2.68 wt% H suggesting an empirical formula of C₃N_{4.95}H_{1.01} which was in close proximity with the theoretical wt% for C₃N₅ composition (Table 1). Slight difference between predicted and observed C:N ratio might be due to the presence of unbonded -NH₂ at the edge of sheets, formed by cleavage of hydrazino group (-NH-NH₂) at elevated temperature and loss of some azo nitrogens.^{9b, 10b} As expected, sulfur was not present at measurable levels. Notably, the observed hydrogen might arise from -NH₂ and -OH groups present at the edge of the polymeric framework.

To elucidate the chemical structure of MH and C₃N₅ materials, solid-state nuclear magnetic resonance (NMR) spectroscopy using the cross-polarization magic-angle spinning (CPMAS) technique was performed (Figure 5). CPMAS NMR enables the structural investigation of local- and medium-range structure in micro- and nano-crystalline compounds. The ¹³C CPMAS NMR spectra of melem hydrazine (MH) display three NMR signals at 164, 160 and 154 ppm (Figure 5a). The ¹³C NMR signals at 164 and 160 ppm originated from N₂C-NHNH₂ carbons while the

resonance at 154 ppm was observed from CN_3 carbons of the heptazine nucleus. The observed signals were in good agreement with the reported NMR spectra for MH and melem based structures.^{18a, 24, 30} The CPMAS NMR spectrum of C_3N_5 exhibits two ^{13}C NMR signals of approximately equal intensity at 164 and 156 ppm for $\text{N}_2\text{C}=\text{N}=\text{N}-$ and CN_3 carbons (Figure 5b).^{24, 30-31} The $\text{N}_2\text{C}-\text{NHNH}_2$ carbon signal of MH located at 160 ppm arising due to C-H functionalities disappeared in the ^{13}C NMR of C_3N_5 , which confirms removal of $-\text{NHNH}_2$ protons and formation of an azide linkage during polymerization step agreeing with ^{15}N CPMAS NMR, *vide infra*. Furthermore, the appearance of equally intense (Cc:Ce/1:1.07) ^{13}C peaks in the ^{13}C NMR spectrum of C_3N_5 suggests that heptazine units are in the presence of a symmetric azo bridging motif (where Cc corresponds to central carbons in ring and Ce to external carbons bonded to azo N). A slight shift to higher frequency in CN_3 carbon peaks from 154 ppm in MH to 156 ppm in C_3N_5 suggests shielding of carbons due to N2p overlap of azo and aromatic π system which extends the π conjugated network.³²

The ^{15}N CPMAS NMR spectrum of MH exhibits four signals, -207, -252, -273 and -317 ppm (Figure 5c).^{23a} The ^{15}N NMR signal at -207 ppm and another weak signal at -273 ppm were assigned to (NC_2) and (NC_3) nitrogens of the heptazine motif,^{23a, 31b, 32-33} while the peaks at -252 and -317 ppm assigned to NH_2 and NH terminal nitrogens of hydrazino moiety.³³⁻³⁴ The transformation of MH to C_3N_5 proceeds with removal of NH_3 and formation of azo linkage which was evident from the disappearance of NH_2 and NH peaks at -252 and -317 ppm in the ^{15}N NMR spectrum of C_3N_5 (Figure 5d). The two NMR peaks in the ^{15}N NMR spectra of C_3N_5 at -197 and -248 (weak) ppm were attributed to NC_2 and NC_3 nitrogens of heptazine skeleton while another peak at -271 ppm arose from $-\text{N}=\text{N}-$ (and residual NHs) type nitrogens. As the N atoms are in similar chemical environments, a semi-quantitative CPMAS NMR analysis of the ^{15}N peak areas

achieved by peak integration of NC_2 and NC_3 and $-\text{N}=\text{N}-$ resonances was found give a ratio of 1.00:0.18:0.54 which was in good agreement with the theoretical value (1.00:0.17:0.5) calculated for C_3N_5 polymeric structure containing heptazine units interconnected with azo linkage (Figure S1). Furthermore, ^1H NMR of MH gave an intense peak at 5.11 ppm due to NH and NH_2 hydrogens (Figure S4). This intense peak disappeared in the ^1H NMR spectra of C_3N_5 further confirming the removal of NH hydrogens and a very broad peak centered at 9.18 ppm appeared due to intercalated hydrogen, and residual carboxy and aldehyde hydrogens (essential for the CPMAS approach to function whereby ^1H magnetization is transferred to ^{13}C and ^{15}N). All these NMR results validate the successful synthesis of a modified carbon nitride framework.

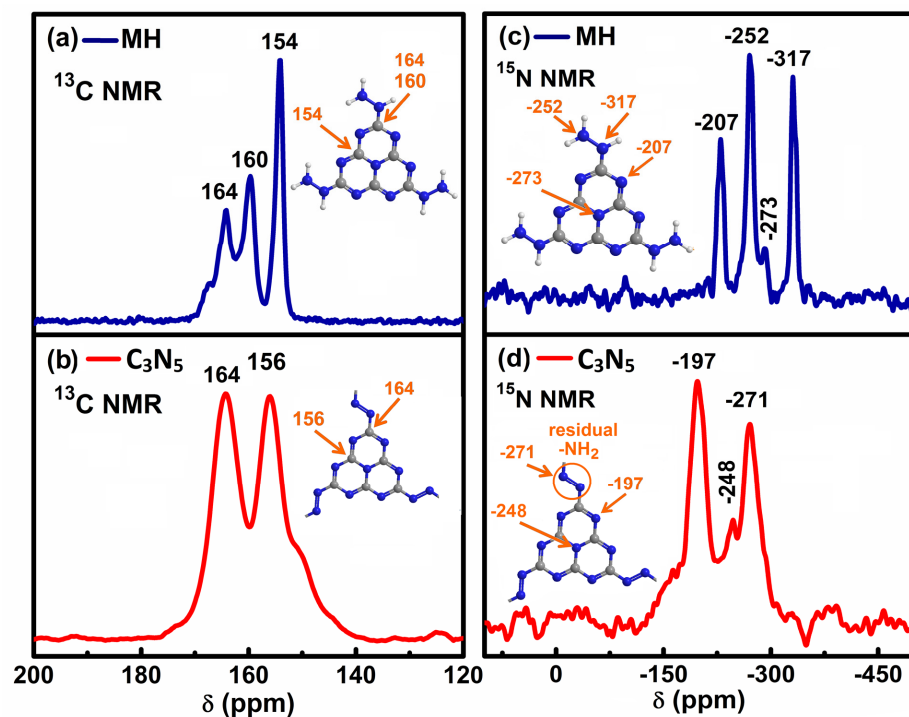


Figure 5. CPMAS NMR spectra (a) ^{13}C of MH, (b) ^{13}C of C_3N_5 , (c) ^{15}N of MH and (d) ^{15}N of C_3N_5 .

Fourier transform infrared (FTIR) spectroscopy was employed to determine the change in functional moiety in the material (Figure 6a-d). The FTIR spectrum of melem shows characteristic broad peaks at 3109 cm^{-1} due to the combined symmetric and antisymmetric stretch vibrations of $-\text{NH}_2$ and $-\text{OH}$ ($\nu_{\text{N-H}}$ and $\nu_{\text{O-H}}$) groups. The IR bands at 1595, 1411, 1230 and 1078 cm^{-1} are ascribed to the C–N stretch ($\nu_{\text{C-N}}$) of heptazine (C_6N_7) aromatic nucleus (Figure 6a).^{18a, 31b, 34a, 35} The N–H stretch band ranging from $3153\text{--}2895\text{ cm}^{-1}$ for MH was found to become broader due to combinational symmetric and asymmetric N–H stretches of $-\text{NH-NH}_2$ group in MH which confirms the successful transformation of $-\text{NH}_2$ moiety in melem to $-\text{NH-NH}_2$ in melem hydrazine (Figure 6b). The broadening of NH peak was attributed to strong intermolecular hydrogen bonding in MH molecules.³⁵⁻³⁶ However, all stretching and bending peaks due to heptazine aromatic ring skeleton remain preserved which indicates that the heptazine motif remains unchanged during the hydrazine treatment. Additionally, some new peaks emerged at 1095 and 965 cm^{-1} implicating the N–N stretch and $-\text{NH}_2$ rocking vibration respectively.^{18a, 36-37} Graphitic carbon nitride shows characteristic peaks at 3145 cm^{-1} due to residual $-\text{NH}_2$ and $-\text{OH}$ stretch and $1639\text{--}1145\text{ cm}^{-1}$ due to triazine ring stretch and 798 cm^{-1} for triazine ring bending vibration was in good agreement with the reported literature (Figure 6c).³⁷⁻³⁸ After conversion of MH to C_3N_5 by thermal annealing, the intensity of $-\text{NH-NH}_2$ peak of MH was diminished which implicated the transformation of $-\text{NH-NH}_2$ group into azo ($-\text{N=N-}$) linkage through the removal of NH_3 (Figure 6d). It is important to note that vibration of symmetrical $-\text{N=N-}$ azo linkage is forbidden due to which no new sharp peak due to azo functionalities was observed. The possibility of $-\text{NH-NH-}$ bond can be neglected due to the absence of any strong N–H band; however very

weak broad peaks arise due to some residual -NH_2 present at the edge of the polymeric framework. This fact was well supported by CHNS analysis which showed the presence of only one H for each stoichiometric C_3N_5 unit (Table 1). Further, other peaks of MH at 1095 and 965 cm^{-1} due to N–N stretch and -NH_2 rocking vibration disappear in C_3N_5 , which confirmed the transformation of hydrazine group into azo moiety. Peaks corresponding to the C_3N_4 framework at 1542 , 1315 and 887 cm^{-1} were absent in C_3N_5 which suggests an entirely different network of C_3N_5 in comparison to g- C_3N_4 .

The changes in phase structure and crystalline nature of melem, MH, g- C_3N_4 , and C_3N_5 were investigated through the measurement of X-ray diffraction (XRD) (Figure 6). The XRD pattern of melem demonstrated a series of peaks located at 12.5° , 13.6° , 16.7° , 18.4° , 19.7° , 22.0° , 25.2° , 27.2° and 30.4° , in close agreement with previous reports (Figure 6e).³⁸⁻³⁹ The XRD results indicate the absence of any melamine impurity in the melem sample.^{18b, 39a} Due to the transformation of melem into melem hydrazine, the XRD pattern of MH changed, with new peaks being observed at 2θ values of 7.3° , 7.9° , 8.4° , 12.9° , 13.7° , 14.8° , 25.1° and 28.0° (Figure 6f). Bulk g- C_3N_4 shows two distinct XRD peaks at 2θ values of 27.1° and 13.0° indexed to the 002 and 100 planes of carbon nitride materials (Figure 6g). The 002 peak with a 0.32 nm interplanar d spacing was correlated to interplanar stacking of sheets while 100 peaks with a 0.68 nm spacing was specific to in-plane structural packing of heptazine units (Figure 6g).^{18b, 39b, 40} The XRD pattern of C_3N_5 exhibits one broad 002 peak at 27.6° corresponded to 0.33 nm interplanar sheet distance. The slight increase in 2θ value and d spacing can be explained due to repulsion between electron rich π conjugated C_3N_5 sheets as in graphite (0.34 nm) (Figure 6h). Further, the absence of 100 peak – a specific feature of in-plane packing, suggests distortion in the carbon nitride framework and broadening of the nanochannel distance between heptazine units due to azo (-N=N-) bridging

linkage, further consistent with ^{13}C and ^{15}N NMR resonance broadening above, suggesting local/medium-range disorder. Also, bridging of two heptazine units with two nitrogens through in-plane lattice packing is less efficient in C_3N_5 which was responsible for the absence of any expected peak at lower 2θ values. These XRD results clearly support the distinct structure of C_3N_5 possessing azo linkage.

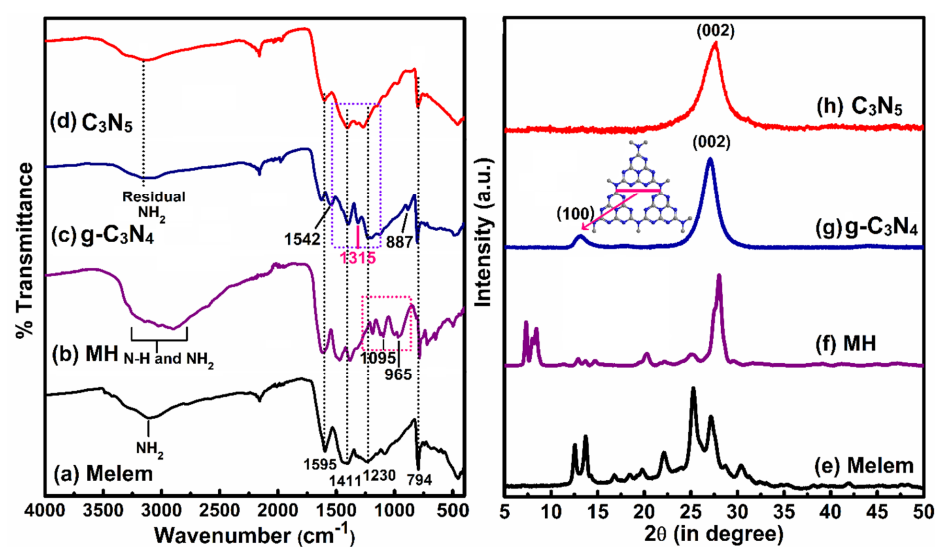


Figure 6. FTIR spectra of (a) Melem, (b) Melem hydrazine, (c) $\text{g-C}_3\text{N}_4$, (d) C_3N_5 , and XRD diffraction pattern of (e) Melem, (f) Melem hydrazine, (g) $\text{g-C}_3\text{N}_4$, (h) C_3N_5 .

Raman spectra of melem acquired using 632 nm laser excitation show characteristic fingerprint peaks of melem at 435 and 697 cm^{-1} due to heptazine ring (C_6N_7) breathing modes and a broad hump at 1452 cm^{-1} due to $-\text{NH}_2$ bending mode (Figure S5a).^{18a, 40a} Raman spectra of MH demonstrate many signature peaks correlated to the core at 472, 744 and 1529 cm^{-1} which were shifted in comparison to melem due to functionalization while other peaks due to various

vibrations of the heptazine nucleus and hydrazine group were observed at 127, 342, 537, 985, 1159, 1314 and 3071 cm^{-1} , in good agreement with the reported literature (Figure S5b).^{18a, 23a, 40b}

⁴¹ The Raman spectra of g- C_3N_4 display many prominent peaks due to the heptazine framework at 471, 697, 706 cm^{-1} (heptazine ring breathing modes) and two additional peaks at 1233 and 1567 cm^{-1} corresponding to the $-\text{NH}_2$ bending mode and graphitic G band (Figure S5c).^{23a, 42} Further, the presence of a broad hump extended from 1100-1600 cm^{-1} suggests multilayer stacking of g- C_3N_4 sheets.^{41, 43} In the Raman spectra of C_3N_5 , only trace peaks of melem hydrazine motif are observed which indicates the complete transformation of MH to C_3N_5 . Two small peaks were observed at 1085 and 1161 cm^{-1} due to the mixed vibration of heptazine motif and azo stretch (Figure S5d). A sharp peak at 1609 cm^{-1} originated due to the C=N stretching mode.

Figure 7a displays the diffuse reflectance UV-Vis (DR-UV-Vis) spectra of g- C_3N_4 and C_3N_5 . The DR-UV-Vis spectra of g- C_3N_4 shows a characteristic absorption peak between 200–400 nm with a band tail extended up to 450 nm due to charge transfer from the populated valence band of the nitrogen atom (2p orbitals) to the conduction band of the carbon atom (2p orbitals) of carbon nitride. The less intense absorption band at 330 nm is due to $\pi \rightarrow \pi^*$ transition in the conjugated network while another intense peak at *ca.* 387 nm appeared due to $n \rightarrow \pi^*$ transition from nitrogen nonbonding orbital to the aromatic nonbonding orbital.^{12b, 42-44} The DR-UV-Vis spectrum of C_3N_5 demonstrates a drastic change in the UV-Vis absorption profile in comparison to g- C_3N_4 due to a more extended π conjugated network (Figure 7a).^{12b, 45} A broad absorption peak around 393 nm in UV-Vis spectrum of C_3N_5 was attributed to $n \rightarrow \pi^*$ transition from nitrogen nonbonding orbital to the π conjugated nonbonding orbital. The absorption spectrum of C_3N_5 was red shifted showing band tailing up to 670 nm, due to an extended π conjugated network arising from the overlap between N2p orbitals of bridging azo moieties and N2p in heptazine π conjugated

system. Further residual -NH_2 also contributes to the delocalized aromatic π conjugated system. Due to this, the position of the valence band gets upshifted and $\pi \rightarrow \pi^*$ transition occurs at ~~a~~ relatively low energy which facilitates the absorption of a large fraction of the visible spectrum and results in the sample displaying an orange color. Further, the optical bandgaps of g- C_3N_4 and C_3N_5 were determined using a Tauc plot by plotting a graph between $(\alpha h\nu)^{1/2}$ vs $h\nu$ and extrapolation of the linear tangent to abscissa; where α is absorption coefficient, h is plank constant and ν is light frequency (Figure S6a). From the Tauc plot, the value of bandgap for g- C_3N_4 was estimated to be 2.65 eV corresponding to a band-edge at a wavelength of 467 nm, in good agreement with the bandgap values reported in the literature.⁴⁶ The bandgap value of C_3N_5 was calculated to be 1.76 eV corresponding to a band-edge at a wavelength of 707 nm.

Photoluminescence (PL) spectra were collected by exciting samples using 360 nm photons to probe radiative recombination (Figure 7b). The PL spectrum of melem consists of an intense emission peak centered at 441 nm which is indicative of radiative recombination of carriers within melem unit.^{39a, 44} It is important to note here that melem exhibits excitation wavelength-dependent PL emission. On the other hand, g- C_3N_4 showed a sharp emission peak at 468 nm which did not shift upon changing the excitation wavelength. This peak is attributed to fast interlayer carrier recombination in multilayered sheets of bulk g- C_3N_4 .^{45, 47} Surprisingly, C_3N_5 does not exhibit any distinguishing PL peak which might be indicative of efficient charge separation between the bulk and the surface. Such charge transfer excitonic states involving the bulk and the surface, have also been observed in other conjugated organic semiconductors that possess an extended π -conjugated network that prevents radiative recombination by delocalizing the Frenkel exciton. However, due to conductive conjugated surface non-radiative charge recombination can take place over new localized states in the sheets scaffold.⁴⁸

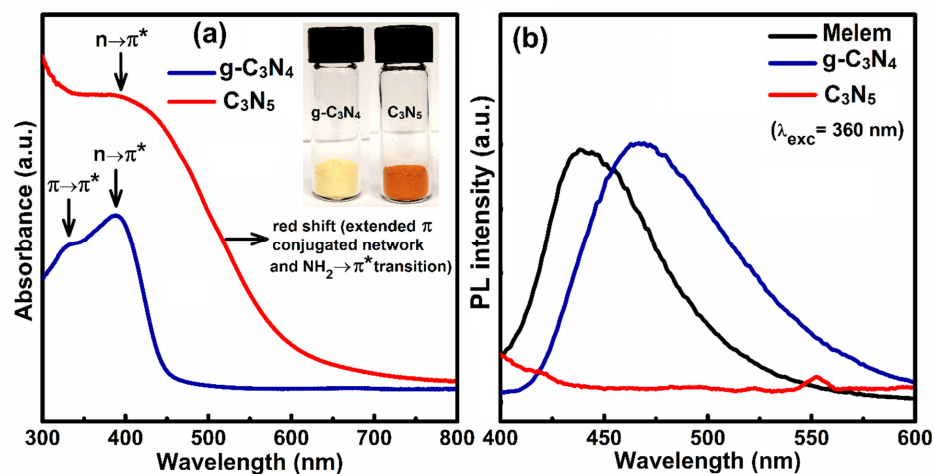


Figure 7. (a) DR-UV-Vis spectra of g-C₃N₄ (blue) and C₃N₅ (red), with inset showing photographs of g-C₃N₄ and C₃N₅ samples and (b) Steady-state PL spectra of melem (black), g-C₃N₄ (blue) and C₃N₅ (red) obtained using an excitation wavelength of 360 nm.

In order to investigate the lifetime of excited charged species, and charge separation processes, we collected time resolved photoluminescence (TRPL) spectra of g-C₃N₄ and C₃N₅ using a single photon picosecond pulsed laser at a wavelength of 405 nm. Figure 8 displays the PL lifetime decay curves of g-C₃N₄ and C₃N₅. The PL decay curve was fitted tri-exponentially using the following equation:

$$I(t) = A_1 e^{-t/\tau_1} + A_2 e^{-t/\tau_2} + A_3 e^{-t/\tau_3} \quad (1)$$

where, A_1 , A_2 , and A_3 represent the normalized amplitudes of each decay component and τ_1 , τ_2 and τ_3 are values of the lifetime components respectively. The existence of three radiative lifetimes in the fitted PL lifetime spectra of g-C₃N₄ and C₃N₅ was in good agreement with previously

reported carbon nitride-based materials.⁴⁹ The obtained values of lifetimes and their fractional components are given in Table 2.

Table 2. The PL lifetime of photogenerated charge carrier and their relative contribution in g-C₃N₄ and C₃N₅.

Sample	τ_1 (ns) [A ₁]	τ_2 (ns) [A ₂]	τ_3 (ns) [A ₃]	Average lifetime (τ_{avg}) ns
g-C ₃ N ₄	3.31 [0.34]	0.75 [0.63]	25.02 [0.05]	12.43
C ₃ N ₅	8.10 [0.07]	2.11 [0.26]	0.28 [0.73]	4.40

The three components in the PL lifetime decay curve of g-C₃N₄ can be assigned to various energy states in g-C₃N₄ formed by the overlap of C and N sp² and sp³ hybridized orbitals and the presence of lone pairs of electrons which allow for various radiative transitions. g-C₃N₄ is composed of tri-s-triazine (C₆N₇) units inter-connected with tertiary nitrogen atoms where C-N sp³ hybridized state constitute high energy σ and σ^* molecular orbitals while C-N sp² hybridization gives rise to a conjugated network resulting in low energy π bonding and π^* antibonding orbital which constitutes the valence and conduction bands respectively.⁵⁰ The presence of unbonded lone pairs of electrons on pyridinic N atoms creates energy levels just below the π bonding orbital and their overlap with the π conjugated system can further decrease the energy of the π molecular orbital resulting in the reduction of the bandgap.⁵¹ The first two shorter lifetime components of 3.31 and 0.75 ns with 34 % and 63 % contribution in g-C₃N₄ correspond to charge carrier recombination from σ^* and π^* antibonding to π MO.⁵² The third longer lifetime component of 25.02 ns with a relative low contribution originated due to intersystem crossing (ISC) of electron from σ^* and π^* orbital followed by radiative relaxation to conjugated π orbital and trap-assisted radiative

recombination.⁵³ The first two lifetimes of C₃N₅ at 8.10 and 2.11 ns with 7 % and 26 % contributions in the PL decay curve were significantly longer lived in comparison to g-C₃N₄, strongly suggesting that the introduction of azo moiety extends π conjugated network which facilitates better charge carrier mobility on C₃N₅ sheets (delocalized the exciton, as mentioned previously) and prevents faster charge carrier recombination.⁵⁴ Further, due to extended conjugation, the difference between σ^* and π^* band get decreased which is also evident in Mott-Schottky measurement (Figure S6b).^{51a} The low energy difference between σ^* and π^* accelerates the transfer of electrons from σ^* and π^* orbital via intersystem crossing followed by radiative relaxation which was evident from higher percentage contribution of the third lifetime component (73 %).

The average lifetime (τ_{avg}) which is regarded as coherent measure to evaluate the rate of spontaneous emission was calculated from the three lifetime components using the following expression.

$$\tau_{\text{avg}} = (A_1\tau_1^2 + A_2\tau_2^2 + A_3\tau_3^2) / (A_1\tau_1 + A_2\tau_2 + A_3\tau_3) \quad (2)$$

From Eq (2), the average lifetimes of g-C₃N₄ and C₃N₅ were calculated to be 12.43 and 4.40 ns respectively. The decreased lifetime of the C₃N₅ in comparison to g-C₃N₄ coupled with the very weak photoluminescence of C₃N₅ (as seen in Figure 7b) is indicative of fast quenching of the C₃N₅ luminescence. The fast quenching might originate from improved charge separation in C₃N₅ due to a larger conjugated π network but might also be due to stronger non-radiative transitions. Fast exciton dissociation with concomitant high carrier mobility can result in photogenerated electrons finding trap sites (and moving to them) and recombining by non-radiative processes.^{48a} The aforementioned processes are highly likely in C₃N₅ since the presence of azo bonds extends the π

network because of overlap of N2p orbital on azo nitrogens with the π network of heptazine motif due to which electrons can move within C_3N_5 scaffold freely. The lower PL lifetime of C_3N_5 in comparison to g- C_3N_4 was consistent with steady-state PL where C_3N_5 shows prodigious quenching in its PL spectrum.

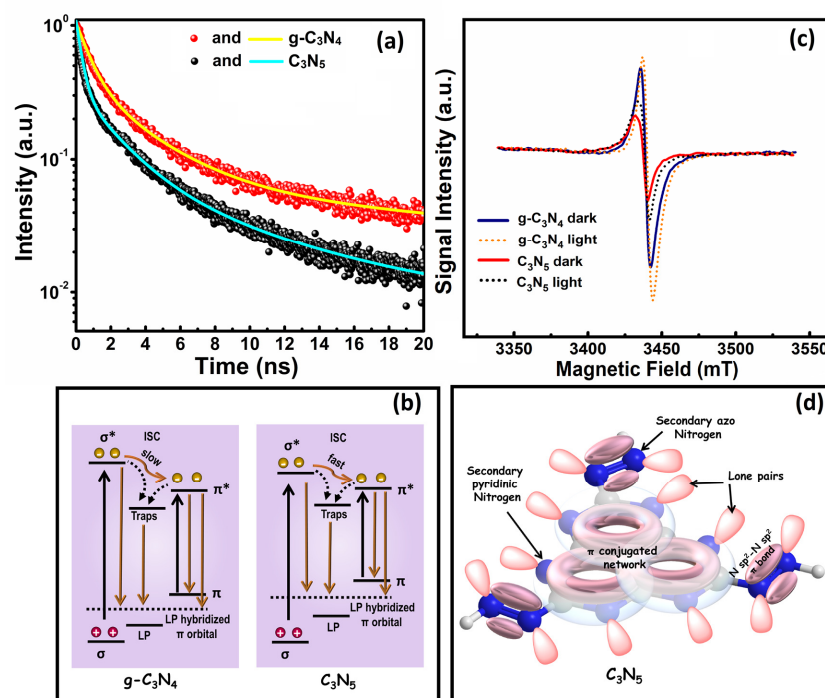


Figure 8. (a) PL lifetime decay curves of g- C_3N_4 (red; tri-exponential fit, yellow line) and C_3N_5 (black, tri-exponential fit, cyan), (b) Schematics of various energy levels bands and possible route of charge carriers recombination (c) X-band EPR spectra of g- C_3N_4 in the dark (blue), after light irradiation (orange dots) and C_3N_5 in the dark (red) and after light irradiation (black dots) at room temperature, (d) Plausible molecular orbital overlap representation of C_3N_5 .

Electron paramagnetic resonance (EPR) spectra of g-C₃N₄ and C₃N₅ to elucidate electronic nature and band excited paramagnetic species were collected under dark and UV irradiation at room temperature (Figure 8b). The EPR spectra of g-C₃N₄ under dark conditions exhibits an intense Lorentzian EPR resonance signal located at a g-factor of 2.003. The observed EPR signal originated due to the presence of unpaired electrons in the sp² hybridized aromatic π -system which was in good agreement with previous reports.^{36, 55} The EPR signal intensity of g-C₃N₄ increased after UV irradiation, attributed to populated unpaired electrons in the conduction band due to π - π^* and N non-bonding to π^* (n- π^*) transition followed by slow relaxation *via* ISC. The observed EPR signal of C₃N₅ was also observed at 2.003 g-value which implies basic graphitic heptazine skeleton remains intact in C₃N₅ framework.⁵⁶ Further, after irradiation with UV light, the EPR signal intensity of C₃N₅ was also enhanced due to increased numbers of unpaired electrons in the conduction band. However, the overall EPR signal intensity of C₃N₅ in both the dark and under UV illumination was significantly weaker in comparison to g-C₃N₄ which was attributed to a lesser number of unpaired electrons in C₃N₅, which in turn can be taken as evidence of the presence of extra N atoms outside the heptazine nucleus in comparison to conventional N-rich carbon nitride materials where N atoms substitute C atoms in the heptazine motif. It is well documented in the literature that substitution of sp² hybridized +4 state C atom in heptazine motif with sp² hybridized +3 state N atom will liberate extra electrons in the aromatic system which will distort electronic symmetry^{16, 47, 57} and also increase EPR signal intensity. However, in the case of C₃N₅, the additional N atom makes an azo bond with an N atom outside the ring via π overlap and the extra electrons remain in the form of lone pairs (Figure 8d).

Fluorescence lifetime imaging microscopy (FLIM) of samples at different spots was used to probe the homogeneity of samples and to determine the nature of the fluorescence (Figure S79).

Formatted: Highlight

The PL spectra of g-C₃N₄ samples obtained from different spots exhibited identical emission profiles with a sharp intense peak at 480 nm which was in good agreement with the steady-state PL spectrum (Figure 7b). The slight red shift in the emission peak (Figure S79a) is attributed to the difference in the mechanism of excitation (750 nm two-photon excitation source for FLIM, 360 nm single photon excitation in Figure 7b). Furthermore, the emission spectrum of C₃N₅ displays two relatively weak peaks centered around 410 and 490 nm which likely originated from some relatively smaller C₃N₅ polymeric fragments and heptazine networks (Figure S79cb). The smaller fragments are consistent with a lesser number of MH units and therefore exhibit PL properties closer to melem. FLIM images of g-C₃N₄ were brighter than C₃N₅ which further supports our inference that the charge separation process was dominant in C₃N₅ samples (Figure S79be and Fig. S79d). The C₃N₅/MB samples obtained after methylene blue (MB) dye adsorption displayed relatively strong PL and brighter FLIM images due to the presence of MB in the composite (Figure S79e and Figure S79f). The absence of PL quenching in the C₃N₅/MB composite further suggests the absence of photo-induced charge transfer between the methylene blue and C₃N₅.

The synthesized C₃N₅ material was explored for dye adsorption studies using methylene blue (MB) as a model dye. Methylene blue is a staining dye widely used in the paper, textile and leather industries which also constitutes a good example of a colored water contaminant which due to its excellent visible light absorption, reduces light penetration in aqueous ambients and adversely affects aquatic flora and fauna. All dye adsorption studies were carried out at room temperature and under dark conditions. UV-Vis spectra of samples were collected for determining the concentration of MB solutions during dye adsorption experiments (For experimental details, see supporting information). MB has a sharp peak at 664 nm due to π - π^*

Formatted: Highlight

Formatted: Highlight

Formatted: Highlight

Formatted: Highlight

Formatted: Highlight

Formatted: Highlight

Formatted: Highlight

Formatted: Highlight

Formatted: Normal (Web), Font Alignment: Baseline

Formatted: Highlight

transition and a shoulder around 614 nm which represents MB present in dimeric and polymeric π stacked forms in water (Figure 9a). After the addition of C_3N_5 sample into methylene blue solution, the color of the solution instantaneously turned green. The green solution after centrifugation turned completely colorless which demonstrated the prompt adsorption of MB dye over the surface of C_3N_5 and subsequent settling of the MB adsorbed C_3N_5 during centrifugation. The obtained solid after centrifugation (denoted as C_3N_5/MB) exhibits a sharp absorption peak intermediate between C_3N_5 and MB with a broad peak centered at 680 nm. The red-shifting in the peak of C_3N_5 from 664 to 680 nm is attributed to the transformation of MB into monomeric form and some degree of ground state charge transfer from C_3N_5 to MB during adsorption on the surface of C_3N_5 . The dye adsorption performance of C_3N_5 was much higher than g- C_3N_4 . MB is a well known cationic dye possessing positive charge centered on the S atom in aqueous solutions.⁵⁸ On the other hand, the surface of C_3N_5 material has electron rich character due to the presence of secondary N (NC_2) in heptazine moieties, terminal $-NH_2$ and π extended network. Therefore, electrostatic interactions between the positively charged MB molecule and negatively charged C_3N_5 are likely responsible for the instantaneous adsorption.^{54, 59} To confirm negative charge on the surface of C_3N_5 , zeta potential measurement was performed which depicts average surface charge -36.2 mV prove the electron-rich surface of C_3N_5 (Figure S840). Further MB can also adsorb on the surface of C_3N_5 via π - π stacking between aromatic conjugated network of MB and π framework of C_3N_5 (Figure 9b).⁶⁰ To investigate the role of surface specific properties in the enhanced adsorption profile, Brunauer-Emmett-Teller (BET) surface area (S_{BET}), pore volume (V_p) and pore diameter (r_p) of g- C_3N_4 and C_3N_5 were measured by N_2 adsorption and desorption. The obtained BET surface area, pore volume and pore diameter for g- C_3N_4 were found to be 11.47 m² g⁻¹, 0.095 cm³ g⁻¹ and 19.13 nm while these values for C_3N_5 were found to be 1.78 m² g⁻¹, 0.002 cm³ g⁻¹ and 16.98

Formatted: Highlight

nm, respectively. The obtained surface values indicate a decrement in the surface area of C_3N_5 in comparison to g- C_3N_4 . The relatively low surface area of C_3N_5 might be due to the less gas evolution (three NH_3 per heptazine unit) from melem hydrazine precursor during thermal annealing step while the formation of g- C_3N_4 from melamine precursor releases six NH_3 molecule per heptazine unit. Further, hydrogen bonded melem hydrazine precursor might promote in-plane cross-linking of heptazine units leading to a stacked sheets type structure which reduces the effective accessible surface area. Contrarily, in g- C_3N_4 ring formation and polymerization step can produce cross-linking between sheets giving a porous structure with high surface area. The obtained results suggests that an electronic interaction between C_3N_5 and MB is responsible for the superior adsorption performance of C_3N_5 rather than an increased surface area.

Formatted: Font: (Default) Arial, Bold, Font color: Blue

To investigate whether the nature of adsorption was chemisorption or physisorption, and to explore the possibility of any chemical bonding, the C_3N_5 /MB composite was analyzed using NMR spectroscopy. The ^{13}C NMR spectrum of C_3N_5 /MB composite did not show any change in peak position and intensity of C_3N_5 which demonstrated the adsorption of MB on C_3N_5 to be purely physisorptive in nature (Figure S944d). FTIR, Raman and PL spectra of C_3N_5 /MB composite displayed various cumulative peaks and signals due to the presence of MB in the C_3N_5 /MB composite. However, no evident signals for any chemical interaction can be identified which further supports a purely physical interaction (physisorption) between C_3N_5 and MB (Figure S944a-c). Additionally, XPS spectra of C_3N_5 /MB composite were identical to pristine C_3N_5 samples which revealed that C_3N_5 signals dominated over MB, and no change in BE value was observed which ruled out the possibility of any chemical bond formation between C_3N_5 and MB (Figure S103).

Formatted: Highlight

Formatted: Highlight

Formatted: Highlight

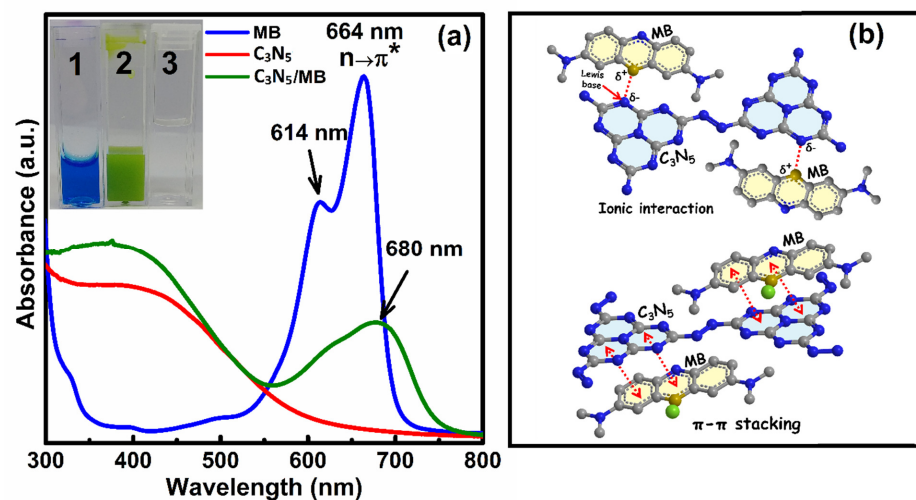


Figure 9. (a) UV-Vis absorption spectra of MB (blue), C₃N₅ (red) and C₃N₅/MB solution just after 1 min of absorption (green). Inset showing photographs of (1) MB before absorption, (2) after absorption and (3) solution after centrifugation, (b) Possible ionic and π - π stacking interaction between methylene blue and C₃N₅.

To quantify the excellent dye adsorption capacity of C₃N₅, various parameters such as the adsorption capacity, adsorption constants, linear regression correlation coefficient, and adsorption isotherm were measured and compared with pristine g-C₃N₄ (Figure 10 and Table 32). The adsorption capacity (amount of dye adsorbed) of g-C₃N₄ and MHP materials was calculated using equation 3

$$q = \frac{(C - C_e)V}{m} \quad (3)$$

Where q is the adsorption capacity, V is the volume of MB solution, m is the mass of the added adsorbent, and C and C_e are the initial and equilibrium concentrations of MB, respectively. The

Formatted: Highlight

kinetics of methylene blue adsorption on the surface of g-C₃N₄ and C₃N₅ were investigated using first and second order adsorption kinetics using following equations 4 and 5.

$$q_t = q_e(1 - e^{-kt}) \quad (4)$$

$$q_t = \frac{kq_e^2 t}{1 + kq_e t} \quad (5)$$

Where q_e is adsorbed amount of dye after reaching equilibrium and q_t is the adsorbed amount at time t , and k is the pseudo-first order or pseudo-second order adsorption rate constant.

The results obtained using pseudo-first order and pseudo-second order kinetics are displayed in Table 3 and Figures 10a and 10b. The kinetic studies clearly demonstrate that the prepared C₃N₅ samples can reach approx. 95% adsorption-desorption equilibrium instantaneously (1 min), and complete adsorption-desorption equilibrium condition within 10 min, which is an extraordinary performance compared to previously reported carbon nitride and carbon-based materials which usually take 45 min to achieve equilibrium.⁶¹ In addition, the kinetics study indicated that the adsorption of methylene blue on the C₃N₅ and g-C₃N₄ materials follows pseudo-second order adsorption kinetics, which agreed well with previous reports.^{61a} For isotherm studies, standard solutions of 5, 10, 15, 20, 25 and 30 ppm MB in water were prepared, 50 mL of these standard solutions were placed in a beaker and 50 mg of the adsorbents were added to them. The solutions were kept under strong stirring for 30 minutes under dark condition to reach equilibrium and then the concentration of methylene blue was calculated using UV-Vis spectroscopy (See Supporting Information for detail). The adsorption isotherms of methylene blue were investigated in terms of the Langmuir^{61b, 62} and Freundlich models^{61b, 63} (equations 6 and 7 respectively) and the results for g-C₃N₄ and C₃N₅ are displayed in Figures 10c and 10d respectively; the relevant

1
2
3
4
5
6
7
8
9
10
11
12
13
14
15
16
17
18
19
20
21
22
23
24
25
26
27
28
29
30
31
32
33
34
35
36
37
38
39
40
41
42
43
44
45
46
47
48
49
50
51
52
53
54
55
56
57
58
59
60

constants are reported in Table 3. It can be seen from Figure 10 and Table 3 that the value of R^2 extracted by employing the Langmuir isotherm model was higher than R^2 value obtained from the Freundlich isotherm model, indicating that the Langmuir model representing complete monolayer coverage on homogeneous sites was successful in predicting the adsorption of methylene blue on both g-C₃N₄ and C₃N₅.⁶⁴

$$q_e = \frac{QbC_e}{(1+bC_e)} \tag{6}$$

$$q_e = KC_e^n \tag{7}$$

Where q_e is adsorbed amount of dye after reaching equilibrium (mg g⁻¹), R is correlation coefficient, Q is the monolayer adsorption capacity (mg g⁻¹), b is the adsorption coefficient (L mg⁻¹), C_e is the equilibrium concentration and K is the Freundlich constant.

Table 3. The pseudo-first and -second order kinetic models of MB adsorption on g-C₃N₄ and C₃N₅ and Langmuir and Freundlich adsorption models showing isotherm constants.

Serial No.	Sample name	Pseudo-first-order			Pseudo-second-order		
		k (s ⁻¹)	q_e (mg g ⁻¹)	R^2	k (s ⁻¹ mg ⁻¹ L)	q_e (mg g ⁻¹)	R^2
1.	g-C ₃ N ₄	0.16	2.35	0.96	0.08	2.6	0.99
2.	C ₃ N ₅	6.35	6.83	0.98	2.24	6.95	0.99
S.No.	Sample name	Langmuir			Freundlich		
		Q (mg g ⁻¹)	b (L mg ⁻¹)	R^2	K (mg ¹⁻ⁿ L ⁿ g ⁻¹)	n	R^2
1.	g-C ₃ N ₄	6.03	0.13	0.97	1.21	0.43	0.96
2.	C ₃ N ₅	42.32	0.05	0.98	2.40	0.78	0.97

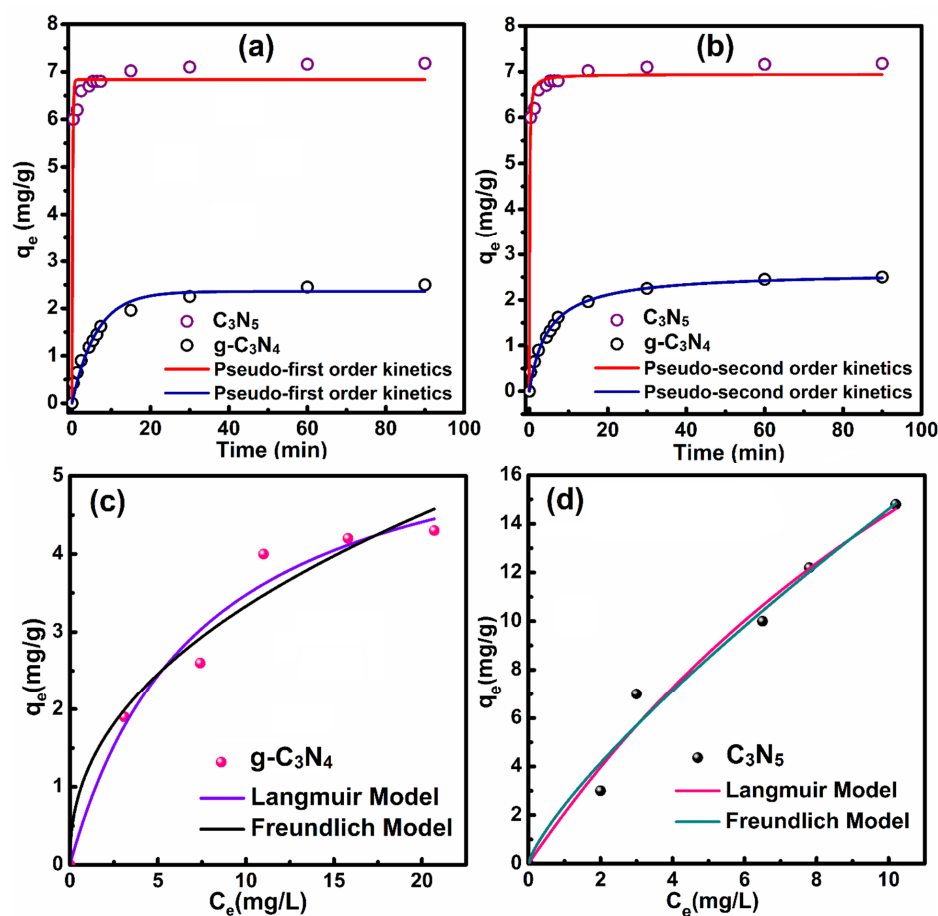


Figure 10. Kinetics of MB dye adsorption on g-C₃N₄ and MB displaying (a) Pseudo-first order fitted curve (b) Pseudo-second order fitted curve and MB adsorption isotherms fitted by Langmuir and Freundlich model of (c) g-C₃N₄ and (d) C₃N₅ respectively. q_e is the amount of dyes adsorbed at equilibrium while C_e is the equilibrium concentration of MB.

To check whether C_3N_5 material displays any visible light induced dye degradation activity, 50 mL of 50 ppm MB containing solution was charged with 50 mg C_3N_5 catalyst and stirred in the dark for 30 min to reach adsorption-desorption equilibrium. Subsequently, the obtained suspension was irradiated under simulated sunlight (AM1.5G, 100 mW cm⁻²). After every 10 min, 1 mL of sample was withdrawn and centrifuged to remove solid C_3N_5 and the supernatant liquid was analyzed with UV-Vis spectroscopy. The UV-Vis analysis indicated that the concentration of MB solution does not change even after 8 h of irradiation. These results suggest that C_3N_5 is not active for dye degradation which might be because of unfavorable band alignment. To understand the band structure of C_3N_5 , Mott Schottky plots were obtained in 0.5 M Na_2SO_4 solution (Figure S6b). From the Mott-Schottky plot, the flat band positions of g- C_3N_4 and C_3N_5 were found to be -1.05 and -0.91 V vs Ag/AgCl, respectively, which can be considered the conduction band position if the Fermi level lies just below conduction band (strong *n*-type character). Using the bandgap values obtained from the Tauc plot (2.65 eV for g- C_3N_4 and 1.76 eV for C_3N_5), the positions of the valence band edge for g- C_3N_4 and C_3N_5 were calculated to be +1.60 and +0.85 V vs Ag/AgCl, respectively. Since the standard band edge positions are usually expressed with reference to NHE, the CB and VB positions of g- C_3N_4 were calculated to -0.85 and +1.80 V vs NHE at pH-0, while CB and VB positions of C_3N_5 were found to be -0.72 and +1.04 V vs NHE at pH-0.

XPS valence band spectra of C_3N_5 was collected to get further information regarding the band structure (Figure 11a). The intersecting point obtained by extrapolation of XPS VB spectra on X and Y axis gave the value of valence band maximum (VB_{max}). The VB_{max} of C_3N_5 was calculated to be +0.95 eV which was approximately the same (+1.05 V) obtained from the Mott-Schottky measurements and UV-Vis data. Further, by using XPS VB and optical bandgap (1.76

Formatted: Highlight

eV) values, the CB_{min} and VB_{max} of C_3N_5 were calculated to be -0.79 and $+0.97$ eV, while for g- C_3N_4 , CB_{min} and VB_{max} positions were found to be -0.85 eV and $+1.80$ eV respectively. Figure 11b a schematic illustration of the density of states (DOS) distribution in C_3N_5 and g- C_3N_4 .

The dye degradation process begins with the reaction with $\bullet OH$ radical originating from photogenerated holes in the valence band of the semiconductor. The oxidation potential of water to generate $\bullet OH$ radical ($H_2O/\bullet OH$) is $+2.38$ V vs NHE at pH-0 which requires highly oxidative holes. Another route for the generation of $\bullet OH$ radicals is the reduction of O_2 to $O_2^{\bullet -}$ anion radical ($O_2/O_2^{\bullet -}$, -0.33 V vs NHE at pH-0) at the conduction band followed by reaction with protons to afford $\bullet OH$ radicals.^{63, 65} However for this process required protons should be derived from water oxidation (H_2O/O_2 , $+1.23$ V vs NHE at pH-0).^{64, 66} Unfortunately, the valence band position of C_3N_5 is just $+1.04$ V vs NHE which cannot facilitate water oxidation thus explaining the absence of photocatalytic activity for MB degradation. Nyquist plots of g- C_3N_4 and C_3N_5 determined with electrochemical impedance spectroscopy (EIS) under dark and AM1.5G irradiation demonstrate that the semicircle for C_3N_5 was larger than for g- C_3N_4 which represents a higher charge transfer resistance in C_3N_5 compared to g- C_3N_4 ; a higher charge carrier recombination is indicated in C_3N_5 (Figure S117).

Due to the unfavorable band edge positions of C_3N_5 ($CB = -0.71$ V and $VB = +1.04$ V vs NHE at pH-0), it is not able to function as a stand-alone catalyst for the photoelectrochemical splitting of water. However, the excellent visible light absorption of C_3N_5 encouraged us to investigate the photosensitizing effect of C_3N_5 to increase the photocatalytic performance of TiO_2 (a wide bandgap semiconductor).⁶⁷ The conduction band of C_3N_5 (-0.72 V vs NHE) was more negative than conduction band of TiO_2 (-0.1 V vs NHE) which favors transfer of photogenerated electrons in the CB of C_3N_5 to the CB of TiO_2 .⁶⁸ To measure photosensitizing performance, C_3N_5 .

Formatted: Highlight

and g-C₃N₄ powders were mixed with TiO₂ nanoparticles in α -terpineol solution (film-forming agent) followed by drop-casting on FTO:glass substrates coated with a thin (~ 50 nm) blocking layer of TiO₂. A three electrode setup consisting of the samples as the photoanode (working electrode), Pt as cathode (counter electrode) and Ag/AgCl reference electrode was used for photoelectrochemical water splitting experiments in 0.1 M Na₂SO₄ electrolyte, while a Class A solar simulator was used as the source of AM1.5G simulated sunlight (100 mW cm⁻²). Linear sweep voltammograms of electrodes consisting of C₃N₅ and pristine g-C₃N₄ samples mixed with TiO₂ NPs are shown in Figure 11a. It can be seen from Figure 11a that the photocurrent density for C₃N₅ sensitized TiO₂ was much higher than g-C₃N₄ sensitized TiO₂. The current density for C₃N₅ and g-C₃N₄ sample blended TiO₂ sample was found to be 152 and 100 μ A cm⁻² at an applied potential of +0.6 V *vs* NHE (or 1.23 V *vs* NHE). To probe the improved photosensitizing performance in the visible region, on-off experiments using a 450 nm LED (54.15 mW cm⁻²) were carried out which clearly show the alternate drop and rise in photocurrents in on-off cycles (Figure 11b). Figure 11b also shows that the magnitude of the photocurrent was higher for the C₃N₅ sample. A similar pattern in the on-off cycle was observed when samples were irradiated with 505 nm LED (40.48 mW cm⁻²) confirming the improved photosensitizing properties of C₃N₅ at longer wavelengths (Figure S128). Further, photoelectrochemical water splitting experiment carried out using Na₂S (2.0 mmol) as hole scavenger showed enhanced photocurrent density, reaching up to 465 μ A cm⁻² for C₃N₅ under AM 1.5 G irradiation (>420 nm) (Figure S13). Under identical conditions, the value of photocurrent density for g-C₃N₄ was found to be 373 μ A cm⁻² (Figure S13a). Similar pattern was followed at higher wavelengths and calculated current density for C₃N₅ was found to be 454 and 145 μ A cm⁻² at 450 and 505 nm, while for g-C₃N₄ the value of current density was found to be 275 and 80 μ A cm⁻² respectively (Figure S13b) Photocurrent response of

Formatted: Highlight

Formatted: Highlight

C_3N_5 as function of time during light on-off cycle doesn't change significantly compared to $g-C_3N_4$ which demonstrate resiliency of C_3N_5 under reaction conditions and charge flow (Figure S14). The maximum applied bias photon-to-current efficiency (ABPE) and incident photon-to-current efficiency (IPCE) achieved by C_3N_5 was 0.059 and 2.33% (at 450 nm) while these value for $g-C_3N_4$ was 0.048 and 1.41% (at 450 nm), respectively (Figure S13c and d).

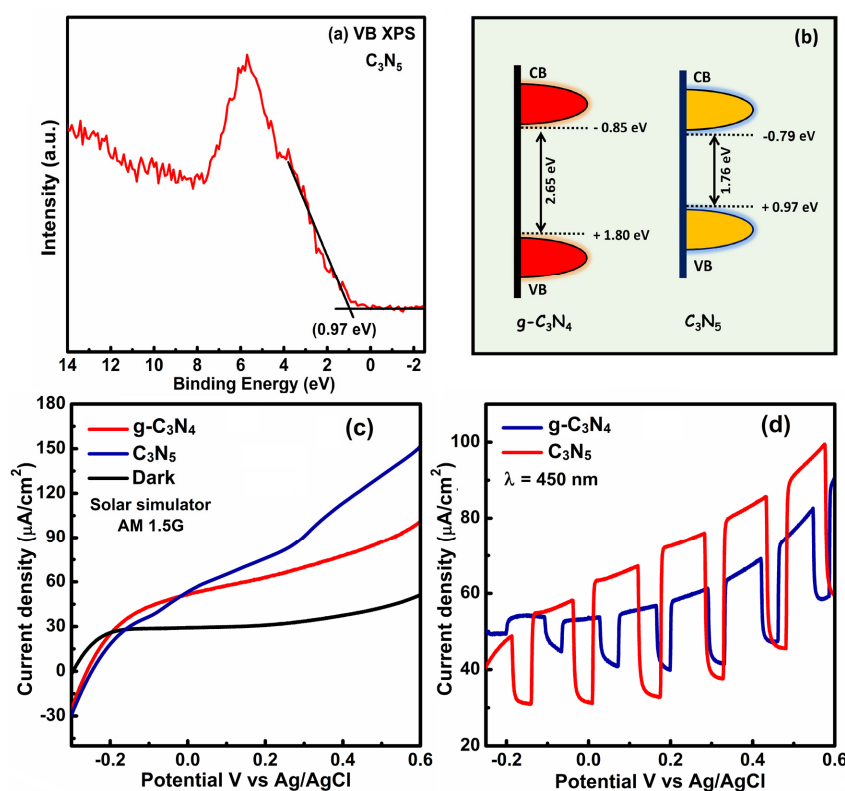


Figure 11. (a) XPS valence band spectra of C_3N_5 for determining energy levels (b) Density of state revealing band structure of $g-C_3N_4$ and C_3N_5 (c) Linear sweep voltammogram showing current-potential characteristics of $g-C_3N_4$ (blue) and C_3N_5 (red) measured in 0.1 M Na_2SO_4 solution AM1.5G light irradiation (100 mW cm^{-2})

and under dark condition (d) Light on-off showing photocurrent response vs applied voltage by using 450 nm wavelength light (54.15 mW cm^{-2}) for g-C₃N₄ (blue) and C₃N₅ (red).

To demonstrate the optoelectronic application of our newly synthesized graphenic semiconductor, we employed C₃N₅ as the electron transport layer (ETL) in MAPbBr₃ based perovskite solar cells and obtained a good result. Carbon-based materials have frequently been used as hole transport layers (HTLs) or hole collection electrodes in MAPbBr₃ based solar cells, but have almost never been used (effectively) as ETLs to boost the open circuit photovoltage. Using C₃N₅ as the ETL and with no optimization of any kind, we measured a V_{oc} of 1.3 V, J_{sc} of 7.5 mA cm^{-2} and a FF (fill factor) of 0.4 to obtain a power conversion efficiency (PCE) of 4.2 % (Figure S157 and S168 in Supporting Information). Some context is needed to appreciate the significance of the aforementioned result. Methylammonium lead bromide (MAPbBr₃) is a halide perovskite with an electronic bandgap of 2.23 eV which has two major advantages for solar cell applications in comparison to the more commonly used methylammonium lead iodide (MAPbI₃) – in theory, it enables the construction of much higher V_{oc} solar cells that can be used to power electrocatalytic and electrochemical reactions and secondly, MAPbBr₃ is known to have superior ambient stability (less moisture sensitivity) and operational stability (due to the absence of phase transitions and enhanced thermal stability at a high working temperature) compared to MAPbI₃.⁶⁹ However, until recently, most works in this area failed to achieve the expected high V_{oc} value, and the typical V_{oc} values obtained using were in the range 0.90-1.16 V.⁷⁰ The use of carbon-based charge transport layers has enabled a dramatic improvement in the performance of MAPbBr₃-based photovoltaic devices by generating photovoltages in excess of 1.3 V (as high as 1.6 V) without suffering a corresponding penalty in the short circuit current (J_{sc}). The first such report was by Wu *et al.*⁷¹ wherein indene-C60 bisadduct (ICBA) was used as the acceptor in conjunction

Formatted: Highlight

with MAPbBr₃ to realize a high V_{oc} perovskite solar cell. Shortly thereafter, Li *et al.* used carbon nanotubes as an efficient hole collector for MAPbBr₃ solar cells and achieved a V_{oc} of 1.4 V.⁷² MAPbBr₃ sandwiched between modified PEDOT:PSS (hole transport layer) and PC₆₁BM (electron transport layer) resulted in a solar cell with a V_{oc} of 1.52 V⁷³ while a graphitic carbon anode (with no hole transport layer) and TiO₂ electron transport layer were used by Liang *et al.* to realize a MAPbBr₃ solar cell with a V_{oc} as high as 1.57 V.⁷⁴

The origin of the poor V_{oc} values was poorly understood for a long time. Even now, there are two distinct explanations, one based on active layer material quality issues and another based on high interfacial recombination. For instance, vapor deposited MAPbBr₃ films were found to generate high V_{oc} values in comparison with solution-deposited films, which was attributed to the superior morphology and grain size in the vapor deposited films, and supported the explanation based invoking material quality.⁷⁵ The second explanation was supported by the observation of high V_{oc} values when hole transport layers with deep HOMO levels were used, indicating that the separation of the electron- and hole- quasi-Fermi levels at the charge extraction interfaces, was the controlling mechanism determining V_{oc} .⁷⁶ Our examination of MAPbBr₃ solar cells using C₃N₅ as the ETL provides a way to reconcile the above explanations. On the one hand, the high CB position of C₃N₅ is better aligned with the CB of MAPbBr₃, and enables an optimal value for the electron quasi-Fermi level at the perovskite- C₃N₅ interface. On the other hand, the low dark current observed using C₃N₅ ETL in comparison to both TiO₂ and g-C₃N₄ ETLs (Figure S179 in Supporting Information) indicates suppression of trap-mediated hopping through MAPbBr₃ due to the insertion of C₃N₅ as a midgap state-free barrier layer, thus enabling the circumventing of active layer material quality issues. In summary, it is noteworthy that an unoptimized ETL made with a

Formatted: Highlight

brand new semiconductor (C_3N_5) that was cast into films from a particulate suspension, generated a V_{oc} value of 1.3 V, higher than that generated by TiO_2 and $g-C_3N_4$ ETLs.

The photovoltaic performance of halide perovskite solar cells is highly dependent on grain size and defects free lattice states and presence of small numbers of defects and trap sites have a detrimental effect. The trap assisted recombinations can be minimized by passivating perovskite layer with graphenic materials due to their high carrier mobility and surface area materials which can efficiently capture charge are improve transportation behavior resulting in better photoconversion efficiency.⁷⁷ Further, incorporation of graphenic semiconductors with perovskite precursor provide crystallization surface which helps in increasing of grain size and minimize defects density at grain boundaries. The increased conjugation in C_3N_5 should lead to electron rich conductive surface with high charge carrier density and better carrier mobility than $g-C_3N_4$. To verify this assumption we have blended $MA_xFA_{1-x}Pb(I_{0.85}Br_{0.15})_3$ based perovskite with different wt% of C_3N_5 and $g-C_3N_4$. Under optimized conditions, 4 wt% doping of $g-C_3N_4$ and C_3N_5 with respect to PbX_2 was found best performing and C_3N_5 outperformed over $g-C_3N_4$ and bare PbX_2 based solar cell architecture attributed to better charge separation in more conjugated C_3N_5 scaffold and reduced trap sites.

Figure 12 shows the $J-V$ curves of the best performing solar cells devices based on undoped and doped perovskite layers while the photovoltaic performance of solar cells is summarized in table 4. Solar cells made with a compact undoped perovskite solar cell yielded a short circuit current density (J_{sc}) of about 20.344 mA/cm^2 , an open circuit voltage (V_{oc}) of 1.04 V and fill factor (FF) of about 66% resulting in the overall power conversion efficiency (PCE) of about 13.959%. While, perovskite solar cell made with $g-C_3N_4$ -doped perovskite layer showed a J_{sc} of 21.573 mA/cm^2 , V_{oc} of 1.03V and fill factor of about 69.1% and corresponding PCE of about 15.344%.

C₃N₅ doped perovskite solar cells displayed PCE value of 16.689% resulting from V_{oc} of 1.065V, J_{sc} of 22.87 mA/cm² and FF of 68.5%.

Capacitance-voltage measurement on fabricated devices with doped/undoped perovskite layer was measured at 10 kHz frequency in dark to determine bulk properties such as doping density (N_D) and energy equilibrium at the contacts which is related to the flat-band potential (V_{fb}).⁷⁸ Mott-Schottky plots for the devices made with doped and undoped perovskite layer are shown in Figure

13.5

$$\frac{1}{C_{sc}^2} = \frac{2}{e\epsilon_0\epsilon_r N_D} \left\{ (V - V_{FB}) - \frac{kT}{e} \right\} \quad (8)$$

$$N_D = \frac{2}{e\epsilon_0\epsilon_r n} \quad (9)$$

V_{fb} and N_D were calculated by using equation (8) and equation (9) respectively, where C_{sc} is the space-charge capacitance (*i.e.* film capacitance) per unit area; ϵ_r is the dielectric constant of the material, ϵ_0 is the vacuum permittivity, k is Boltzmann constant, T is temperature in Kelvin, e is the electron charge and V is the applied potential. The measured V_{fb} of bare undoped, g-C₃N₄-doped and C₃N₅ doped perovskite solar cell was found to be 1.12, 1.08 and 1.15 V respectively, while carrier concentration of the respective devices was found to be 1.74×10^{16} , 1.96×10^{16} and 1.36×10^{16} cm⁻³. This proves that doping perovskite layer with C₃N₅ significantly improves the charge transport in the device compared to the undoped and g-C₃N₄-doped devices.

To explore the charge transport characteristics, hole only devices with the architecture of FTO/PEDOT:PSS/Perovskite/Spiro-oMeTAD/Au were measured by the space charge limited current (SSLC) model described by the following equation.

$$J = \frac{9}{8L^3} \epsilon_0 \epsilon_r \mu V^2 \quad (10)$$

Where ϵ_0 , ϵ_r , μ and L are permittivity of the free space, relative permittivity of the perovskite, carrier mobility in the perovskite layer and thickness of perovskite layer respectively. The hole mobility in pure perovskite was found to be $2.55 \times 10^{-3} \text{ cm}^2/\text{s}$ while that of g-C₃N₄ and C₃N₅ doped perovskite was found to be $3.28 \times 10^{-3} \text{ cm}^2/\text{Vs}$ and $4.33 \times 10^{-3} \text{ cm}^2/\text{Vs}$ respectively (Figure S1922).

To get insight into the charge transfer properties of perovskite solar cells based on undoped and doped perovskite layer, solid-state impedance spectroscopy measurements in the frequency range from 0.1 Hz to 1 MHz at different applied bias under dark condition were performed. The resulting Nyquist plots were fitted with the circuit shown in inset of Figure 12c, where R_s is series resistance, R_{rec} and C represents the resistance and capacitance at the interface between the active layer and charge transport layer and Q is a constant phase element (CPE) with coefficient N . The resulting recombination resistance of different solar cells obtained after fitting the Nyquist plot observed from the low-frequency region at different voltage shown in Figure 12 (d-i). C₃N₅ doped device showed a higher value of R_{rec} compared to the g-C₃N₄ doped and undoped devices. As the electron and hole transporting layers for all kind of devices are same, the difference in R_{rec} is mostly governed by the change in the interfacial property of perovskite layer induced by doping with C₃N₅ and g-C₃N₄. Interfacial recombination is inversely proportional to the recombination resistance, therefore, it can be concluded that the interfacial charge recombination in perovskite solar cells significantly gets suppressed by doping with MHP while it increases by doping with g-C₃N₄ resulting in an improved V_{oc} in C₃N₅ based device followed by the undoped and doped devices.

Formatted: Highlight

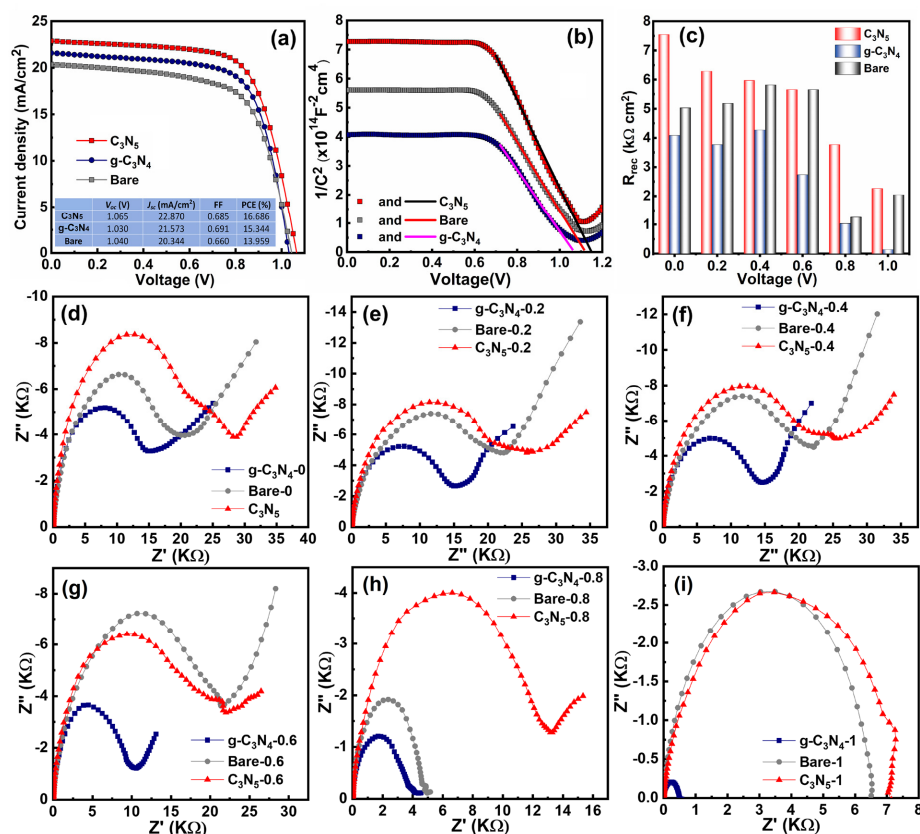


Figure 12. (a) Current-voltage characteristics of perovskite solar cells made with bare PbX₂, 4 wt% of g-C₃N₄ and C₃N₅ under AM1.5 G one sun illumination. (b) Mott-Schottky plot of the perovskite solar cells based undoped and g-C₃N₄/C₃N₅-doped perovskite active layers. (c) Recombination resistance of perovskite solar cell based on undoped and doped Perovskite layer with CN and MHP in dark. The corresponding equivalent circuit is shown in insets where Rs is series resistance, C is high-frequency capacitance, R is recombination resistance, and Q is a constant phase element (CPE) with coefficient N. (d-i) Nyquist plots for perovskite solar cells made with bare PbX₂, g-C₃N₄ and C₃N₅ doping under dark condition at 0.0, 0.2, 0.4, 0.6, 0.8 and 1.0 V.

Table 4. Photovoltaic performance of HPSCs made with bare PbX₂, 4 wt% g-C₃N₄ and C₃N₅ in PbX₂ solution under AM1.5 G solar simulated light.

		<i>V</i> _{oc} (V)	<i>J</i> _{sc} (mA/cm ²)	FF	PCE (%)
C ₃ N ₅	Maximum	1.065	22.870	0.685	16.686
	Average	1.026±0.043	22.560±1.039	0.654±0.044	15.142±1.442
g-C ₃ N ₄	Maximum	1.030	21.573	0.691	15.344
	Average	0.984±0.042	21.204±0.565	0.670±0.017	13.981±0.949
Bare	Maximum	1.040	20.344	0.660	13.959
	Average	1.041±0.035	20.394±0.200	0.647±0.020	13.713±0.245

The low band gap and extended π conjugation of C₃N₅ makes it an excellent candidate to harvest solar light to drive visible light induced catalytic reaction. Recently plasmonic materials capable of generating hot electrons, coupled with graphenic materials has shown wide potential in plasmon-exciton co-induced surface catalytic reactions.⁷⁹ The plasmon-exciton coupling for co-driven chemical reactions can be measured by surface enhanced Raman spectroscopy (SERS).⁸⁰ To probe the viability C₃N₅ for promoting chemical reaction on its surface, the transformation of 4NBT (4-nitrobenzenethiol) to DMAB (4,4'-dimercaptoazobenzene) was chosen as model reaction while silver nanocubes (AgNC)⁸¹ were used as plasmonic material. The comparative SERS spectra of NBT adsorbed on bare AgNC, and AgNC decorated on g-C₃N₄ mW and C₃N₅ using 532 nm laser and 1 mW laser power are presented in Figure 13a. Normal Raman spectra of the pristine 4NBT powder show three main Raman signals at 1101, 1332 and 1576 cm⁻¹ assigned to S-C

Formatted: Highlight

stretch, NO₂ vibration and C=C stretch respectively.⁸² After irradiating with 532 nm laser with a 1 mW power intensity the N-O vibration was decreased and new peaks at 1142 (C-N stretch), 1389 and 1438 (N=N stretch) cm⁻¹ corresponded to DMAB *ag* modes emerged demonstrating conversion of 4NBT to DMAB.⁸³ For bare AgNC the drop in 4NBT peak was not significant which show inefficient surface-plasmon-to-hot-electron conversion to promote plasmon-driven chemical reaction. The AgNC/g-C₃N₄ show a slight lowering of 4NBT peak intensity and rise in DMAB peaks, however, the peak was not disappeared suggesting incomplete transformation at lower laser power. While for AgNC/C₃N₅ the N-O vibration peak was completely disappeared at 1.0 mW laser power. Further, we have tested laser power dependent SERS spectra on NBT adsorbed samples which demonstrate complete disappearance of 4NBT peaks for Ag/C₃N₅ even at 0.7 mW while bare Ag and AgNC/g-C₃N₄ system could not achieve complete degradation even at 10 mW laser power (Figure 13 b-d). Magnified SERS spectra of Ag/C₃N₅, in 1270-1470 cm⁻¹ region show a gradual decrease in N-O vibration peak as a function of laser power AgNC and completely disappear at 1.0 mW (Figure S204). While sluggish transformation rate was observed for AgNC/g-C₃N₄ and AgNC as evident from the increase in 4NBT peak at 1332 cm⁻¹ along with DMAB peak at 1389 and 1438 cm⁻¹ as a function of laser intensity. The excellent conversion efficiency of AgNC/C₃N₅ assembly was attributed due to better plasmon-to-electron conversion efficiency on conjugated C₃N₅'s surface which lead to a high-density hot electrons to facilitate high catalytic conversion.^{79b}

Formatted: Highlight

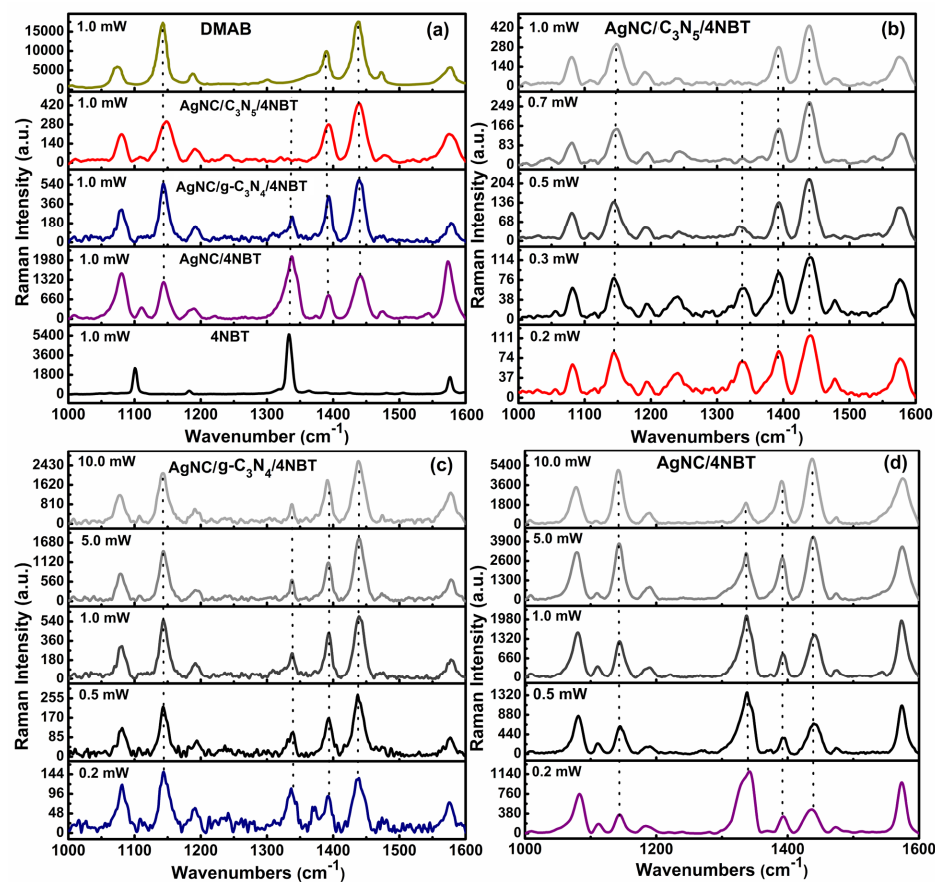


Figure 13. (a) Raman spectrum of pristine 4NBT (black), DMAB (yellow) and comparison of SERS spectra of plasmon-exciton co-induced surface catalytic reaction of 4NBT to DMAB on AgNC (purple), AgNC/g-C₃N₄ (blue) and AgNC/C₃N₅ (red) under 532 nm laser irradiation at 1.0 mW power and 60 s accumulation time and SERS spectra as function of laser power for plasmon-exciton co-induced surface catalytic transformation of 4NBT to DMAB on (b) AgNC/C₃N₅ (c) AgNC/g-C₃N₄ and (d) AgNC. The gradual lightening of color as a function of laser power represents the transformation of 4NBT to DMAB.

We performed thermogravimetric analysis (TGA) analysis of $g-C_3N_4$ samples to determine the thermal stability of materials (Figure S2143). The TGA thermogram of $g-C_3N_4$ shows two weight loss regimes in the range of 60-150 °C and 500-740 °C (Figure S21a). The first small weight loss (~6%) in the range of 60-150 °C was due to loss of surface adsorbed water molecules. The second major weight loss started from 550 °C, shows slow weight loss (~8%) up to 635 °C due to loss of NH_2 and condensation of heptazine units followed by almost ~70% sharp weight loss in the range of 635-740 °C due to degradation of heptazine moieties.⁸⁴ Following that, a steady weight loss was observed up to 900 °C due to the removal of residual carbon material. For C_3N_5 , an initial small weight loss of 6% in the range of 60-150 °C was attributed due to loss of surface adsorbed and intercalated water (Figure S21b). A second steady weight loss (~34%) observed in the temperature range of 420-630 °C was assigned to loss of bridging azo nitrogens ($-N=N-$) and edge decorated $-NH_2$ nitrogens. The absence of any sharp weight loss for azo nitrogens demonstrates that azo nitrogens were not localized but present in a crosslinked heptazine network. Previous reports on azo linked polymer also demonstrated excellent thermal stability of such polymers due to the formation of a rigid structure.⁸⁵ Further, the observed weight loss value was in close agreement with expected weight loss value for azo nitrogen (33.5%) calculated by considering removal of three azo nitrogens ($-N=N-$ shared by two heptazine) from azo bridged C_6N_{10} unit, leaving behind C_6N_7 heptazine unit. These results further validated the presence of azo nitrogens in C_3N_5 polymer. Approximately 38% sharp weight loss in 630-720 °C region was assigned to degradation of heptazine ring system followed by slow weight loss due up to 900 °C for residual carbon. Further, to investigate the nature of the product formed at high temperature, we annealed the sample in a closed evacuated quartz tube at 800 °C for 4 h. The orange product turned black and stuck to the wall of the tubes. Raman analysis of the product showed specific D, G band along with the 2D

Formatted: Highlight

Formatted: Highlight

Formatted: Highlight

band and demonstrate its transformation into N doped graphene/carbon (Figure S22). Previous reports also demonstrate the transformation of carbon nitride-based materials/nitrogenous precursors into N-graphene/N-carbon at higher temperatures.

To understand charge carrier dynamics and recombination mechanisms in C_3N_5 , the surface potential changes of the samples under dark and under laser illumination at different wavelengths, were measured using Kelvin Probe Force Microscopy (KPFM) as illustrated in Figure 14. The surface topographical AFM image of $g-C_3N_4$ and C_3N_5 thin films deposited on bare FTO reveals an average roughness of 20.4 and 19 nm respectively (Figure 14ai and bi). Figure 14(aii)-(av) and (bii)-(bv) displays the surface potential map of $g-C_3N_4$ and C_3N_5 samples under dark, 635, 520 and 450 nm respectively. The FTO was grounded and behaves as an electron sink for photogenerated charges, leaving holes behind. The surface potential map under dark for both $g-C_3N_4$ and C_3N_5 shows even distribution of charge all over the surface of samples, (Figure 14(aii) and (bii)). After illumination with 635 nm laser the contrast of blue spots (positive potential shift) in the surface potential map was increased for both $g-C_3N_4$ and C_3N_5 , however, this change was much intense for C_3N_5 . Under 520 nm light, the density of blue spots was slightly higher for $g-C_3N_4$ than C_3N_5 which drastically increased under 450 nm illumination (Figure 14a (aiv)-av) and Figure 14b (biv)-(bv). These observations demonstrate that highest charge generation and accumulation on the surface was at 450 nm for $g-C_3N_4$ and at 635 nm for C_3N_5 while remaining moderate for both at 520 nm. Further, values of surface potential measured by KPFM under dark condition were found to be +156 and +45 mV for $g-C_3N_4$ and C_3N_5 respectively, which agreed well with the increased electron density on C_3N_5 than $g-C_3N_4$ due to contribution of charge from azo motif to heptazine ring system *via* extended orbital overlap (Figure 14c and d). The high surface negative charge of C_3N_5 was also confirmed by zeta potential measurements (Figure S8+9). After illumination with

Formatted: Highlight

Formatted: Highlight

Formatted: Highlight

450 nm light, the surface potential was negatively shifted reaching maximum +40 mV for g-C₃N₄ and +25 mV for C₃N₅. Higher change in contact potential difference (CPD) or SP i.e. 102 mV for g-C₃N₄ was observed due to good absorption at 450 nm for generation of electron-hole pairs and accumulation of negative charge on the sample surface. The broad surface potential peaks and significantly larger CPD shift for g-C₃N₄ were attributed possibly due to the longer lifetime (as confirmed by TRPL, Figure 8a) of g-C₃N₄ charge carriers resulting into delayed recombination of accumulated charge. Under 520 nm illumination, the surface potential values for g-C₃N₄ and C₃N₅ were measured to be 123 and 8 mV, while the change in SP was found to be 33 and 37 mV, respectively. For g-C₃N₄, relatively small CPD shifting at 520 nm can be explained due to its limited absorption at 520 nm wavelength generating fewer numbers of excitons, while in C₃N₅ most of the photogenerated charge get recombined due to faster recombination rate. Interestingly, C₃N₅ show unusually high SP shift (77 mV) at 635 nm, while g-C₃N₄ show explicitly small CPD shift (30 mV). Exceptional high SP shift at 635 nm, demonstrating azo motif playing a certain role in charge carrier generation and stabilization at a longer wavelength. Azo bridged aromatic compounds are well known for their visible light absorption due to the presence of azo chromophore (-N=N-) in conjugation with aromatic units. The n→π* transition corresponding to azo nitrogen nonbonding orbital to the π* orbital of conjugated nitrogens in azo moiety occurs at low energy giving visible light absorption.⁸⁶ In C₃N₅ where electron withdrawing heptazine units (C₆H₇) were bridged together with azo bonds, a these low energy transition can take place at 635 nm resulting into increase CPD shift at 635 nm. The high surface potential of C₃N₅ at 635 nm validates its potential to generate excitons at longer wavelengths.

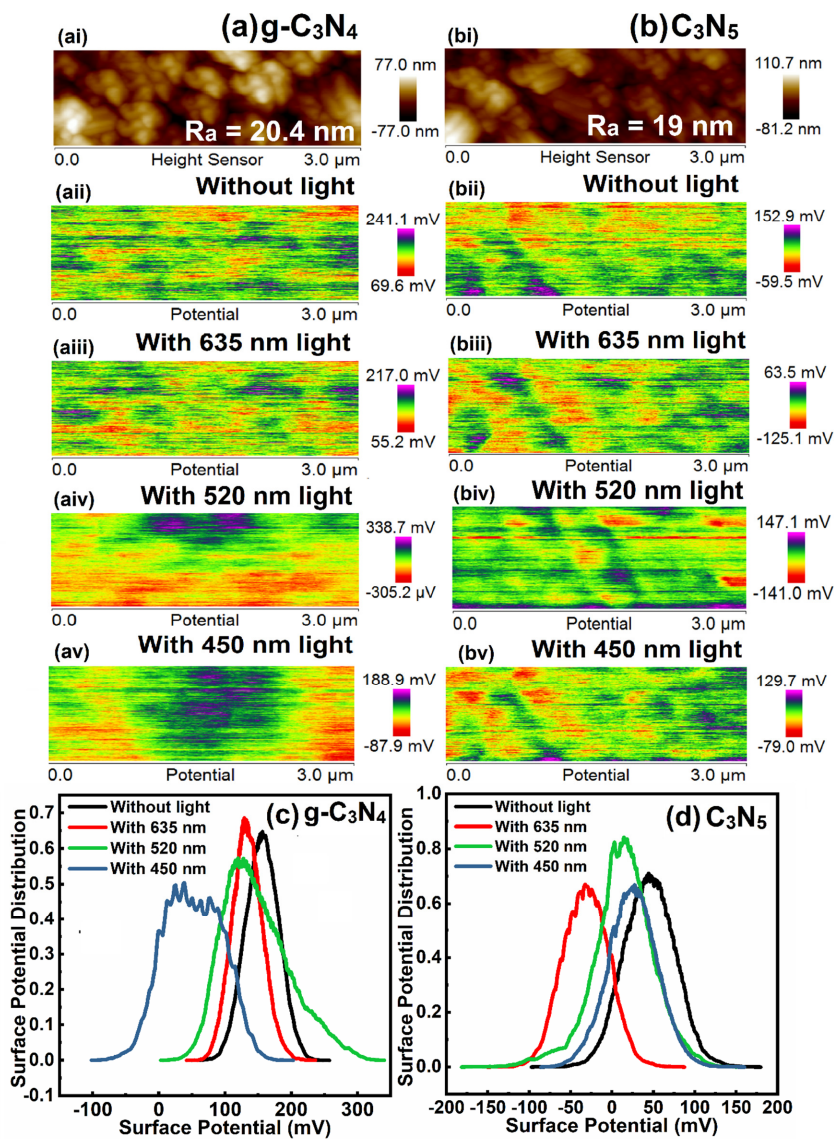


Figure 14. (a) and (b) Topographical AFM images (ai), (bi) and Surface potential maps of g-C₃N₄ and C₃N₅ samples deposited on FTO (aii) and (bii) without light, (aiii) and (biii) with 635 nm laser, (aiv) and (biv) with 520 nm laser, (av) and (bv) with 450 nm laser in sequence of top to bottom and surface potential distribution of (c) g-C₃N₄ and (d) C₃N₅ samples deposited on FTO under dark conditions, under illumination with 635, 520 and 450 nm laser.

3. Conclusion

We report the synthesis of a modified carbon nitride framework C₃N₅ polymer containing exceptionally high N:C atomic ratio (5:3) melem hydrazine as the monomeric unit. Extensive characterization of C₃N₅ with XPS, EELS, NMR spectroscopy and elemental analysis suggested the presence of heptazine moiety bridged by azo nitrogens in the C₃N₅ framework. Due to the overlap between the π orbitals of azo-bridged units and the π -conjugated network of the heptazine unit, the bandgap of C₃N₅ material was significantly reduced which, in turn, enabled optical absorption extended up to 700 nm and a bandgap of 1.76 eV. The position of the valence band in C₃N₅ was raised (+1.04 V vs NHE) in comparison to g-C₃N₄ (+1.80 V vs NHE) and C₃N₅ displayed excellent photosensitizing behavior to sensitize TiO₂ at longer wavelengths (505 nm) to facilitate photoelectrochemical water splitting. Due to the increased nitrogen content and the availability of electron rich basic nitrogen sites, C₃N₅ materials displayed astonishing dye adsorption performance for methylene blue removal reaching 90 % adsorption-desorption equilibria within 1 min and complete adsorption-desorption equilibria within 10 min. In conjunction with Ag nanocubes, C₃N₅ displayed excellent photocatalytic activity for the plasmon-exciton (plexciton) co-driven reduction of 4-nitrobenzenethiol to 4,4'-dimercaptoazobenzene. A prototypical solar cell device using C₃N₅ ETL and MAPbBr₃ displayed an improved V_{oc} of 1.3 V and power conversion

efficiency (PCE) of 4.2 % higher than g-C₃N₄ ETL. C₃N₅ blended with MA_xFA_{1-x}Pb(I_{0.85}Br_{0.15})₃ perovskite active layer achieved a photoconversion efficiency (PCE) as high as 16.7 %.

Supporting Information:

Experimental details; chemical structures; Supporting Figures (Fig. S1-S22); XPS, ssNMR, Raman, electrochemical characterization (Mott-Schottky, EIS), PL, Fluorescence lifetime imaging, Zeta potential, EELS, TGA, Photoelectrochemical water splitting results (under AM 1.5G irradiation, LEDs PCE, IPCE, APCE, i-t curve), solar cell results (*J-V* curves, action spectra) and plexitonic performance (SERS spectra)

Acknowledgements

We would like to thank the Natural Sciences and Engineering Research Council of Canada (NSERC), the National Research Council Canada (NRC), Future Energy Systems (FES) and CMC Microsystems for direct and indirect (equipment use) financial support. UKT is supported by a graduate student scholarship from Alberta Innovates. Some device fabrication and testing used research infrastructure made possible by a Leaders Opportunity Fund grant to KS from the Canada Foundation for Innovation and the Alberta Small Equipment Grants Program. We acknowledge use of the following facilities: the National Research Council - National Institute for Nanotechnology (NRC-NINT) Electron Microscopy Lab, the Cell Imaging Facility, the Analytical Chemistry Laboratory and the University of Alberta Nanofab. Drs. Shihong Xu[†] and Wayne Moffat are kindly acknowledged for assisting in He-ion imaging, CHNS elemental analysis, respectively. We thank Prof. Alkiviathes Meldrum for allowing the use of his lab to perform PL lifetime measurements.

References

1. (a) Brabec, C. J.; Winder, C.; Sariciftci, N. S.; Hummelen, J. C.; Dhanabalan, A.; van Hal, P. A.; Janssen, R. A.; *A low bandgap semiconducting polymer for photovoltaic devices and infrared emitting diodes*. *Advanced Functional Materials* **2002**, *12* (10), 709-712. (b) Kim, J.-S.; Lu, L.; Sreearunothai, P.; Seeley, A.; Yim, K.-H.; Petrozza, A.; Murphy, C. E.; Beljonne, D.; Cornil, J.; Friend, R. H.; *Optoelectronic and Charge Transport Properties at Organic—Organic Semiconductor Interfaces: Comparison between Polyfluorene-Based Polymer Blend and Copolymer*. *Journal of the American Chemical Society* **2008**, *130* (39), 13120-13131. (c) Liang, Y. Y.; Yu, L. P.; *A New Class of Semiconducting Polymers for Bulk Heterojunction Solar Cells with Exceptionally High Performance*. *Accounts Chem. Res.* **2010**, *43* (9), 1227-1236. (d) Bandara, J.; Shankar, K.; Grimes, C. A.; Thelakkat, M.; *Efficient and stable, structurally inverted poly (3-hexylthiophen):[6,6]-phenyl C61 butyric acid methyl ester heterojunction solar cells with fibrous-like poly (3-hexylthiophen)*. *Thin Solid Films* **2011**, *520* (1), 582-590. (e) Baeg, K. J.; Caironi, M.; Noh, Y. Y.; *Toward Printed Integrated Circuits based on Unipolar or Ambipolar Polymer Semiconductors*. *Advanced Materials* **2013**, *25* (31), 4210-4244. (f) Hu, X. W.; Dong, Y.; Huang, F.; Gong, X.; Cao, Y.; *Solution-Processed High-Detectivity Near-Infrared Polymer Photodetectors Fabricated by a Novel Low-Bandgap Semiconducting Polymer*. *J. Phys. Chem. C* **2013**, *117* (13), 6537-6543. (g) Scaccabarozzi, A.; Stingelin, N.; *Semiconducting-insulating polymer blends for optoelectronic applications—a review of recent advances*. *Journal of Materials Chemistry A* **2014**, *2* (28), 10818-10824. (h) Fokina, A.; Lee, Y.; Chang, J. H.; Park, M.; Sung, Y.; Bae, W. K.; Char, K.; Lee, C.; Zentel, R.; *The Role of Emission Layer Morphology on the Enhanced Performance of Light Emitting Diodes Based on Quantum Dot Semiconducting Polymer Hybrids*. *Adv. Mater. Interfaces* **2016**, *3* (18), 1600279. (i) Gao, L.; Zhang, Z. G.; Bin, H.; Xue, L.; Yang, Y.; Wang, C.; Liu, F.; Russell, T. P.; Li, Y.; *High-Efficiency Nonfullerene Polymer Solar Cells with Medium-Bandgap Polymer Donor and Narrow-Bandgap Organic Semiconductor Acceptor*. *Advanced Materials* **2016**, *28* (37), 8288-8295. (j) Mola, G. T.; Dlamini, W. E.; Oseni, S. O.; *Improving optical absorption bandwidth using bi-layer bulk heterojunction organic photoactive medium*. *J. Mater. Sci.: Mater. Electron.* **2016**, *27* (11), 11628-11633. (k) Chang, P.-H.; Tsai, Y.-C.; Shen, S.-W.; Liu, S.-Y.; Huang, K.-Y.; Li, C.-S.; Chang, H.-P.; Wu, C.-I.; *Highly Sensitive Graphene Semiconducting Polymer Hybrid Photodetectors with Millisecond Response Time*. *ACS Photonics* **2017**, *4* (9), 2335-2344. (l) Schroeder, B. C.; Kurosawa, T.; Fu, T. R.; Chiu, Y. C.; Mun, J.; Wang, G. J. N.; Gu, X. D.; Shaw, L.; Kneller, J. W. E.; Kreouzis, T.; Toney, M. F.; Bao, Z. A.; *Taming Charge Transport in Semiconducting Polymers with Branched Alkyl Side Chains*. *Advanced Functional Materials* **2017**, *27* (34), 1701973. (m) Zhao, W.; Li, S.; Zhang, S.; Liu, X.; Hou, J.; *Ternary polymer solar cells based on two acceptors and one donor for achieving 12.2% efficiency*. *Advanced Materials* **2017**, *29* (2), 1604059. (n) Kang, M. J.; Khim, D.; Kim, J.; Lee, H. J.; Jo, J. Y.; Baeg, K. J.; Kim, D. Y.; *Tuning non-volatile memory characteristics via molecular doping of polymer semiconductors based on ambipolar organic field-effect transistors*. *Org. Electron.* **2018**, *58*, 12-17. (o) Brabec, C. J.; Winder, C.; Sariciftci, N. S.; Hummelen, J. C.; Dhanabalan, A.; van Hal, P. A.; Janssen, R. A. J.; *A low bandgap semiconducting polymer for photovoltaic devices and infrared emitting diodes*. *Advanced Functional Materials* **2002**, *12* (10), 709-712. (p) Kim, J. S.; Lu, L.; Sreearunothai, P.; Seeley, A.; Yim, K. H.; Petrozza, A.; Murphy, C. E.; Beljonne, D.; Cornil, J.; Friend, R. H.; *Optoelectronic and charge transport properties at organic organic*

semiconductor interfaces: Comparison between polyfluorene based polymer blend and copolymer. *Journal of the American Chemical Society* **2008**, 130 (39), 13120-13131. (q) Bandara, J.; Shankar, K.; Grimes, C. A.; Thelakkat, M., Efficient and stable, structurally inverted poly(3-hexylthiophene)-6,6-phenyl-C61-butyric acid methyl ester heterojunction solar cells with fibrous like poly(3-hexylthiophene). *Thin Solid Films* **2011**, 520 (4), 582-590. (r) Scaccabarozzi, A. D.; Stingelin, N., Semiconducting-insulating polymer blends for optoelectronic applications a review of recent advances. *Journal of Materials Chemistry A* **2014**, 2 (28), 10818-10824. (s) Gao, L.; Zhang, Z. G.; Bin, H. J.; Xue, L. W.; Yang, Y. K.; Wang, C.; Liu, F.; Russell, T. P.; Li, Y. F., High-Efficiency Nonfullerene Polymer Solar Cells with Medium-Bandgap Polymer Donor and Narrow-Bandgap Organic Semiconductor Acceptor. *Advanced Materials* **2016**, 28 (37), 8288-8295. (t) Chang, P. H.; Tsai, Y. C.; Shen, S. W.; Liu, S. Y.; Huang, K. Y.; Li, C. S.; Chang, H. P.; Wu, C. I., Highly Sensitive Graphene Semiconducting Polymer Hybrid Photodetectors with Millisecond Response Time. *ACS Photonics* **2017**, 4 (9), 2335-2344. (u) Zhong, L.; Gao, L.; Bin, H. J.; Hu, Q.; Zhang, Z. G.; Liu, F.; Russell, T. P.; Zhang, Z. J.; Li, Y. F., High-Efficiency Ternary Nonfullerene Polymer Solar Cells with Two Polymer Donors and an Organic Semiconductor Acceptor. *Adv. Energy Mater.* **2017**, 7 (44), 1602215.

2. —Po, R.; Bianchi, G.; Carbonera, C.; Pellegrino, A., "All That Glisters Is Not Gold": An Analysis of the Synthetic Complexity of Efficient Polymer Donors for Polymer Solar Cells. *Macromolecules* **2015**, 48 (3), 453-461.

3. —(a) Di Pietro, R.; Fazzi, D.; Kehoe, T. B.; Sirringhaus, H., Spectroscopic investigation of oxygen and water induced electron trapping and charge transport instabilities in n-type polymer semiconductors. *Journal of the American Chemical Society* **2012**, 134 (36), 14877-14889. (b) Chen, C. Y.; Tsao, C. S.; Huang, Y. C.; Liu, H. W.; Chiu, W. Y.; Chuang, C. M.; Jeng, U. S.; Su, C. J.; Wu, W. R.; Su, W. F.; Wang, L., Mechanism and control of the structural evolution of a polymer solar cell from a bulk heterojunction to a thermally unstable hierarchical structure. *Nanoscale* **2013**, 5 (16), 7629-7638. (c) Phan, H.; Wang, M.; Bazan, G. C.; Nguyen, T. Q., Electrical Instability Induced by Electron Trapping in Low-Bandgap Donor-Acceptor Polymer Field-Effect Transistors. *Advanced Materials* **2015**, 27 (43), 7004-7009; (d) Ye, Z.; Cui, H.; Yang, X.; Qiu, F., Charge injection promoted electrohydrodynamic instabilities in poly(3-hexylthiophene) thin films. *Journal of Materials Chemistry C* **2015**, 3 (9), 1949-1956. (e) Pearson, A. J.; Hopkinson, P. E.; Couderc, E.; Domanski, K.; Abdi-Jalebi, M.; Greenham, N. C., Critical light instability in CB/DIO processed PBDTTT-EFT: PC71BM organic photovoltaic devices. *Org. Electron.* **2016**, 30, 225-236. (f) Hsieh, Y. J.; Huang, Y. C.; Liu, W. S.; Su, Y. A.; Tsao, C. S.; Rwei, S. P.; Wang, L., Insights into the Morphological Instability of Bulk Heterojunction PTB7-Th/PCBM Solar Cells upon High Temperature Aging. *ACS Applied Materials & Interfaces* **2017**, 9 (17), 14808-14816. (g) Un, H. I.; Zheng, Y. Q.; Shi, K.; Wang, J. Y.; Pei, J., Air and Active Hydrogen Induced Electron Trapping and Operational Instability in n-Type Polymer Field-Effect Transistors. *Advanced Functional Materials* **2017**, 27 (11), 1605058. (h) Di Pietro, R.; Fazzi, D.; Kehoe, T. B.; Sirringhaus, H., Spectroscopic Investigation of Oxygen and Water Induced Electron Trapping and Charge Transport Instabilities in n-type Polymer Semiconductors. *Journal of the American Chemical Society* **2012**, 134 (36), 14877-14889. (i) Kim, S. H.; Yoon, W. M.; Jang, M.; Yang, H.; Park, J. J.; Park, C. E., Damage-free hybrid encapsulation of organic field-effect transistors to reduce environmental instability. *Journal of Materials Chemistry* **2012**, 22 (16), 7731-7738. (j) Phan, H.; Wang, M.; Bazan, G. C.; Nguyen, T. Q., Electrical Instability Induced by Electron Trapping in Low-Bandgap Donor-

3. ~~Acceptor Polymer Field-Effect Transistors. *Advanced Materials* **2015**, 27(43), 7004-7004.~~ (k) Ye, Z.; Cui, H. N.; Yang, X. B.; Qiu, F., ~~Charge injection promoted electrohydrodynamic instabilities in poly(3-hexylthiophene) thin films. *Journal of Materials Chemistry C* **2015**, 3(9), 1949-1956.~~ (l) Pearson, A. J.; Hopkinson, P. E.; Couderc, E.; Domanski, K.; Abdi-Jalebi, M.; Greenham, N. C., ~~Critical light instability in CB/DIO-processed PBDTTT-EFT:PC71BM organic photovoltaic devices. *Org. Electron.* **2016**, 30, 225-236.~~ (m) Un, H. I.; Zheng, Y. Q.; Shi, K.; Wang, J. Y.; Pei, J., ~~Air and Active Hydrogen-Induced Electron Trapping and Operational Instability in n-Type Polymer Field-Effect Transistors. *Advanced Functional Materials* **2017**, 27(41), 1605058.~~
4. ~~—(a) Matthews, J. R.; Niu, W. J.; Tandia, A.; Wallace, A. L.; Hu, J. Y.; Lee, W. Y.; Giri, G.; Mannsfeld, S. C. B.; Xie, Y. T.; Cai, S. C.; Fong, H. H.; Bao, Z. N.; He, M. Q., Scalable Synthesis of Fused Thiophene Diketopyrrolopyrrole Semiconducting Polymers Processed from Nonchlorinated Solvents into High Performance Thin Film Transistors. *Chemistry of Materials* **2013**, 25(5), 782-789.~~ (b) Marzano, G.; Ciasca, C. V.; Babudri, F.; Bianchi, G.; Pellegrino, A.; Po, R.; Farinola, G. M., ~~Organometallic Approaches to Conjugated Polymers for Plastic Solar Cells: From Laboratory Synthesis to Industrial Production. *Eur. J. Org. Chem.* **2014**, 2014(30), 6583-6614.~~ (c) Bohra, H.; Wang, M. F., ~~Direct C-H arylation: a "Greener" approach towards facile synthesis of organic semiconducting molecules and polymers. *Journal of Materials Chemistry A* **2017**, 5(23), 11550-11571.~~
5. ~~—(a) Zhang, X. M.; Wang, A. Z.; Zhao, M. W., Spin-gapless semiconducting graphitic carbon nitrides: A theoretical design from first principles. *Carbon* **2015**, 84, 1-8.~~ (b) Berger, D.; Ratsch, C., ~~Line defects in graphene: How doping affects the electronic and mechanical properties. *Phys. Rev. B* **2016**, 93(23)235441.~~
6. ~~—(a) Kumar, P.; Boukherroub, R.; Shankar, K., Sunlight-driven water-splitting using two dimensional carbon-based semiconductors. *Journal of Materials Chemistry A* **2018**, 6, 12876-12931.~~ (b) Linley, S.; Liu, Y.; Ptacek, C. J.; Blowes, D. W.; Gu, F. X., ~~Recyclable Graphene-Oxide-Supported Titanium Dioxide Photocatalysts with Tunable Properties. *ACS Applied Materials & Interfaces* **2014**, 6(7), 4658-4668.~~ (c) Putz, M. V.; Buzatu, D. L.; Mirica, M. C.; Ori, O., ~~Quantum particles on graphenic systems. Part 1. roadmap for semiconductor based graphenes. *Fuller. Nanotub. Carbon Nanostruct.* **2018**, 26(5), 303-314.~~
7. ~~—(a) Sridharan, K.; Kuriakose, T.; Philip, R.; Park, T. J., Transition metal (Fe, Co and Ni) oxide nanoparticles grafted graphitic carbon nitrides as efficient optical limiters and recyclable photocatalysts. *Applied Surface Science* **2014**, 308, 139-147.~~ (b) Liu, J.; Liu, Y.; Liu, N.; Han, Y.; Zhang, X.; Huang, H.; Lifshitz, Y.; Lee, S.-T.; Zhong, J.; Kang, Z., ~~Metal-free efficient photocatalyst for stable visible water splitting via a two-electron pathway. *Science* **2015**, 347(6225), 970.~~ (c) Kumar, P.; Thakur, U. K.; Alam, K.; Kar, P.; Kisslinger, R.; Zeng, S.; Patel, S.; Shankar, K., ~~Arrays of TiO₂ nanorods embedded with fluorine doped carbon nitride quantum dots (CNFQDs) for visible light driven water splitting. *Carbon* **2018**, 137, 174-187.~~
8. ~~—Wen, J.; Xie, J.; Chen, X.; Li, X., A review on g-C₃N₄ based photocatalysts. *Applied Surface Science* **2017**, 391, 72-123.~~
9. ~~—(a) Zhou, Z.; Zhang, Y.; Shen, Y.; Liu, S.; Zhang, Y., Molecular engineering of polymeric carbon nitride: advancing applications from photocatalysis to biosensing and more. *Chemical Society Reviews* **2018**, 47(7), 2298-2321.~~ (b) Ong, W.-J.; Tan, L.-L.; Ng, Y. H.; Yong, S.-T.; Chai, S.-P., ~~Graphitic carbon nitride (g-C₃N₄)-based photocatalysts for artificial photosynthesis and environmental remediation: are we a step closer to achieving sustainability? *Chemical*~~

Formatted: Font: Italic

Formatted: Font: Not Bold, Italic

- Reviews* **2016**, *116*-(12), 7159-7329. (c) Zheng, Y.; Lin, L.; Wang, B.; Wang, X., *Graphitic carbon nitride polymers toward sustainable photoredox catalysis*. *Angew. and Chem. International Edition* **2015**, *54*-(44), 12868-12884.
10. (a) Cao, S.; Low, J.; Yu, J.; Jaroniec, M., *Polymeric photocatalysts based on graphitic carbon nitride*. *Advanced Materials* **2015**, *27*-(13), 2150-2176. (b) Wang, Y.; Wang, X.; Antonietti, M., *Polymeric graphitic carbon nitride as a heterogeneous organocatalyst: from photochemistry to multipurpose catalysis to sustainable chemistry*. *Angew. and Chem. International Edition* **2012**, *51*-(1), 68-89. (c) Wang, Y.; Zhang, J.; Wang, X.; Antonietti, M.; Li, H., *Boron and Fluorine-Containing Mesoporous Carbon Nitride Polymers: Metal-Free Catalysts for Cyclohexane Oxidation*. *Angew. and Chem. International Edition* **2010**, *49*-(19), 3356-3359.
11. (a) Zhang, Y.; Mori, T.; Ye, J.; Antonietti, M., *Phosphorus-doped carbon nitride solid: enhanced electrical conductivity and photocurrent generation*. *Journal of the American Chemical Society* **2010**, *132*-(18), 6294-6295. (b) Hong, J.; Xia, X.; Wang, Y.; Xu, R., *Mesoporous carbon nitride with in situ sulfur doping for enhanced photocatalytic hydrogen evolution from water under visible light*. *Journal of Materials Chemistry* **2012**, *22*-(30), 15006-15012. (c) Wang, Y.; Di, Y.; Antonietti, M.; Li, H.; Chen, X.; Wang, X., *Excellent visible light photocatalysis of fluorinated polymeric carbon nitride solids*. *Chemistry of Materials* **2010**, *22*-(18), 5119-5121. (d) Ran, J.; Ma, T. Y.; Gao, G.; Du, X.-W.; Qiao, S. Z., *Porous P-doped graphitic carbon nitride nanosheets for synergistically enhanced visible light photocatalytic H₂ production*. *Energy & Environmental Science* **2015**, *8*-(12), 3708-3717. (e) Lin, J.; Pan, Z.; Wang, X., *Photochemical reduction of CO₂ by graphitic carbon nitride polymers*. *ACS Sustainable Chemistry & Engineering* **2013**, *2*-(3), 353-358. (f) Wang, Y.; Li, H.; Yao, J.; Wang, X.; Antonietti, M., *Synthesis of boron-doped polymeric carbon nitride solids and their use as metal-free catalysts for aliphatic C-H bond oxidation*. *Chemical Science* **2011**, *2*-(3), 446-450.
12. (a) Yang, S.; Gong, Y.; Zhang, J.; Zhan, L.; Ma, L.; Fang, Z.; Vajtai, R.; Wang, X.; Ajayan, P. M., *Exfoliated graphitic carbon nitride nanosheets as efficient catalysts for hydrogen evolution under visible light*. *Advanced Materials* **2013**, *25*-(17), 2452-2456. (b) Kumar, A.; Kumar, P.; Joshi, C.; Ponnada, S.; Pathak, A. K.; Ali, A.; Sreedhar, B.; Jain, S. L., *A [Fe(bpy)₃]³⁺ grafted graphitic carbon nitride hybrid for visible light assisted oxidative coupling of benzylamines under mild reaction conditions*. *Green Chemistry* **2016**, *18*-(8), 2514-2521. (c) Kumar, A.; Kumar, P.; Pathak, A. K.; Chokkapu, A. N.; Jain, S. L., *Carbon Nitride Grafted Cobalt Complex (Co@npg-C₃N₄) for Visible Light-Assisted Esterification of Aldehydes*. *ChemistrySelect* **2017**, *2*-(12), 3437-3443.
13. (a) Mane, G. P.; Talapaneni, S. N.; Lakhi, K. S.; Ilbeygi, H.; Ravon, U.; Al-Bahily, K.; Mori, T.; Park, D. H.; Vinu, A., *Highly Ordered Nitrogen-Rich Mesoporous Carbon Nitrides and Their Superior Performance for Sensing and Photocatalytic Hydrogen Generation*. *Angew. and Chem. International Edition* **2017**, *56*-(29), 8481-8485.
14. (a) Mane, G. P.; Dhawale, D. S.; Anand, C.; Ariga, K.; Ji, Q.; Wahab, M. A.; Mori, T.; Vinu, A., *Selective sensing performance of mesoporous carbon nitride with a highly ordered porous structure prepared from 3-amino-1,2,4-triazine*. *Journal of Materials Chemistry A* **2013**, *1*-(8), 2913-2920. (b) Talapaneni, S. N.; Mane, G. P.; Park, D.-H.; Lakhi, K. S.; Ramadass, K.; Joseph, S.; Skinner, W. M.; Ravon, U.; Al-Bahily, K.; Vinu, A., *Diaminotetrazine-based mesoporous C₃N₆ with a well-ordered 3D-cubic structure and its excellent photocatalytic performance for hydrogen evolution*. *Journal of Materials Chemistry A* **2017**, *5*-(34), 18183-

- 18192; (c) Talapaneni, S. N.; Mane, G. P.; Mano, A.; Anand, C.; Dhawale, D. S.; Mori, T.; Vinu, A., ~~Synthesis of Nitrogen-Rich Mesoporous Carbon Nitride with Tunable Pores, Band Gaps and Nitrogen Content from a Single Aminoguanidine Precursor~~. *ChemSusChem* **2012**, *5* (4), 700-708; (d) Lakhi, K. S.; Park, D.-H.; Al-Bahily, K.; Cha, W.; Viswanathan, B.; Choy, J.-H.; Vinu, A., ~~Mesoporous carbon nitrides: synthesis, functionalization, and applications~~. *Chem. Soc. Rev.* **2017**, *46* (1), 72-101.
15. —Kim, I. Y.; Kim, S.; Jin, X.; Premkumar, S.; Chandra, G.; Lee, N.-S.; Mane, G. P.; Hwang, S.-J.; Umapathy, S.; Vinu, A., ~~Ordered Mesoporous C₃N₄ with a Combined Triazole and Triazine Framework and Its Graphene Hybrids~~. *Angew. Chem.* **2018**, *130*, 17381-17386.
16. —Fang, J.; Fan, H.; Li, M.; Long, C., ~~Nitrogen self-doped graphitic carbon nitride as efficient visible light photocatalyst for hydrogen evolution~~. *Journal of Materials Chemistry A* **2015**, *3* (26), 13819-13826.
17. —Zhang, P.; Li, X.; Shao, C.; Liu, Y., ~~Hydrothermal synthesis of carbon-rich graphitic carbon nitride nanosheets for photoredox catalysis~~. *Journal of Materials Chemistry A* **2015**, *3* (7), 3281-3284.
18. —(a) Jürgens, B.; Irran, E.; Senker, J.; Kroll, P.; Müller, H.; Schnick, W., ~~Melem (2,5,8-triamino-1,3,5-triazine), an important intermediate during condensation of melamine rings to graphitic carbon nitride: Synthesis, structure determination by X-ray powder diffractometry, solid-state NMR, and theoretical studies~~. *Journal of the American Chemical Society* **2003**, *125* (34), 10288-10300; (b) Chu, S.; Wang, C.; Feng, J.; Wang, Y.; Zou, Z., ~~Melem: A metal-free unit for photocatalytic hydrogen evolution~~. *International Journal of Hydrogen Energy* **2014**, *39* (25), 13519-13526; (c) Saplinova, T.; Lehnert, C.; Böhme, U.; Wagler, J.; Kroke, E., ~~Melem and melamine-derived iminophosphoranes~~. *New Journal of Chemistry* **2010**, *34* (9), 1893-1908; (d) Chu, S.; Wang, Y.; Guo, Y.; Feng, J.; Wang, C.; Luo, W.; Fan, X.; Zou, Z., ~~Band-structure engineering of carbon nitride: in search of a polymer photocatalyst with high photooxidation property~~. *ACS Catalysis* **2013**, *3* (5), 912-919.
19. —Shiraishi, Y.; Kanazawa, S.; Kofuji, Y.; Sakamoto, H.; Ichikawa, S.; Tanaka, S.; Hirai, T., ~~Sunlight-Driven Hydrogen Peroxide Production from Water and Molecular Oxygen by Metal-Free Photocatalysts~~. *Angew. Chem. International Edition* **2014**, *53* (49), 13454-13459.
20. —Che, W.; Cheng, W.; Yao, T.; Tang, F.; Liu, W.; Su, H.; Huang, Y.; Liu, Q.; Liu, J.; Hu, F., ~~Fast Photoelectron Transfer in (Cring)-C₃N₄ Plane Heterostructural Nanosheets for Overall Water Splitting~~. *Journal of the American Chemical Society* **2017**, *139* (8), 3021-3026.
21. —(a) Miller, D. R.; Swenson, D. C.; Gillan, E. G., ~~Synthesis and structure of 2,5,8-triazido-s-heptazine: An energetic and luminescent precursor to nitrogen-rich carbon nitrides~~. *Journal of the American Chemical Society* **2004**, *126* (17), 5372-5373; (b) Miller, D. R.; Holst, J. R.; Gillan, E. G., ~~Nitrogen-rich carbon nitride network materials via the thermal decomposition of 2,5,8-triazido-s-heptazine~~. *Inorganic Chemistry* **2007**, *46* (7), 2767-2774.
22. —Gillan, E. G., ~~Synthesis of nitrogen-rich carbon nitride networks from an energetic molecular azide precursor~~. *Chemistry of Materials* **2000**, *12* (12), 3906-3912.
23. —(a) Saplinova, T.; Bakumov, V.; Gmeiner, T.; Wagler, J.; Schwarz, M.; Kroke, E., ~~2,5,8-Trihydrazino-s-heptazine: A Precursor for Heptazine-based Iminophosphoranes~~. *Zeitschrift für Anorganische und Allgemeine Chemie* **2009**, *635* (15), 2480-2487; (b) Sattler, A.; Schönberger, S.; Schnick, W., ~~Melemium Methylsulfonates HC₆N₇(NH₂)₃H₂C₆N₇(NH₂)₃(SO₃Me)₃·3H₂O and H₂C₆N₇(NH₂)₃(SO₃Me)₂·2H₂O~~. *Zeitschrift für Anorganische und Allgemeine Chemie* **2010**, *636* (3-4), 476-482.

Formatted: Font: Not Bold, Italic

24. —Makowski, S. J.; Köstler, P.; Schnick, W., ~~Formation of a Hydrogen Bonded Heptazine Framework by Self Assembly of Melem into a Hexagonal Channel Structure.~~ *Chemistry-A European Journal* **2012**, *18* (11), 3248-3257.
25. —(a) Kumar, A.; Kumar, P.; Borkar, R.; Bansiwala, A.; Labhsetwar, N.; Jain, S. L., ~~Metal-organic hybrid: Photoreduction of CO₂ using graphitic carbon nitride supported heteroleptic iridium complex under visible light irradiation.~~ *Carbon* **2017**, *123*, 371-379; (b) Yu, H.; Shi, R.; Zhao, Y.; Bian, T.; Zhao, Y.; Zhou, C.; Waterhouse, G. I.; Wu, L. Z.; Tung, C. H.; Zhang, T., ~~Alkali-Assisted Synthesis of Nitrogen Deficient Graphitic Carbon Nitride with Tunable Band Structures for Efficient Visible-Light-Driven Hydrogen Evolution.~~ *Advanced Materials* **2017**, *29* (16), 1605148.
26. —(a) Xia, P.; Zhu, B.; Yu, J.; Cao, S.; Jaroniec, M., ~~Ultra-thin nanosheet assemblies of graphitic carbon nitride for enhanced photocatalytic CO₂ reduction.~~ *Journal of Materials Chemistry A* **2017**, *5* (7), 3230-3238; (b) Mao, J.; Peng, T.; Zhang, X.; Li, K.; Ye, L.; Zan, L., ~~Effect of graphitic carbon nitride microstructures on the activity and selectivity of photocatalytic CO₂ reduction under visible light.~~ *Catalysis Science & Technology* **2013**, *3* (5), 1253-1260.
27. —Axen, N.; Botton, G.; Somekh, R.; Hutchings, I., ~~Effect of deposition conditions on the chemical bonding in sputtered carbon nitride films.~~ *Diamond and Related Materials* **1996**, *5* (2), 163-168.
28. —Hu, J.; Yang, P.; Lieber, C. M., ~~Nitrogen-driven sp³ to sp² transformation in carbon nitride materials.~~ *Phys. Rev. B* **1998**, *57* (6), R3185.
29. —Li, X.; Zhang, J.; Shen, L.; Ma, Y.; Lei, W.; Cui, Q.; Zou, G., ~~Preparation and characterization of graphitic carbon nitride through pyrolysis of melamine.~~ *Applied Physics A* **2009**, *94* (2), 387-392.
30. —Seyfarth, L.; Senker, J., ~~An NMR crystallographic approach for the determination of the hydrogen substructure of nitrogen-bonded protons.~~ *Physical Chemistry Chemical Physics* **2009**, *11* (18), 3522-3531.
31. —(a) Sehnert, J.; Baerwinkel, K.; Senker, J., ~~Ab initio calculation of solid-state NMR spectra for different triazine and heptazine based structure proposals of g-C₃N₄.~~ *The Journal of Physical Chemistry B* **2007**, *111* (36), 10671-10680; (b) Hu, Y.; Shim, Y.; Oh, J.; Park, S.; Park, S.; Ishii, Y., ~~Synthesis of ¹³C, ¹⁵N Labeled Graphitic Carbon Nitrides and NMR Based Evidence of Hydrogen Bonding Assisted Two-Dimensional Assembly.~~ *Chemistry of Materials* **2017**, *29* (12), 5080-5089.
32. —Cui, Y.; Ding, Z.; Fu, X.; Wang, X., ~~Construction of conjugated carbon nitride nanoarchitectures in solution at low temperatures for photoredox catalysis.~~ *Angewandte Chemie International Edition* **2012**, *51* (47), 11814-11818.
33. —Sattler, A.; Pagano, S.; Zeuner, M.; Zurawski, A.; Gunzelmann, D.; Senker, J.; Müller-Buschbaum, K.; Schnick, W., ~~Melamine-melem adduct phases: investigating the thermal condensation of melamine.~~ *Chemistry-A European Journal* **2009**, *15* (47), 13161-13170.
34. —(a) Hsu, C.-Y.; Chang, K.-S., ~~Fabrication and Photocatalytic Application of Aromatic Ring Functionalized Melem Oligomers.~~ *The Journal of Physical Chemistry C* **2018**, *122* (6), 3506-3512; (b) Rovnyak, D.; Baldus, M.; Itin, B. A.; Bennati, M.; Stevens, A.; Griffin, R. G., ~~Characterization of a Carbon-Nitrogen Network Solid with NMR and High-Field EPR.~~ *The Journal of Physical Chemistry B* **2000**, *104* (42), 9817-9822.
35. —Lotsch, B. V.; Schnick, W., ~~New light on an old story: formation of melam during thermal condensation of melamine.~~ *Chemistry-A European Journal* **2007**, *13* (17), 4956-4968.

36. — Guo, Q.; Zhang, Y.; Qiu, J.; Dong, G., ~~Engineering the electronic structure and optical properties of gC₃N₄ by non-metal ion doping.~~ *J.ournal of Mater.ials Chem.istry C* **2016**, *4*-(28), 6839-6847.
37. — (a) Gulaczyk, I.; Kęrglewski, M.; Valentin, A., ~~The N-N stretching band of hydrazine.~~ *J.ournal of Mol.ecular Spectrosc.opy* **2003**, *220*-(1), 132-136; (b) Dirtu, D.; Odochian, L.; Pui, A.; Humelnicu, I., ~~Thermal decomposition of ammonia. N₂H₄ an intermediate reaction product.~~ *Open Chem.istry* **2006**, *4*-(4), 666-673.
38. — (a) Niu, P.; Zhang, L.; Liu, G.; Cheng, H. M., ~~Graphene-like carbon nitride nanosheets for improved photocatalytic activities.~~ *Adv.anced Funct.ional Mater.ials* **2012**, *22*-(22), 4763-4770; (b) Xu, J.; Zhang, L.; Shi, R.; Zhu, Y., ~~Chemical exfoliation of graphitic carbon nitride for efficient heterogeneous photocatalysis.~~ *J.ournal of Mater.ials Chem.istry A* **2013**, *1*-(46), 14766-14772.
39. — (a) Zheng, H.; Chen, W.; Gao, H.; Wang, Y.; Guo, H.; Guo, S.; Tang, Z.; Zhang, J., ~~Melem: an efficient metal-free luminescent material.~~ *J.ournal of Mater.ials Chem.istry C* **2017**, *5*-(41), 10746-10753; (b) Lau, V. W.-h.; Mesch, M. B.; Duppel, V.; Blum, V.; Senker, J. r.; Lotsch, B. V., ~~Low molecular weight carbon nitrides for solar hydrogen evolution.~~ *J.ournal of the Am.erician Chem.ical Soc.iety* **2015**, *137*-(3), 1064-1072.
40. — (a) Wang, X.; Maeda, K.; Thomas, A.; Takanabe, K.; Xin, G.; Carlsson, J. M.; Domen, K.; Antonietti, M., ~~A metal-free polymeric photocatalyst for hydrogen production from water under visible light.~~ *Nat.ure Mmater.ials* **2009**, *8*-(1), 76; (b) Bojdys, M. J.; Müller, J. O.; Antonietti, M.; Thomas, A., ~~Ionothermal synthesis of crystalline, condensed, graphitic carbon nitride.~~ *Chem.istry A Eur.opean J.ournal* **2008**, *14*-(27), 8177-8182.
41. — Kroke, E.; Schwarz, M.; Horath-Bordon, E.; Kroll, P.; Noll, B.; Norman, A. D., ~~Tri-s-triazine derivatives. Part I. From trichloro tri-s-triazine to graphitic C₃N₄ structures.~~ *New J.ournal of Chem.istry* **2002**, *26*-(5), 508-512.
42. — Tonda, S.; Kumar, S.; Kandula, S.; Shanker, V., ~~Fe-doped and-mediated graphitic carbon nitride nanosheets for enhanced photocatalytic performance under natural sunlight.~~ *J.ournal of Mater.ials Chem.istry A* **2014**, *2*-(19), 6772-6780.
43. — Jiang, J.; Ou-yang, L.; Zhu, L.; Zheng, A.; Zou, J.; Yi, X.; Tang, H., ~~Dependence of electronic structure of gC₃N₄ on the layer number of its nanosheets: a study by Raman spectroscopy coupled with first principles calculations.~~ *Carbon* **2014**, *80*, 213-221.
44. — Cui, Y.; Zhang, J.; Zhang, G.; Huang, J.; Liu, P.; Antonietti, M.; Wang, X., ~~Synthesis of bulk and nanoporous carbon nitride polymers from ammonium thiocyanate for photocatalytic hydrogen evolution.~~ *J.ournal of Mater.ials Chem.istry* **2011**, *21*-(34), 13032-13039.
45. — Zhang, J.; Zhang, M.; Lin, S.; Fu, X.; Wang, X., ~~Molecular doping of carbon nitride photocatalysts with tunable bandgap and enhanced activity.~~ *J.ournal of Catal.ysis* **2014**, *310*, 24-30.
46. — (a) Sharma, P.; Sasson, Y., ~~A photoactive catalyst Ru-g-C₃N₄ for hydrogen transfer reaction of aldehydes and ketones.~~ *Green Chem.istry* **2017**, *19*-(3), 844-852; (b) Yuan, B.; Chu, Z.; Li, G.; Jiang, Z.; Hu, T.; Wang, Q.; Wang, C., ~~Water-soluble ribbon-like graphitic carbon nitride (g-C₃N₄): green synthesis, self assembly and unique optical properties.~~ *J.ournal of Mater.ials Chem.istry C* **2014**, *2*-(39), 8212-8215.
47. — Zhang, G.; Zhang, M.; Ye, X.; Qiu, X.; Lin, S.; Wang, X., ~~Iodine-modified carbon nitride semiconductors as visible light photocatalysts for hydrogen evolution.~~ *Adv.anced Mater.ials* **2014**, *26*-(5), 805-809.

48. —(a) Shalom, M.; Inal, S.; Fettkenhauer, C.; Neher, D.; Antonietti, M., ~~Improving carbon nitride photocatalysis by supramolecular preorganization of monomers.~~ *Journal of the American Chemical Society* **2013**, *135* (19), 7118-7121.; (b) Shalom, M.; Guttentag, M.; Fettkenhauer, C.; Inal, S.; Neher, D.; Llobet, A.; Antonietti, M., ~~In situ formation of heterojunctions in modified graphitic carbon nitride: Synthesis and noble metal free photocatalysis.~~ *Chemistry of Materials* **2014**, *26* (19), 5812-5818.
49. —(a) Kang, Y.; Yang, Y.; Yin, L. C.; Kang, X.; Wang, L.; Liu, G.; Cheng, H. M., ~~Selective breaking of hydrogen bonds of layered carbon nitride for visible light photocatalysis.~~ *Advanced Materials* **2016**, *28* (30), 6471-6477.; (b) Yang, P.; Ou, H.; Fang, Y.; Wang, X., ~~A facile steam reforming strategy to delaminate layered carbon nitride semiconductors for photoredox catalysis.~~ *Angewandte Chemie International Edition* **2017**, *56* (14), 3992-3996.
50. —Alibert, F.; Lejeune, M.; Durand Drouhin, O.; Zellama, K.; Benlahsen, M., ~~Influence of disorder on localization and density of states in amorphous carbon nitride thin films systems rich in π bonded carbon atoms.~~ *Journal of Applied Physics* **2010**, *108* (5), 053504.
51. —(a) Zhang, Y.; Pan, Q.; Chai, G.; Liang, M.; Dong, G.; Zhang, Q.; Qiu, J., ~~Synthesis and luminescence mechanism of multicolor emitting g-C₃N₄ nanopowders by low temperature thermal condensation of melamine.~~ *Scientific Reports* **2013**, *3*, 1943.; (b) Sun, C.; Tay, B.; Lau, S.; Sun, X.; Zeng, X.; Li, S.; Bai, H.; Liu, H.; Liu, Z.; Jiang, E., ~~Bond contraction and lone pair interaction at nitride surfaces.~~ *Journal of Applied Physics* **2001**, *90* (5), 2615-2617.
52. —Niu, P.; Liu, G.; Cheng, H. M., ~~Nitrogen vacancy promoted photocatalytic activity of graphitic carbon nitride.~~ *The Journal of Physical Chemistry C* **2012**, *116* (20), 11013-11018.
53. —(a) Chen, L. C.; Teng, C. Y.; Lin, C. Y.; Chang, H. Y.; Chen, S. J.; Teng, H., ~~Architecting nitrogen functionalities on graphene oxide photocatalysts for boosting hydrogen production in water decomposition process.~~ *Advanced Energy Materials* **2016**, *6* (22), 1600719.; (b) Yeh, T. F.; Teng, C. Y.; Chen, S. J.; Teng, H., ~~Nitrogen-Doped Graphene Oxide Quantum Dots as Photocatalysts for Overall Water-Splitting under Visible Light Illumination.~~ *Advanced Materials* **2014**, *26* (20), 3297-3303.; (c) Yeh, T.-F.; Chen, S.-J.; Yeh, C.-S.; Teng, H., ~~Tuning the electronic structure of graphite oxide through ammonia treatment for photocatalytic generation of H₂ and O₂ from water splitting.~~ *The Journal of Physical Chemistry C* **2013**, *117* (13), 6516-6524.; (d) Shi, R.; Li, Z.; Yu, H.; Shang, L.; Zhou, C.; Waterhouse, G. I.; Wu, L. Z.; Zhang, T., ~~Effect of nitrogen doping level on the performance of N-doped carbon quantum dot/TiO₂ composites for photocatalytic hydrogen evolution.~~ *ChemSusChem* **2017**, *10* (22), 4650-4656.; (e) Chen, L. C.; Teng, C. Y.; Lin, C. Y.; Chang, H. Y.; Chen, S. J.; Teng, H., ~~Architecting nitrogen functionalities on graphene oxide photocatalysts for boosting hydrogen production in water decomposition process.~~ *Advanced Energy Materials* **2016**, *6* (22), 1600719.; (f) Run, S.; Zi, L.; Huijun, Y.; Lu, S.; Chao, Z.; N., W. G. I.; Li-Zhu, W.; Tierui, Z., ~~Effect of Nitrogen Doping Level on the Performance of N-Doped Carbon Quantum Dot/TiO₂ Composites for Photocatalytic Hydrogen Evolution.~~ *ChemSusChem* **2017**, *10* (22), 4650-4656.
54. —Liang, Q.; Li, Z.; Huang, Z. H.; Kang, F.; Yang, Q. H., ~~Holey graphitic carbon nitride nanosheets with carbon vacancies for highly improved photocatalytic hydrogen production.~~ *Advanced Functional Materials* **2015**, *25* (44), 6885-6892.
55. —(a) Sun, J.; Zhang, J.; Zhang, M.; Antonietti, M.; Fu, X.; Wang, X., ~~Bioinspired hollow semiconductor nanospheres as photosynthetic nanoparticles.~~ *Nature Communications* **2012**, *3*, 1139.; (b) Liu, Q.; Chen, T.; Guo, Y.; Zhang, Z.; Fang, X., ~~Ultrathin g-C₃N₄ nanosheets coupled with carbon nanodots as 2D/0D composites for efficient photocatalytic H₂ evolution.~~ *Applied*

- Catalysis B: Environmental* **2016**, 193, 248-258; (c) Ye, X.; Cui, Y.; Wang, X., ~~Ferrocene-Modified Carbon Nitride for Direct Oxidation of Benzene to Phenol with Visible Light~~. *ChemSusChem* **2014**, 7(3), 738-742.
56. —(a) Chen, Z.; Sun, P.; Fan, B.; Liu, Q.; Zhang, Z.; Fang, X., ~~Textural and electronic structure engineering of carbon nitride via doping with π -deficient aromatic pyridine ring for improving photocatalytic activity~~. *Applied Catalysis B: Environmental* **2015**, 170, 10-16; (b) Zhang, M.; Duan, Y.; Jia, H.; Wang, F.; Wang, L.; Su, Z.; Wang, C., ~~Defective graphitic carbon nitride synthesized by controllable co-polymerization with enhanced visible light photocatalytic hydrogen evolution~~. *Catalysis Science & Technology* **2017**, 7(2), 452-458.
57. —(a) Qin, J.; Wang, S.; Ren, H.; Hou, Y.; Wang, X., ~~Photocatalytic reduction of CO₂ by graphitic carbon nitride polymers derived from urea and barbituric acid~~. *Applied Catalysis B: Environmental* **2015**, 179, 1-8; (b) Luo, L.; Zhang, M.; Wang, P.; Wang, Y.; Wang, F., ~~Nitrogen rich carbon nitride synthesized by copolymerization with enhanced visible light photocatalytic hydrogen evolution~~. *New Journal of Chemistry* **2018**, 42(2), 1087-1091.
58. —Ali, H., ~~Biodegradation of synthetic dyes—a review~~. *Water, Air, & Soil Pollution* **2010**, 213(1-4), 251-273.
59. —Mittal, A.; Mittal, J.; Malviya, A.; Kaur, D.; Gupta, V., ~~Adsorption of hazardous dye crystal violet from wastewater by waste materials~~. *Journal of Colloid and Interface Science* **2010**, 343(2), 463-473.
60. —Yagub, M. T.; Sen, T. K.; Afroze, S.; Ang, H. M., ~~Dye and its removal from aqueous solution by adsorption: a review~~. *Advances in Colloid and Interface Science* **2014**, 209, 172-184.
61. —(a) Fronczak, M.; Krajewska, M.; Demby, K.; Bystrzejewski, M., ~~Extraordinary adsorption of methyl blue onto sodium-doped graphitic carbon nitride~~. *The Journal of Physical Chemistry C* **2017**, 121(29), 15756-15766; (b) Zhu, B.; Xia, P.; Ho, W.; Yu, J., ~~Isoelectric point and adsorption activity of porous g-C₃N₄~~. *Applied Surface Science* **2015**, 344, 188-195.
62. —Langmuir, I., ~~The adsorption of gases on plane surfaces of glass, mica and platinum~~. *Journal of the American Chemical Society* **1918**, 40(9), 1361-1403.
63. —Freundlich, H., ~~Over the adsorption in solution~~. *J. Phys. Chem.* **1906**, 57(385471), 1100-1107.
64. —Han, S.; Liu, K.; Hu, L.; Teng, F.; Yu, P.; Zhu, Y., ~~Superior adsorption and regenerable dye adsorbent based on flower-like molybdenum disulfide nanostructure~~. *Scientific Reports* **2017**, 7, 43599.
65. —Gaya, U. I.; Abdullah, A. H., ~~Heterogeneous photocatalytic degradation of organic contaminants over titanium dioxide: a review of fundamentals, progress and problems~~. *Journal of Photochemistry and Photobiology C: Photochemistry Reviews* **2008**, 9(1), 1-12.
66. —Ahmad, H.; Kamarudin, S.; Minggu, L.; Kassim, M., ~~Hydrogen from photocatalytic water splitting process: A review~~. *Renewable and Sustainable Energy Reviews* **2015**, 43, 599-610.
67. —Pelaez, M.; Nolan, N. T.; Pillai, S. C.; Seery, M. K.; Falaras, P.; Kontos, A. G.; Dunlop, P. S.; Hamilton, J. W.; Byrne, J. A.; O'shea, K., ~~A review on the visible light active titanium dioxide photocatalysts for environmental applications~~. *Applied Catalysis B: Environmental* **2012**, 125, 331-349.
68. —Zhou, X.; Peng, F.; Wang, H.; Yu, H.; Fang, Y., ~~Carbon nitride polymer sensitized TiO₂ nanotube arrays with enhanced visible light photoelectrochemical and photocatalytic performance~~. *Chemical Communications* **2011**, 47(37), 10323-10325.

69. —(a) Zheng, X. J.; Chen, B.; Yang, M. J.; Wu, C. C.; Orlor, B.; Moore, R. B.; Zhu, K.; Priya, S.; ~~The Controlling Mechanism for Potential Loss in CH₃NH₃PbBr₃ Hybrid Solar Cells.~~ *ACS Energy Lett.* **2016**, *1*-(2), 424-430; (b) Askar, A. M.; Bernard, G. M.; Wiltshire, B.; Shankar, K.; Michaelis, V. K.; ~~Multinuclear magnetic resonance tracking of hydro, thermal, and hydrothermal decomposition of CH₃NH₃PbI₃.~~ *The Journal of Physical Chemistry C* **2017**, *121*-(2), 1013-1024.
70. —Zhao, Y.; Nardes, A. M.; Zhu, K.; ~~Mesoporous perovskite solar cells: material composition, charge-carrier dynamics, and device characteristics.~~ *Faraday Discussions* **2014**, *176*-(9), 301-312.
71. —Wu, C. G.; Chiang, C. H.; Chang, S. H.; ~~A perovskite cell with a record-high V_{oc} of 1.61 V based on solvent annealed CH₃NH₃PbBr₃/ICBA active layer.~~ *Nanoscale* **2016**, *8*-(7), 4077-4085.
72. —Li, Z.; Boix, P. P.; Xing, G. C.; Fu, K. W.; Kulkarni, S. A.; Batabyal, S. K.; Xu, W. J.; Cao, A. Y.; Sum, T. C.; Mathews, N.; Wong, L. H.; ~~Carbon nanotubes as an efficient hole collector for high voltage methylammonium lead bromide perovskite solar cells.~~ *Nanoscale* **2016**, *8*-(12), 6352-6360.
73. —Zuo, C. T.; Ding, L. M.; ~~Modified PEDOT Layer Makes a 1.52 V V_{oc} for Perovskite/PCBM Solar Cells.~~ *Adv. Energy Mater.* **2017**, *7*-(2), 1601193.
74. —Liang, Y. Q.; Wang, Y. J.; Mu, C.; Wang, S.; Wang, X. N.; Xu, D. S.; Sun, L. C.; ~~Achieving High Open Circuit Voltages up to 1.57 V in Hole Transport Material Free MAPbBr₃ Solar Cells with Carbon Electrodes.~~ *Adv. Energy Mater.* **2018**, *8*-(4), 1701159.
75. —Sheng, R.; Ho-Baillie, A.; Huang, S. J.; Chen, S.; Wen, X. M.; Hao, X. J.; Green, M. A.; ~~Methylammonium Lead Bromide Perovskite Based Solar Cells by Vapor Assisted Deposition.~~ *J. Phys. Chem. C* **2015**, *119*-(7), 3545-3549.
76. —Ryu, S.; Noh, J. H.; Jeon, N. J.; Kim, Y. C.; Yang, S.; Seo, J. W.; Seok, S. I.; ~~Voltage output of efficient perovskite solar cells with high open-circuit voltage and fill factor.~~ *Energy & Environmental Science* **2014**, *7*-(8), 2614-2618.
77. —(a) Chen, X.; Liu, Q.; Wu, Q.; Du, P.; Zhu, J.; Dai, S.; Yang, S.; ~~Incorporating Graphitic Carbon Nitride (g-C₃N₄) Quantum Dots into Bulk Heterojunction Polymer Solar Cells Leads to Efficiency Enhancement.~~ *Advanced Functional Materials* **2016**, *26*-(11), 1719-1728; (b) He, M.; Chen, Y.; Liu, H.; Wang, J.; Fang, X.; Liang, Z.; ~~Chemical decoration of CH₃NH₃PbI₃ perovskites with graphene oxides for photodetector applications.~~ *Chemical Communications* **2015**, *51*-(47), 9659-9661; (c) Zhu, Z.; Ma, J.; Wang, Z.; Mu, C.; Fan, Z.; Du, L.; Bai, Y.; Fan, L.; Yan, H.; Phillips, D. L.; ~~Efficiency enhancement of perovskite solar cells through fast electron extraction: the role of graphene quantum dots.~~ *Journal of the American Chemical Society* **2014**, *136*-(10), 3760-3763; (d) Hadadian, M.; Correa-Baena, J. P.; Goharshadi, E. K.; Ummadisingu, A.; Seo, J. Y.; Luo, J.; Gholipour, S.; Zakeeruddin, S. M.; Saliba, M.; Abate, A.; ~~Enhancing Efficiency of Perovskite Solar Cells via N-doped Graphene: Crystal Modification and Surface Passivation.~~ *Advanced Materials* **2016**, *28*-(39), 8681-8686; (e) Jiang, L. L.; Wang, Z. K.; Li, M.; Zhang, C. C.; Ye, Q. Q.; Hu, K. H.; Lu, D. Z.; Fang, P. F.; Liao, L. S.; ~~Passivated Perovskite Crystallization via g-C₃N₄ for High-Performance Solar Cells.~~ *Advanced Functional Materials* **2018**, *28*-(7), 1705875.
78. —(a) Kirchartz, T.; Gong, W.; Hawks, S. A.; Agostinelli, T.; MacKenzie, R. C. I.; Yang, Y.; Nelson, J.; ~~Sensitivity of the Mott-Schottky Analysis in Organic Solar Cells.~~ *The Journal of Physical Chemistry C* **2012**, *116*-(14), 7672-7680; (b) Guo, X.; Tan, Q.; Liu, S.; Qin, D.; Mo, Y.; Hou, L.; Liu, A.; Wu, H.; Ma, Y.; ~~High-efficiency solution-processed CdTe nanocrystal solar~~

Formatted: Font: (Default) Times New Roman, 12 pt

cells incorporating a novel crosslinkable conjugated polymer as the hole transport layer. *Nano Energy* **2018**, *46*, 150-157. (c) Liu, Z.; Zhu, A.; Cai, F.; Tao, L.; Zhou, Y.; Zhao, Z.; Chen, Q.; Cheng, Y.-B.; Zhou, H., **Nickel oxide nanoparticles for efficient hole transport in p-i-n and n-i-p perovskite solar cells.** *Journal of Materials Chemistry A* **2017**, *5* (14), 6597-6605. (d) Liu, Z.; Chang, J.; Lin, Z.; Zhou, L.; Yang, Z.; Chen, D.; Zhang, C.; Liu, S.; Hao, Y., **High-Performance Planar Perovskite Solar Cells Using Low-Temperature, Solution-Combustion-Based Nickel Oxide Hole-Transporting Layer with Efficiency Exceeding 20%.** *Adv. Energy Mater.* **2018**, *8* (19), 1703432. (e) Jahandar, M.; Heo, J. H.; Song, C. E.; Kong, K.-J.; Shin, W. S.; Lee, J.-C.; Im, S. H.; Moon, S.-J., **Highly efficient metal halide-substituted $\text{CH}_3\text{NH}_3\text{I}(\text{PbI}_2)_{1-x}(\text{CuBr}_2)_x$ planar perovskite solar cells.** *Nano Energy* **2016**, *27*, 330-339. (f) He, Q.; Yao, K.; Wang, X.; Xia, X.; Leng, S.; Li, F., **Room-Temperature and Solution-Processable Cu-Doped Nickel Oxide Nanoparticles for Efficient Hole Transport Layers of Flexible Large-Area Perovskite Solar Cells.** *ACS Applied Materials & Interfaces* **2017**, *9* (48), 41887-41897. (g) Niu, G.; Wang, S.; Li, J.; Li, W.; Wang, L., **Oxygen doping in nickel oxide for highly efficient planar perovskite solar cells.** *Journal of Materials Chemistry A* **2018**, *6* (11), 4721-4728.

79. (a) Lin, W.; Cao, E.; Zhang, L.; Xu, X.; Song, Y.; Liang, W.; Sun, M., **Electrically enhanced hot hole driven oxidation catalysis at the interface of a plasmon exciton hybrid.** *Nanoscale* **2018**, *10* (12), 5482-5488. (b) Kang, L.; Chu, J.; Zhao, H.; Xu, P.; Sun, M., **Recent progress in the applications of graphene in surface-enhanced Raman scattering and plasmon-induced catalytic reactions.** *Journal of Materials Chemistry C* **2015**, *3* (35), 9024-9037. (c) Ding, Q.; Shi, Y.; Chen, M.; Li, H.; Yang, X.; Qu, Y.; Liang, W.; Sun, M., **Ultrafast dynamics of plasmon exciton interaction of Ag nanowire-graphene hybrids for surface catalytic reactions.** *Scientific Reports* **2016**, *6*, 32724. (d) Wu, H. Y.; Lai, Y. H.; Hsieh, M. S.; Lin, S. D.; Li, Y. C.; Lin, T. W., **Highly Intensified Surface-Enhanced Raman Scattering through the Formation of p, p'-Dimercaptoazobenzene on Ag Nanoparticles/Graphene Oxide Nanocomposites.** *Adv. Mater. Interfaces* **2014**, *1* (8), 1400119.

80. (a) Liang, X.; You, T.; Liu, D.; Lang, X.; Tan, E.; Shi, J.; Yin, P.; Guo, L., **Direct observation of enhanced plasmon-driven catalytic reaction activity of Au nanoparticles supported on reduced graphene oxides by SERS.** *Physical Chemistry Chemical Physics* **2015**, *17* (15), 10176-10181. (b) Zhao, J.; Sun, M.; Liu, Z.; Quan, B.; Gu, C.; Li, J., **Three dimensional hybrids of vertical graphene nanosheet sandwiched by Ag nanoparticles for enhanced surface selectively catalytic reactions.** *Scientific Reports* **2015**, *5*, 16019.

81. Siekkinen, A. R.; McLellan, J. M.; Chen, J.; Xia, Y., **Rapid synthesis of small silver nanocubes by mediating polyol reduction with a trace amount of sodium sulfide or sodium hydrosulfide.** *Chemical Physics Letters* **2006**, *432* (4-6), 491-496.

82. Dong, B.; Fang, Y.; Xia, L.; Xu, H.; Sun, M., **Is 4-nitrobenzenethiol converted to p, p'-dimercaptoazobenzene or 4-aminothiophenol by surface photochemistry reaction?** *Journal of Raman Spectroscopy* **2011**, *42* (6), 1205-1206.

83. (a) Canpean, V.; Iosin, M.; Astilean, S., **Disentangling SERS signals from two molecular species: A new evidence for the production of p, p'-dimercaptoazobenzene by catalytic coupling reaction of p-aminothiophenol on metallic nanostructures.** *Chemical Physics Letters* **2010**, *500* (4-6), 277-282. (b) Fang, Y.; Li, Y.; Xu, H.; Sun, M., **Ascertaining p, p'-dimercaptoazobenzene produced from p-aminothiophenol by selective catalytic coupling reaction on silver nanoparticles.** *Langmuir* **2010**, *26* (11), 7737-7746.

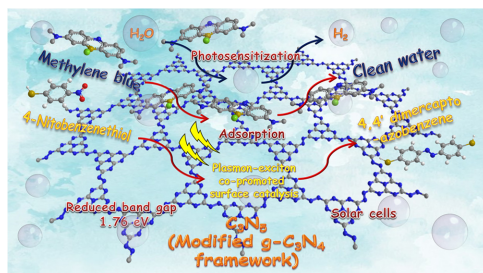
1
2
3
4
5
6
7
8
9
10
11
12
13
14
15
16
17
18
19
20
21
22
23
24
25
26
27
28
29
30
31
32
33
34
35
36
37
38
39
40
41
42
43
44
45
46
47
48
49
50
51
52
53
54
55
56
57
58
59
60

84. —(a) Kang, Y.; Yang, Y.; Yin, L. C.; Kang, X.; Liu, G.; Cheng, H. M., ~~An Amorphous Carbon Nitride Photocatalyst with Greatly Extended Visible Light Responsive Range for Photocatalytic Hydrogen Generation.~~ *Advanced Materials* **2015**, 27 (31), 4572-4577. (b) Niu, P.; Qiao, M.; Li, Y.; Huang, L.; Zhai, T., ~~Distinctive defects engineering in graphitic carbon nitride for greatly extended visible light photocatalytic hydrogen evolution.~~ *Nano Energy* **2018**, 44, 73-81.

85. —(a) Dang, Q.-Q.; Wang, X.-M.; Zhan, Y.-F.; Zhang, X.-M., ~~An azo-linked porous triptycene network as an absorbent for CO₂ and iodine uptake.~~ *Polym. Chem.* **2016**, 7 (3), 643-647. (b) Patel, H. A.; Je, S. H.; Park, J.; Chen, D. P.; Jung, Y.; Yavuz, C. T.; Coskun, A., ~~Unprecedented high-temperature CO₂ selectivity in N₂-phobic nanoporous covalent organic polymers.~~ *Nature Communications* **2013**, 4, 1357. (c) Patel, H. A.; Je, S. H.; Park, J.; Jung, Y.; Coskun, A.; Yavuz, C. T., ~~Directing the structural features of N₂-phobic nanoporous covalent organic polymers for CO₂ capture and separation.~~ *Chemistry - A European Journal* **2014**, 20 (3), 772-780.

86. —(a) Clark, M., *Handbook of textile and industrial dyeing: principles, processes and types of dyes*. Elsevier: 2011. (b) Zollinger, H., *Color chemistry: syntheses, properties, and applications of organic dyes and pigments*. John Wiley & Sons: 2003. (c) Robin, M. B.; Simpson, W. T., ~~Assignment of electronic transitions in azo dye prototypes.~~ *The Journal of Chemical Physics* **1962**, 36 (3), 580-588.

Graphical abstract



SUPPORTING INFORMATION

for

C₃N₅: A Low Bandgap Semiconductor Containing an Azo-linked Carbon Nitride Framework for Photocatalytic, Photovoltaic and Adsorbent Applications

Pawan Kumar,^{1*} Ehsan Vahidzadeh,¹ Ujwal K. Thakur,¹ Piyush Kar,¹ Kazi M. Alam,¹ Ankur Goswami,¹ Najia Mahdi,¹ Kai Cui,² Guy M. Bernard,³ Vladimir K. Michaelis³ and Karthik Shankar^{1*}

¹Department of Electrical and Computer Engineering, University of Alberta, 9211 - 116 St, Edmonton, Alberta, Canada T6G 1H9

²Nanotechnology Research Centre, National Research Council of Canada, Edmonton, Canada T6G 2M9

³Department of Chemistry, University of Alberta, Edmonton, Alberta, Canada, T6G 2G2

*Email: Pawan Kumar (pawan@ualberta.ca), Karthik Shankar (kshankar@ualberta.ca)

Contents

Formatted: Highlight

1.0 Experimental details

1.1 Reagent and materials	Page S4
1.2 Physicochemical characterization	Page S5
1.3 Electrochemical characterization	Page S9

2.0 Synthesis procedures

2.1 Synthesis of Melem (2,5,8-triamino-s-triazine)	Page S10
2.2 Synthesis of 2,5,8-trihydrazino-s-heptazine or melem hydrazine (MH)	Page S10

2.3 Synthesis of C_3N_5 polymer	Page S11
2.4 Synthesis of g- C_3N_4	Page S11
3.0 Experimental for dye adsorption	Page S12
4.0 Photo-electrochemical measurements	Page S12
5.0 Fabrication of solar cell	Page S13
6.0 Measurement of plasmon excitons co-induced surface catalytic transformation of 4NBT to DMAB	Page S15
7.0 Calculation of efficiencies	Page S15
8.0 Figures	
Figure S1. Chemical structures of melem, melem hydrazine, hydrogen bonded melem hydrazine.	Page S17
Figure S2. (a) XPS elemental survey scan of C_3N_5 , and HR-XPS spectra of C_3N_5 in (b) Na1s, (c) Cl2p, and (d) O1s regions.	Page S18
Figure S3+S4. EELS spectra of g- C_3N_4 and C_3N_5 showing σ^* and π^* peaks in C K-edge and N K-edge energy loss	Page S19+27
Figure S4. Solid state CP MAS 1H NMR spectra of (a) melem hydrazine, MH and (b) C_3N_5	Page S20
Figure S5. Raman spectra of (a) melem, (b) melem hydrazine, MH, (c) g- C_3N_4 and (d) C_3N_5	Page S21
Figure S6. (a) Tauc plot of g- C_3N_4 (blue) and C_3N_5 (red) for band gap determination and (b) Mott Schottky plot of g- C_3N_4 (blue) and C_3N_5 (red) in 0.5 M Na_2SO_4 at 1K frequency	Page S22
Figure S7+S9. PL spectra of (a) g- C_3N_4 , (b) C_3N_5 and (c) C_3N_5 /MB composite at different sample spots obtained by using two-photon laser in femtosecond fluorescence life time instrument and two-photon fluorescence images of (d) g- C_3N_4 , (e) C_3N_5 , and (f) C_3N_5 /MB composite	Page S23+34

Figure S810. Zeta potential distribution of C_3N_5 for calculating surface charge. **Page S245**

Figure S119. Comparison of (a) FTIR spectra, (b) Raman spectra, (c) PL spectra using 360 nm excitation wavelength, and (d) CP-MAS ssNMR of C_3N_5 and C_3N_5 /MB composite. **Page S256**

Figure S103. (a) XPS survey scan of C_3N_5 /MB composite and HR-XPS spectra of C_3N_5 /MB composite in (b) C1s, (c) N1s, (d) Na1s, (e) Cl2p, and (f) O1s regions. **Page S2619**

Figure S4. Solid state CP MAS 1H NMR spectra of (a) melem hydrazine, MH and (b) C_3N_5 . **Page S20**

Figure S5. Raman spectra of (a) melem, (b) melem hydrazine, MH, (c) g- C_3N_4 and (d) C_3N_5 . **Page S21**

Figure S6. (a) Tauc plot of g- C_3N_4 (blue) and C_3N_5 (red) for band-gap determination and (b) Mott Schottky plot of g- C_3N_4 (blue) and C_3N_5 (red) in 0.5 M Na_2SO_4 at 1K frequency. **Page S22**

Figure S117. Electrochemical impedance spectroscopy (EIS)-Nyquist plots of g- C_3N_4 in dark (black) and 1 Sun irradiation (blue) and C_3N_5 in dark (green) and 1 Sun irradiation (red). All measurement was performed in 0.1 M Na_2SO_4 at frequencies range of 0.01 kHz to 25 kHz. **Page S272**

Figure S128. Photocurrent response for the light on-off experiment at 505 nm Wavelength light (40.48 mW cm^{-2}) by for g- C_3N_4 (blue) and C_3N_5 (red) sample in 0.1 M Na_2SO_4 . **Page S283**

Figure S9. PL spectra of (a) g- C_3N_4 , (b) C_3N_5 and (c) C_3N_5 /MB composite at different sample spots obtained by using two photon laser in femtosecond fluorescence life time instrument and two photon fluorescence images of (d) g- C_3N_4 , (e) C_3N_5 , and (f) C_3N_5 /MB composite. **Page S24**

Figure S10. Zeta potential distribution of C_3N_5 for calculating surface charge. **Page S25**

Figure S11. Comparison of (a) FTIR spectra, (b) Raman spectra, (c) PL spectra using 360 nm excitation wavelength, and (d) CP-MAS ssNMR of C_3N_5 .

~~and C₃N₅/MB composite. Page S26~~

~~Figure S12. EELS spectra of g-C₃N₄ and C₃N₅ showing σ^* and π^* peaks in C K edge and N K edge energy loss. Page S27~~

~~Figure S13. TGA thermogram of g-C₃N₄ (blue) showing loss of NH₂ and heptazine ring system and C₃N₅ (red) showing loss of NH₂ and azo nitrogen's and heptazine ring system. Page S28~~

Figure S134. Photocurrent density vs applied potential plot of C₃N₅ and g-C₃N₄ (a) under solar simulated AM1.5 G irradiation with and without Na₂S. (b) under 450 nm and 505 nm LEDs irradiation. (c) ABPE% of C₃N₅ and g-C₃N₄ without and with Na₂S (d) IPCE of C₃N₅ and g-C₃N₄, under 450 nm and 505 nm LEDs irradiation. - Page S29

Figure S145. Photocurrent density vs time plot during the light on-off cycle for g-C₃N₄ and C₃N₅ and with 2.0 mM Na₂S Page S30

Figure S16. Raman spectra of (a) C₃N₅ and (b) C₃N₅ after annealing at 800 °C in sealed quartz tube showing specific D, G bands and 2D bands Page S30

Figure S1517. J-V characteristics under AM 1.5 one sun illumination of halide perovskite solar cells comprising an active layer of MAPbBr₃ and different electron transport layers – TiO₂ (black curve), g-C₃N₄ (blue curve) and C₃N₅ (red curve). In every case, spiro-OMeTAD was used as the hole transport layer. Page S31

Figure S1618. Action spectra showing the relative external quantum yields of halide perovskite solar cells comprising an active layer of MAPbBr₃ and different electron transport layers – TiO₂ (black curve), g-C₃N₄ (blue curve) and C₃N₅ (red curve). In every case, spiro-OMeTAD was used as the hole transport layer. Page S321

Figure S179. J-V characteristics in the dark of halide perovskite solar cells comprising an active layer of MAPbBr₃ and different electron transport layers – TiO₂ (black curve), g-C₃N₄ (blue curve) and C₃N₅ (red curve). In every case, spiro-OMeTAD was used as the hole transport layer. Page S332

Figure S1820. Cross-sectional FE-SEM images of perovskite solar cell made composed of (a) perovskite layer with bare PbX₂, (b) with 4 wt% of g-C₃N₄ and (c) with 4 wt% of C₃N₅ in PbX₂ solution. Page S343

Figure S1922. *J-V* curves of hole only device in linear scale (inset is in log-log scale) with the structure of FTO/PEDOT:PSS/Perovskite/Spiro-oMeTAD/Au **Page S35**

Figure S204. SERS spectra as a function of laser power for plasmon-exciton co-induced surface catalytic transformation of 4NBT to DMAB magnified in 1270-1470 cm^{-1} region for (c) AgNC/C₃N₅ and (d) AgNC/g-C₃N₄. **Page S364**

~~**Figure S22.** *J-V* curves of hole only device in linear scale (inset is in log-log scale) with the structure of FTO/PEDOT:PSS/Perovskite/Spiro-oMeTAD/Au **Page S35**~~
Figure S2143. TGA thermogram of g-C₃N₄ (blue) showing loss of NH₂ and -heptazine ring system and C₃N₅ (red) showing loss of NH₂ and azo nitrogen's and heptazine ring system. **Page S3728**

Figure S22. Raman spectra of (a) C₃N₅ and (b) C₃N₅ after annealing at 800 °C in sealed quartz tube showing specific D, G bands and 2D bands **Page S38**
References **Page S3936**

1. Experimental details

1.1 Reagent and materials

Analytical grade pure melamine (99%), hydrazine hydrate (55%), methylene blue (C₁₆H₁₈ClN₃S · xH₂O), NaOH (97%), HCl (37%), anhydrous Na₂SO₄ (99%), titanium (IV) isopropoxide (97%), titanium (IV) butoxide (97%), 4-nitrobenzene thiol (80%), Na₂S · 9H₂O (≥99.99%), Acetic acid (≥99.85%), HCl (37%), formamidine iodide (≥99%, anhydrous), 4-tert-butylpyridine (96%), lithium bis(trifluoromethanesulfonyl)-imide and spiro-OMeTAD (99%) were procured from Sigma Aldrich. Acetonitrile (99.8%), lead iodide (99%) and lead

Formatted: Left, Space After: 8 pt, Line spacing: Multiple 1.08 li

Formatted: Justified, Space After: 0 pt, Line spacing: 1.5 lines, Don't adjust space between Latin and Asian text, Don't adjust space between Asian text and numbers

Formatted: Font: (Default) Times New Roman

bromide (+98%) were purchased from Acros Organics. Methylammonium bromide was obtained from Dyesol. Chlorobenzene (99.8%), titanium (IV) chloride (99.9%), dimethylformamide (DMF) (99.8%) and dimethylsulfoxide (DMSO)(≥99.9 %) were purchased from Fisher Scientific. Transparent titania paste (18NR-T)(Average Nanoparticle Size (active) - 20nm) was purchased from Greatcell Solar. Chemicals were used as received without any further purification. Fluorine-doped tin oxide (FTO), (80-82% transmittance) was purchased from Hartford Tec Glass Company and surface was cleaned by ultrasonication for 10 min in acetone, methanol and de-ionized water respectively. HPLC grade water and solvents were used throughout experiments.

1.2 Physicochemical characterization

The surface morphological features of materials were determined by using Helium ion microscope, by using a Zeiss Orion NanoFab HiM w/ Ga-FIB (Trinity) equipped with GFIS column with a working distance of 9.3 mm, scan size of 1024x1024 and dwell time 0.2 μm. The excess charging on the sample was neutralizing by using electron flood gun to get better images. The sample for He-ion imaging was prepared by deposition of the sample on carbon tape and drying. Fine structural attributes of the sample were acquired by using high resolution transmission microscopy (HR-TEM), on a JEOL 2200 FS TEM/STEM- with EDX operating at an acceleration voltage of 200 KV. For the HR-TEM very dilute suspension of the sample in methanol was deposited on the lacy carbon-coated copper TEM grid. The obtained HR-TEM .dm3 files were processed with Gatan micrograph to determine sheets morphology and inter-planer d spacing. Further, inner shell ionization edge (core loss) of g-C₃N₄ and C₃N₅ for was determined with EELS (electron energy-loss spectroscopy). The EELS project file was processed with GATAN Pro. software and extracted data whereas later plotted in Origin. X-ray photoelectron spectroscopy (XPS) to execute surface

chemical composition, binding energy and at% of samples were obtained by using XPS (Axis-Ultra, Kratos Analytical) instrument equipped with monochromatic Al-K α source (15 kV, 50 W) and photon energy of 1486.7 eV under ultrahigh vacuum ($\sim 10^{-8}$ Torr). The binding energy of C1s core level (BE \approx 284.8 eV) of adventitious hydrocarbon was used as a standard to assign other elements binding energy (BE) and the carbon correction value. The deconvolution of obtained raw data in-to various peak components was done by using CasaXPS software and exported .csv files were plotted in origin 8.5. To elucidate the chemical structure of materials ^1H , ^{13}C and ^{15}N solid-state nuclear magnetic resonance (NMR) spectra were acquired on a Bruker Avance 500 NMR ($B_0 = 11.75$ T) equipped with a 4 mm double resonance MAS NMR probe. The ^{13}C and ^{15}N spectra of natural abundance samples were acquired using the cross polarization¹ technique, with contact times of 3 ms (^{13}C) or 5 ms (^{15}N), a $4.0\ \mu\text{s}$ $\pi/2$ pulse ($\gamma B_1/2\pi = 62.5$ kHz) and a recycle delay of 3.0 s, and with broadband proton decoupling ($\gamma B_1/2\pi = 62.5$ kHz) via two-pulse phase modulation (TPPM). Powdered samples were packed into 4 mm zirconia rotors and all spectra were acquired under magic-angle spinning (MAS) conditions using a spinning frequency of 10 kHz. ^{13}C spectra were referenced to TMS ($\delta(^{13}\text{C}) = 0.00$ ppm) by setting the high frequency ^{13}C peak of solid adamantane to 38.56 ppm. ^{15}N spectra were referenced to nitromethane $\delta(^{15}\text{N}) = 0.00$ ppm by setting the isotropic peak of a glycine sample (98 % ^{15}N) to -347.6 ppm. NB: Liquid NH_3 is also a common ^{15}N reference compound ($\delta(^{15}\text{N}) = -380$ ppm wrt nitromethane). To convert the values reported here with respect to liquid NH_3 at 0 ppm one can easily achieve this by adding 380 ppm to all reported values ($\delta_{\text{wrtNH}_3} = \delta_{\text{reported}} + 380$ ppm). ^1H MAS NMR data were acquired using a Bloch² pulse with a $4.0\ \mu\text{s}$ $\pi/2$ pulse ($\gamma B_1/2\pi = 62.5$ kHz) and a recycle delay of 3.0 s. ^1H signals were referenced with TMS ($\delta(^1\text{H}) = 0.00$ ppm) by setting the isotropic peak of adamantane to 1.85 ppm. The change in functional groups moieties of materials and their IR active vibration were

investigated with the help of Fourier transform infrared (FT-IR) spectroscopy recorded on a Digilab (Varian) FTS 7000 FT-Infrared Spectrophotometer with UMA 600 Microscope using a ZnSe ATR accessory. For acquiring the spectra, samples were deposited on the ZnSe crystal and nitrogen gas flow was maintained through the ATR assembly and spectra were collected by averaging 64 scans in the frequency range of 450–4000 cm^{-1} . The phase structure and crystalline properties to of materials were explored by X-ray powder diffraction (XRD) spectra recorded on Bruker D8 Discover instrument using Cu-K α radiation (40 kV, $\lambda = 0.15418 \text{ nm}$) equipped with a LynxEYE 1-dimensional detector. The spectra were recorded with a scan size of 0.02° in the range of 2 θ value 4–60°. The UV-Vis absorption spectra of materials in diffuse reflectance mode were collected using a Perkin Elmer Lambda-1050 UV–Vis-NIR spectrophotometer equipped with an integrating sphere accessory. The steady-state photoluminescence (PL) spectra of materials were acquired on Varian Cary Eclipse fluorimeter xenon lamp excitation source and a slit width of 5 nm. The vibrational properties of materials were executed with Raman spectroscopy using were recorded on a Thermo Scientific DXR2 Raman Microscope using the 634 nm excitation line with an incident power of 20 mWcm^{-2} . The spectra were accumulated for 60 seconds s using 50 μm confocal pinhole apertures slit, a 2 cm^{-1} /CCD pixel element spectral dispersion grating. The sample was deposited on a glass slide and laser spot was focused on the sample surface and the scattered light was collected. Time-resolved photoluminescence (TRPL) curves were recorded using a homemade single photon counting. Samples were photoexcited by 405-nm picosecond diode laser (Alphas GmbH) operated at a frequency of 13 MHz to excite the samples, and a Becker-Hickl HPM-100-50 PMT interfaced to an SPC-130 pulse counter system. This setup has a response time of ~100 ps. Electron paramagnetic resonance (EPR) spectra of material to was ensued on a Bruker model E-580 (EMXnano Bench Top system) spectrometer (Germany) equipped with a 400 W

mercury-lamp (Lot Quantum-Design GMBH) as the light source and helium flow cryostat (Oxford CF935 helium flow cryostat), operating at X band microwave frequency (~ 9.64 GHz). The operation setting for EPR measurement was as follow: Power 3.162 mW, center field 33440 G, cavity Q quality factor was kept above 4000. The sample was charged in a quartz tube and covered with air-tight lids and EPR spectra were accumulated under dark and light at liquid 100 K using liquid nitrogen. Standard samples was used for the calibrations and obtained field values were converted into g value by following expression $g = h f / m_B B$. where, g is Lande factor, h is plank constant (6.62×10^{-34} J.s), f is frequency (9.64 GHz Hz), m_B is Bohr magneton ($9.2740154 \times 10^{-24}$ J/T) and B is magnetic field is Tesla. In order to execute fluorescence nature at different sample spots Fluorescence lifetime imaging microscopy (FLIM) was performed by exciting the samples by 750 nm femtosecond Ti:sapphire laser, and then imaging the resulting PL using a Zeiss LSM 510 NLO multi-photon microscope equipped with a FLIM module consisting a Hamamatsu RS-39 multichannel plate detector, a filter wheel, and a Becker Hickl Q5 SPC730 photon counting board. Elemental analysis for determination of CHNS content of material was carried out on a Thermo Flash 2000 Elemental Analyzer. The surface properties like Brunauer–Emmett–Teller (BET) surface area, Barrett–Joyner–Halenda (BJH) porosity, pore volume of materials was examined by N_2 adsorption–desorption isotherms at 77 K by using Autosorb Quantachrome 1MP instrument. Thermal stability of samples was evaluated by thermogravimetric analyses (TGA) using a thermal analyzer TA-SDT Q-600. The Aanalysis was carried out in the temperature range of 40 to 900 °C under nitrogen flow with a heating rate of $10^\circ\text{C min}^{-1}$. To measure the change in surface potential (SP) or contact potential difference (CPD) of materials at different wavelength and elucidate nature of charge carrier dynamics, peak force KPFM (Kelvin probe force microscopy) was used on $g\text{-C}_3\text{N}_4$ and C_3N_5 samples using Dimension Fast Scan Atomic Force

Microscope (Bruker Nanoscience Division, Santa Barbara, CA, USA). For measurement materials were dispersed in DMF (10 mg/mL) using ultrasonication and a thin film was spin casted on FTO in three sequential depositions at 500 rpm followed by drying at 150 °C for 30 min. The measurements were performed in the presence and absence of 450, 520 and 635 nm wavelength diode laser (Thorlabs). A custom-made optical setup was used for shining laser perpendicularly of the samples. SCM-PIT cantilever of 4.4 N/m stiffness was employed to conduct the KPFM experiments. The surface potential of the samples was measured at 75 nm lift height at 2 kHz lockin bandwidth by maintaining scan speed of 1 Hz. Samples were grounded with the AFM chuck using a conducting copper tape. The surface potential was mapped by sample routing at zero tip bias. Dark and light conditions were maintained for 5 min, prior to performing the experiments to achieve the equilibrium condition of carrier transport. The work function of Pt-Ir tip was calibrated by measuring the contact potential difference (CPD) of HOPG and the Pt tip using the following equation and found to be 5.04 eV.

$$\text{EF (tip)} = 4.6 \text{ eV (Work function of HOPG)} + \text{VCPD (HOPG and Pt tip)}$$

1.3 Electrochemical characterization

The electrochemical studies were performed by using a CHI660E series electrochemical workstation using Ag/AgCl reference electrode. For the electrochemical measurements three electrode systems was assigning C₃N₅ and g-C₃N₄ deposited on FTO as an anode, Pt as cathode and Ag/AgCl as a cathode reference electrode. The photocurrent response (*J*-*V* curve) of materials was measured in 0.1 M Na₂SO₄ by linear sweep voltammetry by sweeping voltage at the rate of 10 mV/sec from -0.8 V to +0.8 V vs Ag/AgCl. A Solar simulator (Newport, Oriel instrument USA, model 67005) was used as AM1.5G solar light source having

a power density of 100 mW m^{-2} at the surface of the sample. To determine photoresponse at higher wavelength 450 and 505 nm wavelength LED was used having a power density of 54.15 mW cm^{-2} and 40.48 mW cm^{-2} at the surface of the sample respectively. The EIS measurement was done in the dark and AM1.5G solar radiation using a three electrodes configuration at an applied voltage of -0.5 V vs Ag/AgCl in $0.1 \text{ M Na}_2\text{SO}_4$, with AC amplitude of 0.005 V in the frequencies range of 0.01 kHz to 25 kHz . The impedance-potential values for Mott–Schottky plots were determined in $0.5 \text{ M Na}_2\text{SO}_4$ in the voltage range of -1 V to $+1 \text{ V}$ at 1 K frequency.

2.0 Synthesis procedures

2.1 Synthesis of Melem (2,5,8-triamino-s-heptazine)³

For the synthesis of melem (2,5,8 -triamino-s-heptazine) a certain amount of melamine was heated at $425 \text{ }^\circ\text{C}$ for overnight in an alumina crucible covered with a lid. The obtained powder with yellowish tinge was crushed and suspended in DI water. The obtained suspension was refluxed for several hours to remove un-reacted melamine and other impurities. The resulting white product was collected by centrifugation and dried at room temperature. All the data well matched with previously reported literature.

2.2 Synthesis of 2,5,8-trihydrazino-s-heptazine or melem hydrazine (MH)⁴

The monomeric unit 2,5,8-trihydrazino-s-heptazine or melem hydrazine was synthesized by hydrothermal reaction between melem and hydrazine hydrate with slight modification in previous literature procedure. In brief, 1.6 g (7.5 mmol) of melem was dispersed in 15 mL (0.25 mol) of 55% aqueous hydrazine hydrate solution and sealed in a 25 mL Teflon lined autoclave. The autoclave was heated at $140 \text{ }^\circ\text{C}$ in an oven for 24 h hours. After cooling the

obtained yellowish solution suspension was transferred to a 100 mL beaker and 10% HCl was added to maintain pH in between 1–2. This solution was filtered to remove un-reacted solid residue containing melem. The filtrate was precipitated by adding 10 % NaOH solution by maintaining pH in between 7.5 – 8.5. The obtained solid was again dissolved in HCl, filtered and re-precipitated in NaOH and this procedure was followed for three times. Finally, obtained solid was washed several times with DI water and ethanol and dried under vacuum. All the data were well matched with previously reported literature.

NMR (CP/MAS, ppm): ^1H : 5.11, s (–NH– and –NH₂), ^{13}C : 164.13, 159.16, 154.23, ^{15}N : –207.44, –251.55, –273.50, –316.73.; FTIR: 3209, 2926, 1595, 1475, 1388, 1192, 1116, 1099, 1008, 960, 794, 723, 648, 495 cm^{-1} .; Raman: 3365, 3066, 2896, 1589, 1528, 1409, 1309, 1156, 983, 747, 544, 470, 342, 129, 104 cm^{-1} .

2.3 Synthesis of C₃N₅ polymer

C₃N₅ polymer was synthesized by heating melem hydrazine (2,5,8-trihydrazino-s-heptazine) at a temperature of 450 °C with a heating rate of 2 °C and holding at 450 °C for 2 h. The obtained orange powder was used for subsequent experiments without any further treatment. The BET surface area (S_{BET}) of C₃N₅ was found to be 1.781 $\text{m}^2 \text{g}^{-1}$.

CHN analysis wt%, observed (theoretical): N- 61.27 (66.02), C- 31.81 (33.98), H- 2.68 (0.00), Empirical formula: C₃N_{4.95}H_{1.01} (C₃N₅)

XPS elemental Analysis at%, observed (theoretical): N- 63.24 (62.50), C-36.76(37.50), Empirical formula: C₃N_{5.16} (C₃N₅), N_{ring}:N_{bridging} at% and ratio (theoretical): 60.47:39.53 and ~3:2, (60:40, 3:2).

NMR (CP/MAS, ppm): ^1H : 9.18, s (broad) (residual H, intercalated water and carbonyl H), ^{13}C : 164.41, 155.97, ^{15}N : -197.33, -247.88, -270.99.; FTIR: 3305, 3140, 2164, 1608, 1402, 1323, 1271, 1143, 1070, 970, 794, 453 cm^{-1} .; Raman: 2591, 1308, 1258 cm^{-1} .

2.4 Synthesis of $\text{g-C}_3\text{N}_4$ ⁵

For comparison, graphitic carbon nitride ($\text{g-C}_3\text{N}_4$) powder was synthesized by direct heating of melamine at 550 °C with a heating rate of 8 °C min^{-1} up to 300 °C and 2 °C min^{-1} up to 550 °C and finally holding the temperature 550 °C for 4 h. The BET surface area (S_{BET}) of $\text{g-C}_3\text{N}_4$ was found to be 11.471 $\text{m}^2 \text{g}^{-1}$.

3.0 Experimental for dye absorption

To probe the applicability of materials in dye absorption methylene blue (MB) was chosen as model coloring organic contaminant. All the absorption studies were performed at room temperature and pH-7 under the dark condition to avoid any photo-induced effects. To execute absorption kinetic studies, a solution containing 10 ppm of methylene blue was prepared and 50 mL of the solution was placed in a beaker followed by addition of 50 mg C_3N_5 or $\text{g-C}_3\text{N}_4$. As the absorption process was extremely fast initially, so the sample was withdrawn after every 1 min for 10 min interval, and later time of sampling was increased to 15 and 30 min. The collected samples were centrifuged at 10000 rpm using a centrifuge device to remove the solid materials. The supernatant was analyzed with UV-Vis spectroscopy. Methylene blue displays a strong absorption peak around 664 nm. A series of standard solutions were prepared, and a calibration curve was prepared by measuring absorbance and quantification of treated solution. To investigate the nature of interaction

between C_3N_5 and MB the centrifuged solid called C_3N_5 /MB composite was dried at 70 °C under vacuum. Further, g- C_3N_4 was also used under identical condition for comparing the dye absorption performance.

4.0 Photo-electrochemical measurements

For the photo-electrochemical measurement, clean FTO glass was coated with a 60 nm thick TiO_2 seed layer by following our previously reported spin cast procedure using titanium isopropoxide solution as a precursor.⁶ The g- C_3N_4 and C_3N_5 powder were mixed with TiO_2 (5 nm) nanoparticles in α -terpineol solution which works as film forming agent. The obtained suspension was drop-casted on the TiO_2 coated FTO and heated at 250 °C for 1 h. The photo-electrochemical water splitting performance of samples was determined on three electrode working station using Ag/AgCl as a reference electrode. The g- C_3N_4 or C_3N_5 containing FTO works as a working electrode (photoanode) while a Pt electrode was used as counter electrode (photocathode). The surface of anode was sealed with Surlyn by keeping a 0.3167 cm² window open and electrodes were immersed in 0.1 M Na_2SO_4 electrolyte. The photoanode was irradiated with the solar simulator at possessing AM1.5 G filter having a power density of 100 mW cm⁻². The current density vs applied potential graph was obtained by sweeping voltage from -0.8V to +0.8 V. Further, photoresponse at different wavelength was measured by using 450 and 505 nm LED light. LED's were calibrated with a photodiode and the LED intensity on the surface of samples was maintained 54.15 W cm⁻² at 450 nm, 40.48 mW cm⁻² at 505 nm. Dark current was also measured for comparing the photo-response of samples. Additional photoelectrochemical

experiments using 2.0 mmol Na₂S as hole scavenger was also carried out under identical reaction conditions.⁷

5.0 Fabrication of solar cell

A thin compact layer of TiO₂ was deposited on the cleaned FTO:glass substrate. To prepare the precursor solution for the deposition of compact TiO₂, 369 μ L of titanium (IV) isopropoxide and 70 μ L of 1.0 M HCl were separately diluted in 2.53 mL of isopropanol. Diluted HCl was added drop by drop into the diluted titanium (IV) isopropoxide solution under stirring. After overnight stirring of the mixed solution, it was filtered using a 0.2 μ m filter and deposited over cleaned FTO:glass substrates by spin casting at 3000 rpm for 30 s, followed by calcination at 450 °C for 30 min⁸. 18NR-T titania paste was dissolved in absolute ethanol in the ratio of 1:3.5 wt% and spin casted on compact TiO₂ layer at 4000 rpm for 40 s followed by annealing at 450 °C for 30 min. On mesoporous TiO₂ layer, 0.1 M of lithium bis(trifluoromethanesulfonyl)-imide dissolved in acetonitrile was spin-coated at 3000 rpm for 30 sec followed by annealing at 450 °C for 30 min. On FTO/TiO₂ by spin casting followed by calcination at 500 °C for 30 min. Then 636.4 mg of PbI₂ and 90 mg of PbBr₂ was dissolved in 1 mL of DMF and 160 μ L of DMSO. For g-C₃N₄/C₃N₅ based device 4 wt% of g-C₃N₄/C₃N₅ relative to PbX₂ (where X=I and Br) was added in the PbX₂ solution. All the solutions were stirred at 70 °C for 12 h. A solution of 1100 mg of FAI and 110 mg of MABr was dissolved in 15 mg of 2-propanol. PbX₂ solution was spin coated over mesoporous TiO₂ layer at 4000 rpm for 30 sec followed by annealing at 70 °C for 10 min. Then prepared FAI/MABr solution was spin coated over the PbX₂ layer at 2000 rpm for 30 sec followed by annealing at 140 °C for 30 mins. A hole transporting layer was deposited by spin-casting a solution containing 70 mg of Spiro-OMeTAD mixed with 1

mL of chlorobenzene and additives, namely 8.8 mg of lithium bis(trifluoromethanesulfonyl)-imide, 28 μ L of 4-tert-butylpyridine and 35 μ L of acetonitrile at 4000 rpm for 30 sec. A 70-nm thick layer of gold was then thermally evaporated to complete the devices. The current-voltage characteristics of the samples were measured using a Keithley 4200 semiconductor parameter analyzer. For solar cell testing, one sun AM1.5 G illumination from a collimated Class A solar simulator (Newport Instruments) was used. Solid state impedance spectroscopy (SSIS) was performed in a two-electrode configuration using a CHI-600E potentiostat.

6.0 Measurement of plasmon excitons co-induced surface catalytic transformation of 4NBT to DMAB

The plasmonic Ag nanocubes, AgNC (45 nm edge length) were synthesized by ethylene glycol and Na₂S assisted reduction of AgNO₃ according to literature procedure.⁹ Thin film of g-C₃N₄ and C₃N₅ was coated on the glass surface by spin casting 30 mg/mL solution in DMF at 500 rpm followed by heating to evaporate any residual of solvent. Then AgNC were deposited on afforded film by spin casting. To the obtained Ag decorated substrate, 4-NBT (5×10^{-5} M) in methanol solution was drop casted followed by vacuum drying. To identify the peak of DMAB peaks, Raman spectra of DMAB was digitalized from reference.¹⁰ The course of surface catalyzed reaction was monitored by surface-enhanced Raman scattering (SERS) spectroscopy using a Thermo Scientific DXR2Raman Microscope with a 532 nm laser by varying laser power from 0.1 mW to 10 mW. The spectra were accumulated for 3x25 s exposure time using, aperture 50 μ m pinhole, 2 μ m spot size and 2 cm⁻¹/CCD pixel element 900 lines/mm spectral dispersion grating.

7.0 Calculation of efficiencies

1
2
3
4
5
6
7
8
9
10 Diagnostic efficiencies of C₃N₅ and g-C₃N₄ was calculated to evaluate system/inter-face
11 performance.¹¹
12
13 *Applied bias photon-to-current efficiency (ABPE):*
14
15 The applied bias photon-to-current efficiency percentage (ABPE%) which is considered
16 photoconversion efficiency (PCE%) under applied bias was determined by plot between
17 ABPE% and applied voltage on reversible hydrogen electrode (RHE) scale. The ABPE%
18 was calculated by [the](#) following expression:
19
20
21
22
$$ABPE\ (\%) = [J\ (\text{mA cm}^{-2}) \times (1.23 - V_b) / P\ (\text{mW cm}^{-2})] \times 100 \dots\dots\dots \text{Eqn- (1)}$$

23 Where, J is the current density, V_b is applied voltage at RHE scale and P is power density of the
24 incident light.
25
26 The applied voltage on Ag/AgCl scale was converted RHE scale by using [the](#) following equation.
27
28
$$V_{RHE} = V_{Ag/AgCl} + 0.059\ \text{pH} + V^0_{Ag/AgCl} \dots\dots\dots \text{Eqn - (2)}$$

29 Where; $V^0_{Ag/AgCl} = 0.197\ \text{V}$.
30
31 From the ABPE vs RHE plot the maximum ABPE% for C₃N₅ and g-C₃N₄ was calculated to be
32 0.059 and 0.048 without Na₂S and 0.030 and 0.026 with Na₂S respectively.
33
34
35 *Incident photon-to-current efficiency (IPCE):*
36
37 The IPCE also referred as external quantum efficiency (EQE) is a measure of photocurrent
38 obtained (numbers of electrons collected) per incident photon flux as a function of
39 wavelength). The IPCE% of samples were calculated at an applied bias of 0.6 V vs
40 Ag/AgCl (1.23 V vs RHE, thermodynamic water splitting potential) using 450 nm and 505
41 nm wavelength LEDs. IPCE% was calculated using the following expression.
42
43
44
45
$$IPCE\% = [1240 \times J\ (\text{mA cm}^{-2}) / \lambda\ (\text{nm}) \times P\ (\text{mW cm}^{-2})] \times 100 \dots\dots\dots \text{Eqn- (3)}$$

46
47 Where, J is photocurrent density, λ is wavelength of incident light in nm and P is the power density
48 of incident light.
49

The IPCE% of C_3N_5 and g- C_3N_4 without Na_2S was found to be 0.51 and 0.46 at 450 nm and 0.37 and 0.35 at 505 nm respectively. While the IPCE% values for C_3N_5 and g- C_3N_4 using Na_2S was found 2.32 and 1.41 at 450 nm and 0.86 and 0.45 at 505 nm respectively.

Formatted: Font: (Default) Times New Roman, 12 pt, Bold, Font color: Black, English (Canada)

Formatted: Normal

8.0 Figures

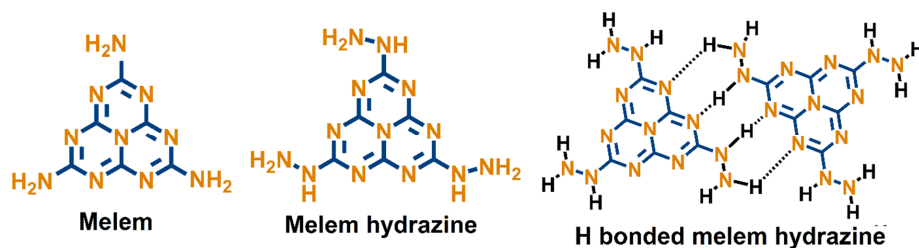


Figure S1. Chemical structures of melem, melem hydrazine, hydrogen bonded melem hydrazine

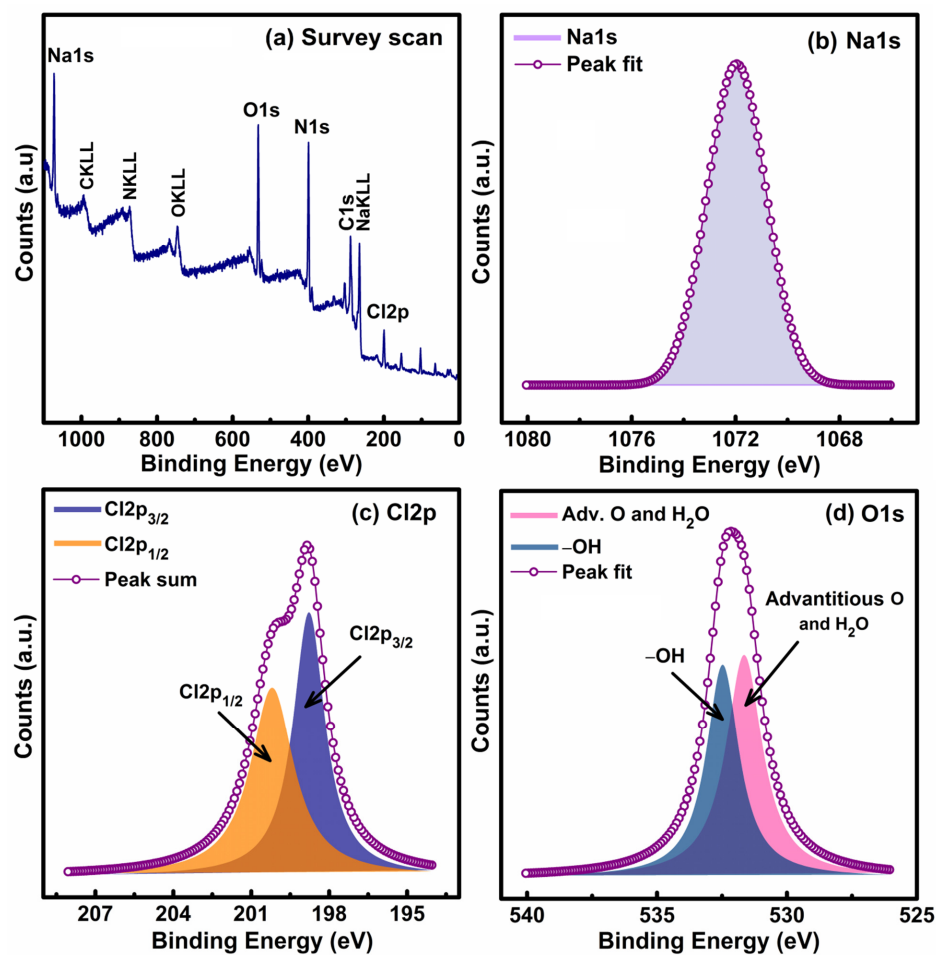


Figure S2. (a) XPS elemental survey scan of C_3N_5 , and HR-XPS spectra of C_3N_5 in (b) Na1s, (c) Cl2p, and (d) O1s regions.

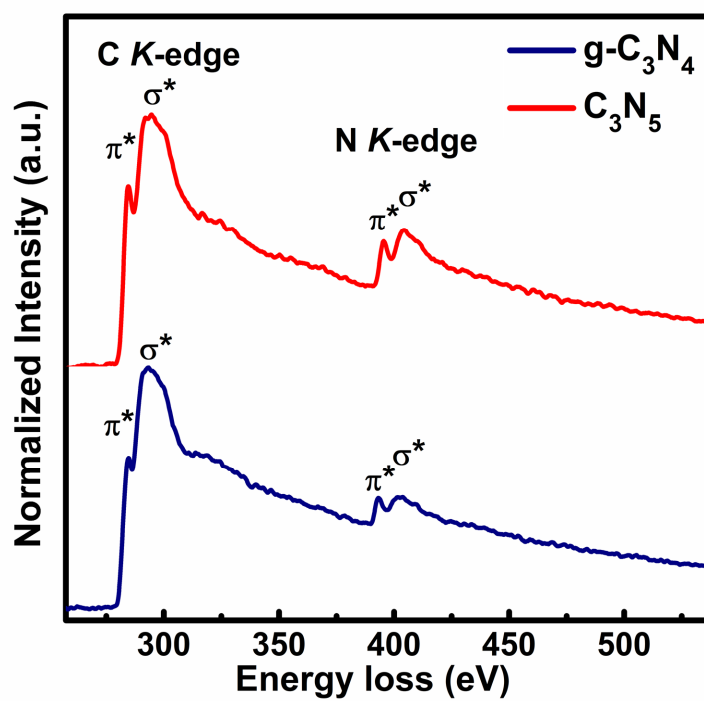


Figure S3-12. EELS spectra of $g-C_3N_4$ and C_3N_5 showing σ^* and π^* peaks in C K-edge and N K-edge energy loss

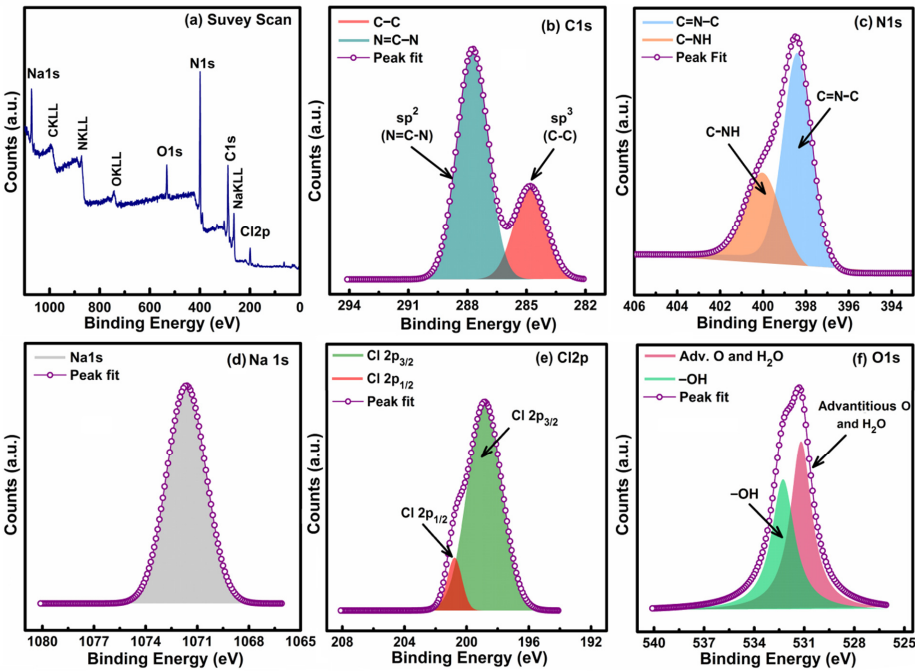


Figure S3. (a) XPS survey scan of C_3N_5/MB composite and HR XPS spectra of C_3N_5/MB composite in (b) C1s, (c) N1s, (d) Na1s, (e) Cl2p, and (f) O1s regions.

Formatted: Highlight

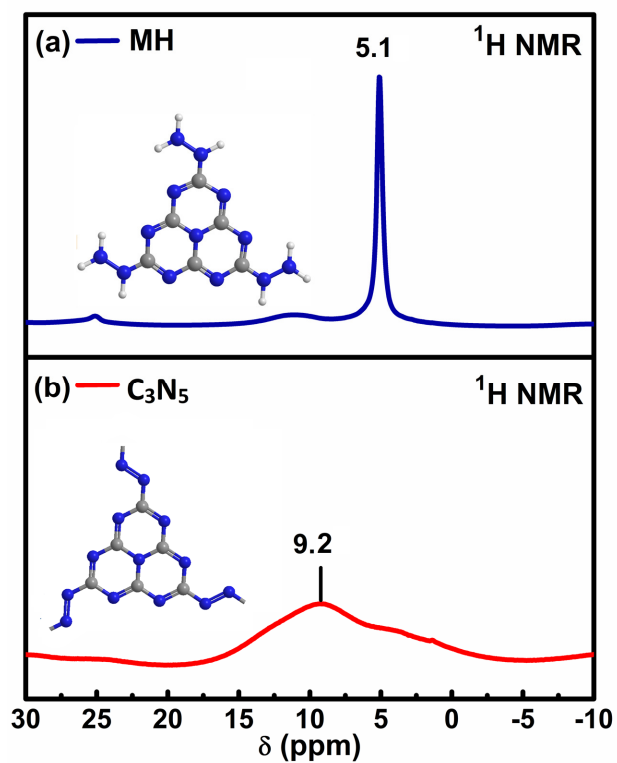


Figure S4. ^1H MAS NMR spectra of (a) melem hydrazine, MH and (b) C_3N_5

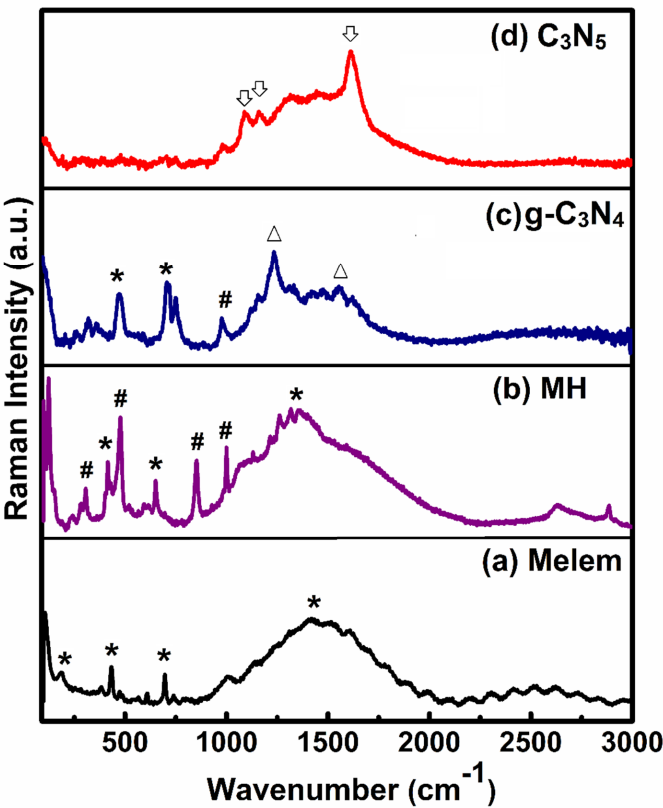


Figure S5. Raman spectra of (a) melem, (b) melem hydrazine, MH, (c) g-C₃N₄ and (d) C₃N₅

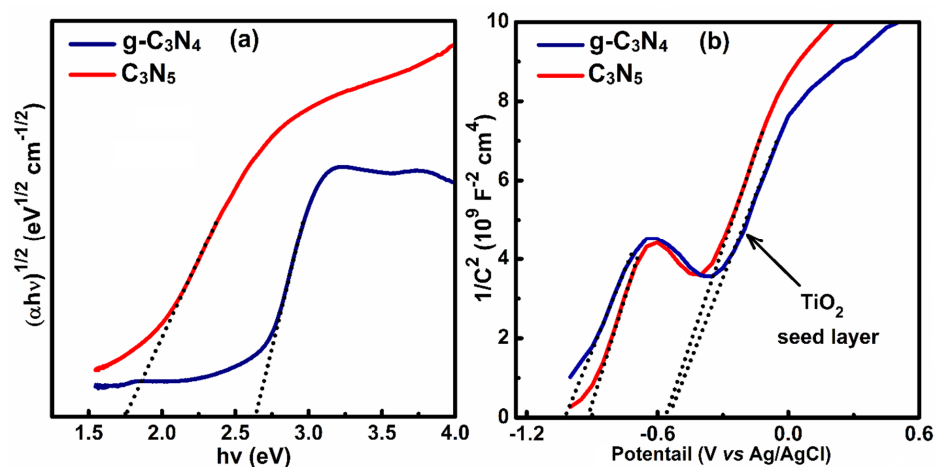


Figure S6. (a) Tauc plot of g-C₃N₄ (blue) and C₃N₅ (red) for band gap determination and (b) Mott Schottky plot of g-C₃N₄ (blue) and C₃N₅ (red) in 0.5 M Na₂SO₄ at 1K frequency.

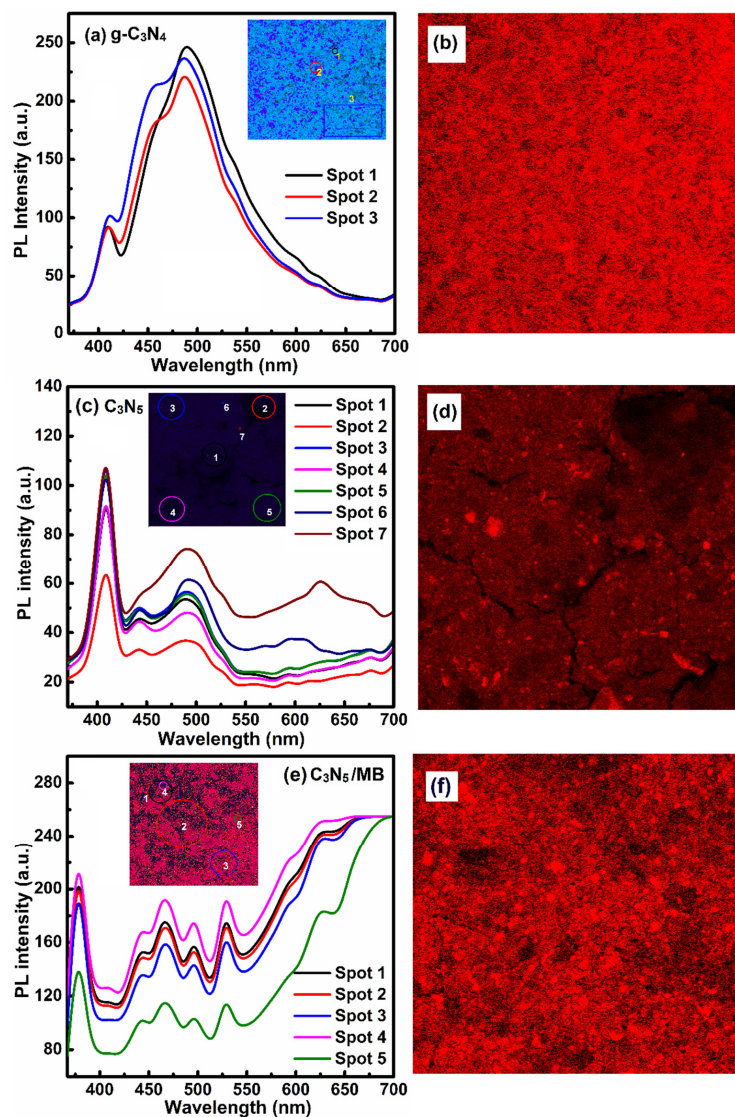


Figure S7. PL spectra obtained from fluorescence lifetime imaging (FLIM) of (a) $g\text{-C}_3\text{N}_4$, (c) C_3N_5 and (e) $\text{C}_3\text{N}_5/\text{MB}$ composite at different sample spots obtained by using two photon laser in

femtosecond fluorescence life time instrument and two photon fluorescence images of (b) g-C₃N₄,
(d) C₃N₅, and (f) C₃N₅/MB composite.

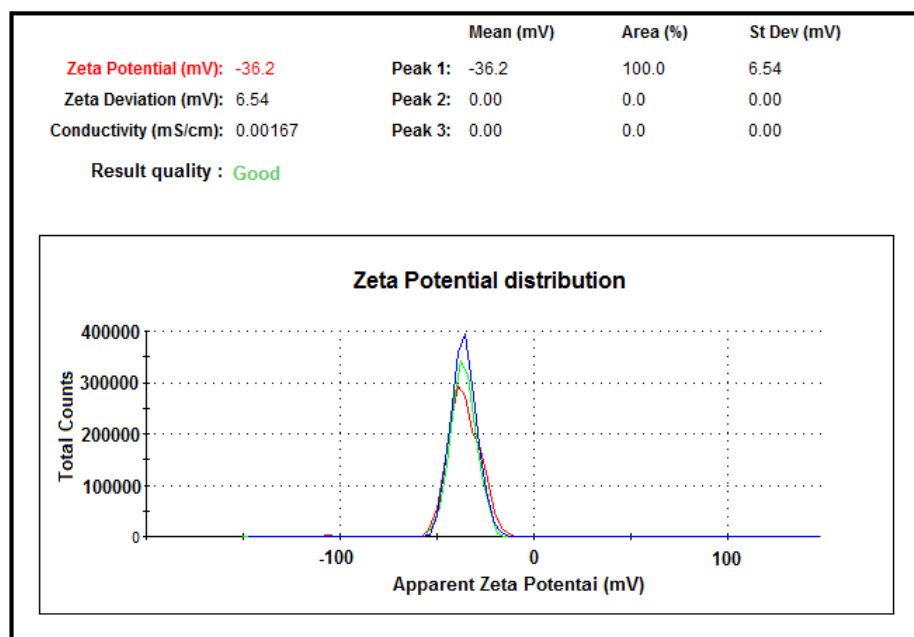


Figure S810. Zeta potential distribution of C₃N₅ for calculating surface charge.

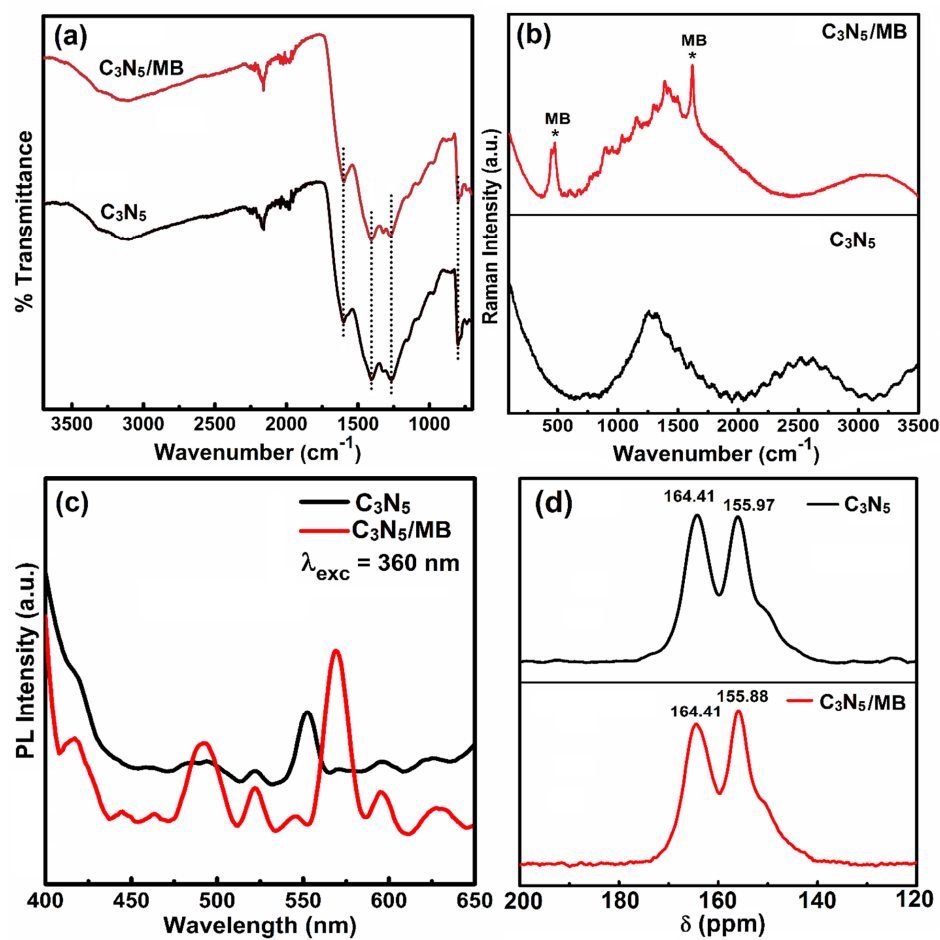


Figure S911. Comparison of (a) FTIR spectra, (b) Raman spectra, (c) PL spectra using 360 nm excitation wavelength, and (d) ^{13}C CPMAS NMR of C_3N_5 (black) and C_3N_5/MB (red) composite.

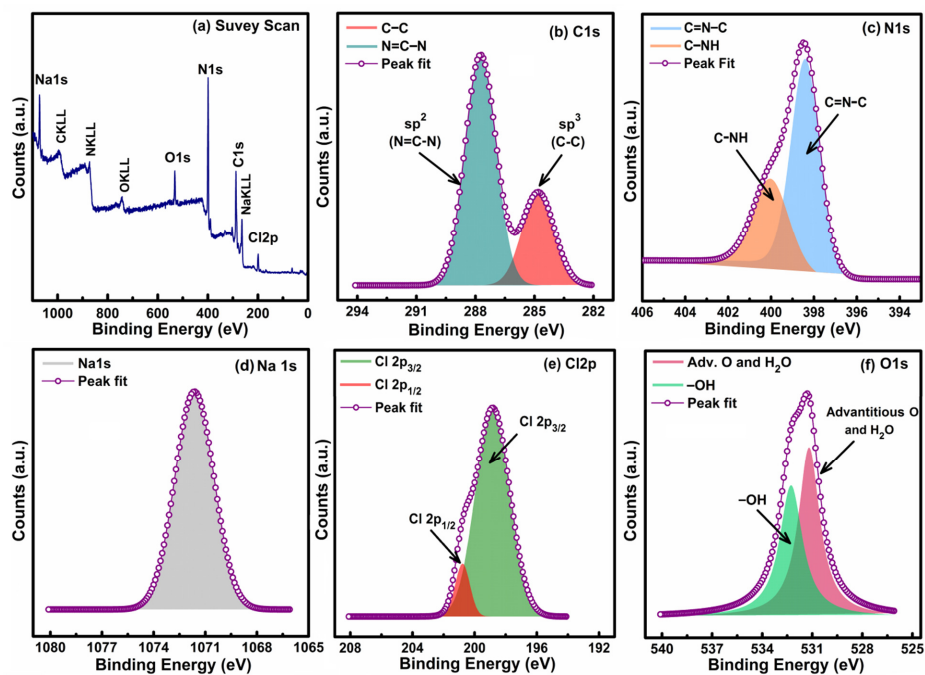


Figure S10. (a) XPS survey scan of C_3N_5/MB composite and HR-XPS spectra of C_3N_5/MB composite in (b) C1s, (c) N1s, (d) Na1s, (e) Cl2p, and (f) O1s regions.

Formatted: Not Highlight

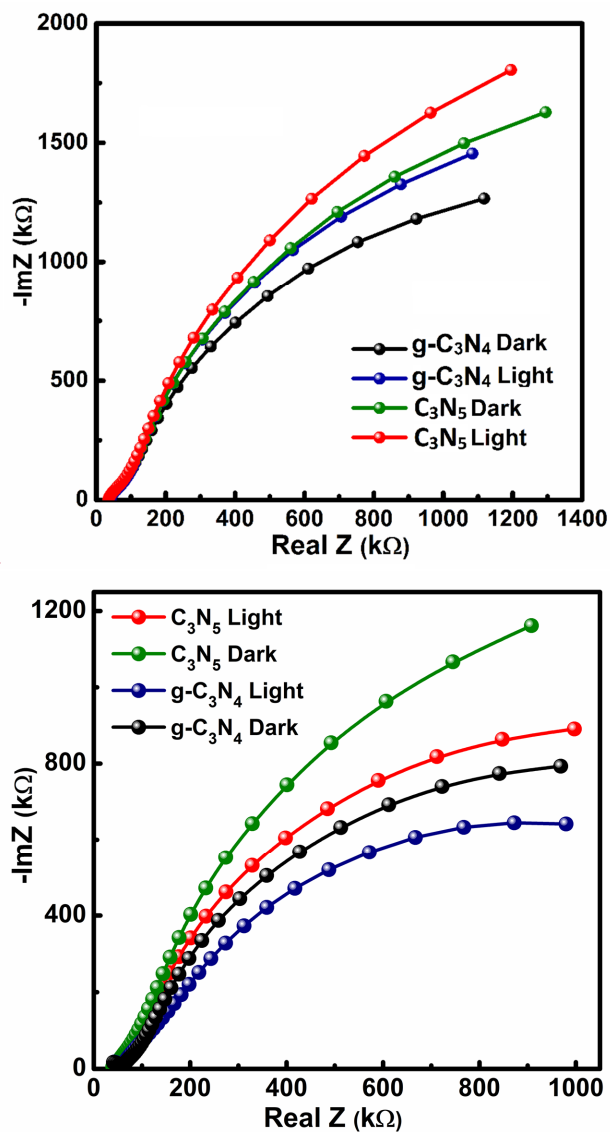
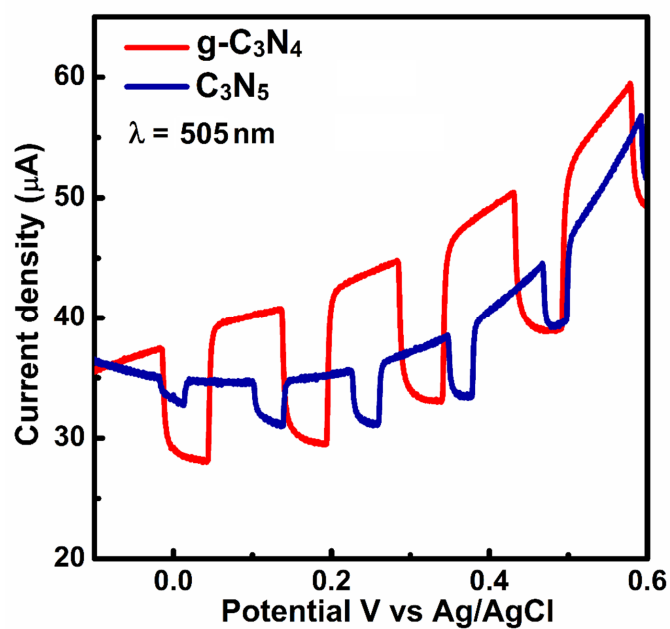


Figure S117. Electrochemical impedance spectroscopy (EIS)-Nyquist plots of g-C₃N₄ in dark (black) and AM1.5G light irradiation (blue) and C₃N₅ in dark (green) and AM1.5G light irradiation

(red). All measurement was performed in 0.1 M Na₂SO₄ at frequencies range of 0.01 kHz to 25 kHz.



Formatted: Justified, Line spacing: 1.5 lines

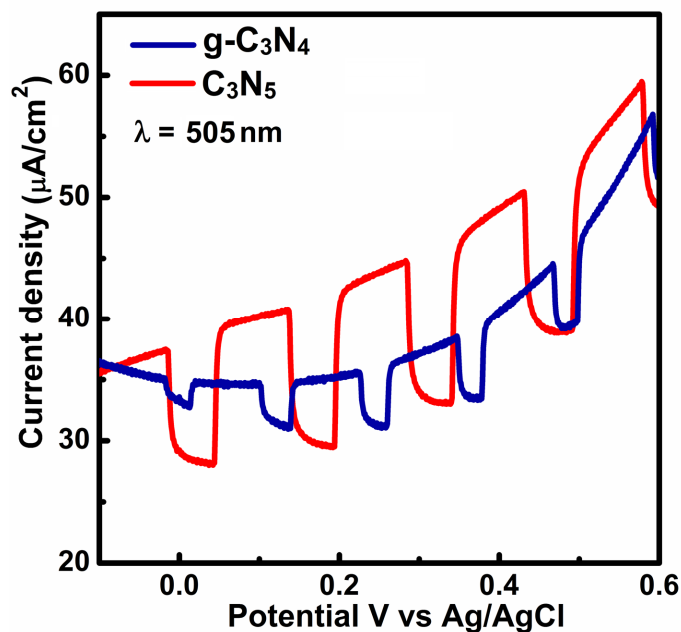


Figure S128. Photocurrent response for light on-off experiment at 505 nm wavelength light (40.48 mW cm⁻²) by for g-C₃N₄ (blue) and C₃N₅ (red) sample in 0.1 M Na₂SO₄.

Formatted: Highlight

Formatted: Highlight

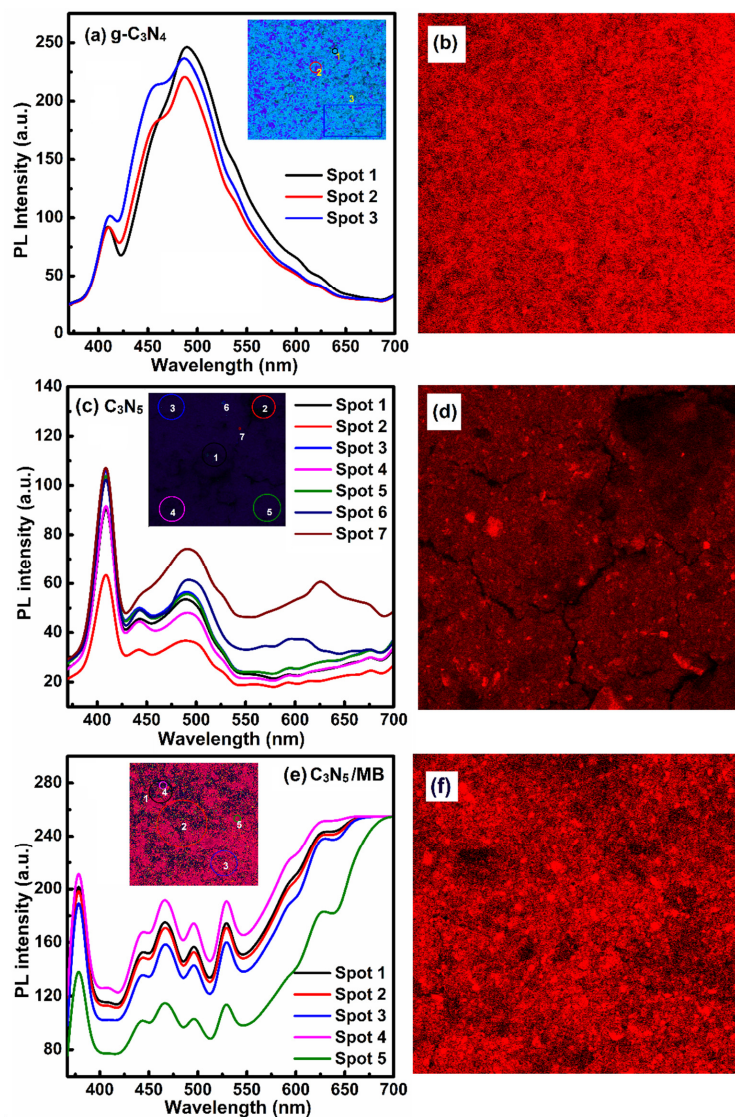


Figure S9. PL spectra obtained from fluorescence lifetime imaging (FLIM) of (a) g-C₃N₄, (b) C₃N₅ and (c) C₃N₅/MB composite at different sample spots obtained by using two-photon laser in

Formatted: Highlight

1
2
3
4
5
6
7
8
9
10
11
12
13
14
15
16
17
18
19
20
21
22
23
24
25
26
27
28
29
30
31
32
33
34
35
36
37
38
39
40
41
42
43
44
45
46
47
48
49
50
51
52
53
54
55
56
57
58
59
60

femtosecond fluorescence life time instrument and two photon fluorescence images of (d) g-C₃N₄,
(e) C₃N₄, and (f) C₃N₄/MB composite.

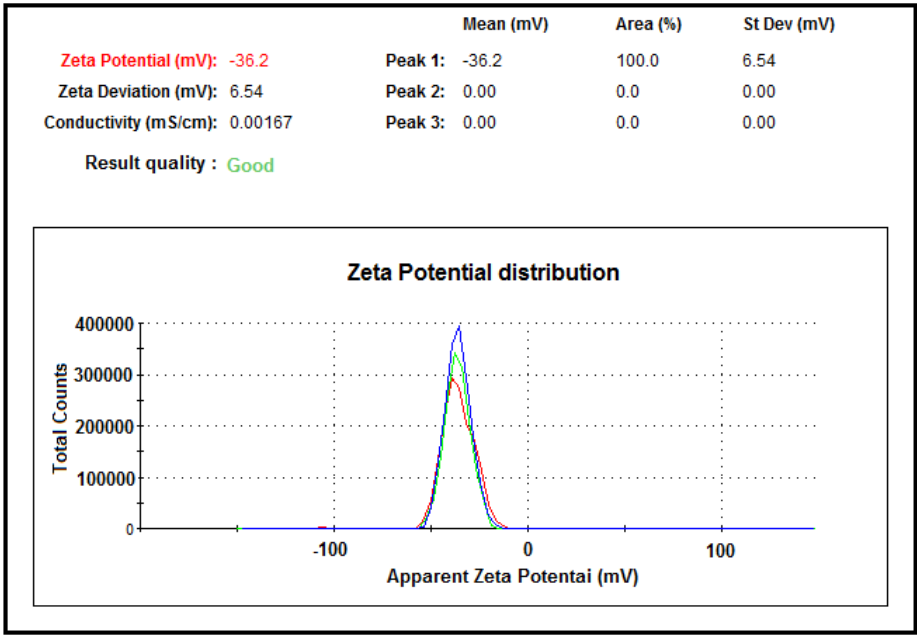


Figure S10. Zeta potential distribution of C₃N₄ for calculating surface charge.

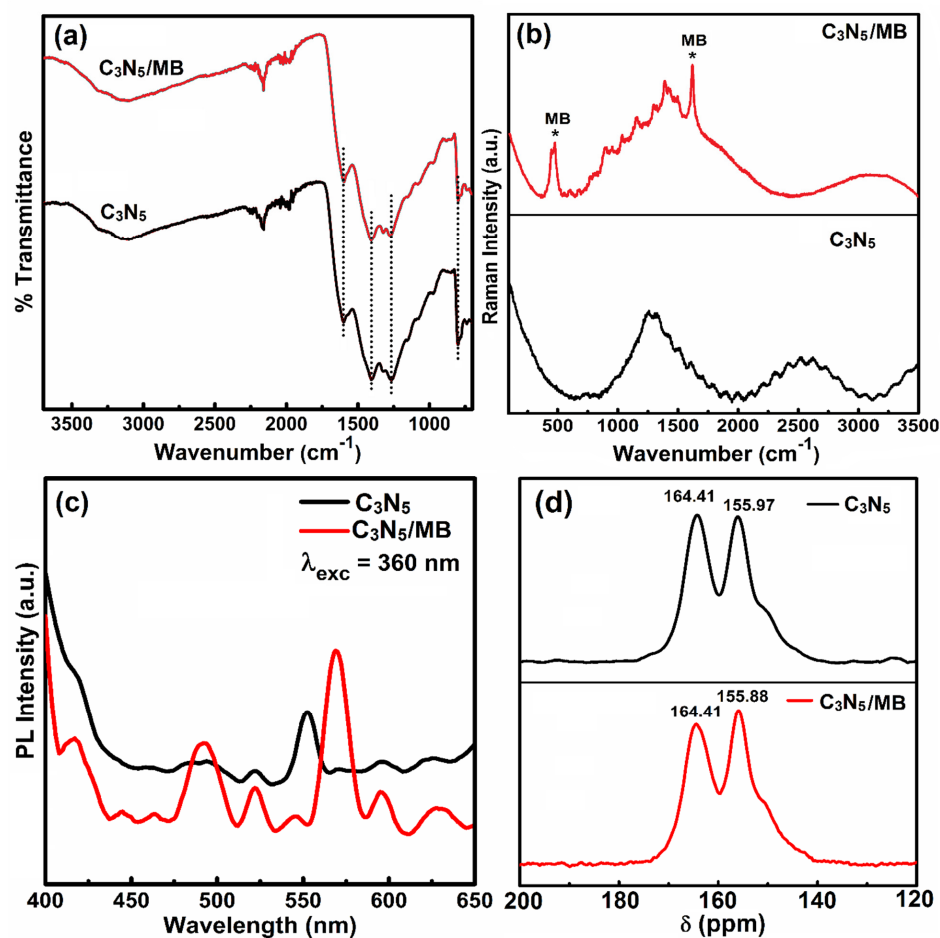


Figure S11. Comparison of (a) FTIR spectra, (b) Raman spectra, (c) PL spectra using 360 nm excitation wavelength, and (d) ^{13}C CPMAS NMR of C_3N_5 (black) and C_3N_5/MB (red) composite.

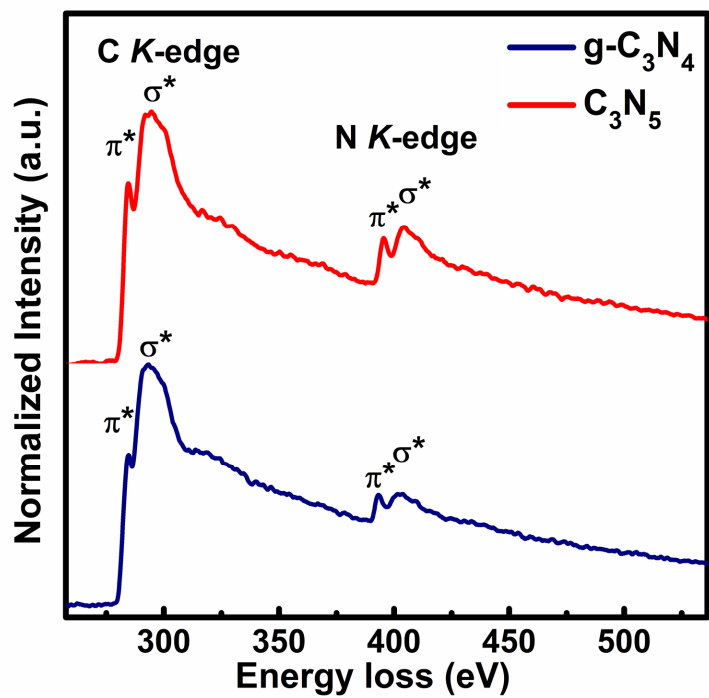


Figure S12. EELS spectra of $g\text{-C}_3\text{N}_4$ and C_3N_5 showing σ^* and π^* peaks in C K-edge and N K-edge energy loss

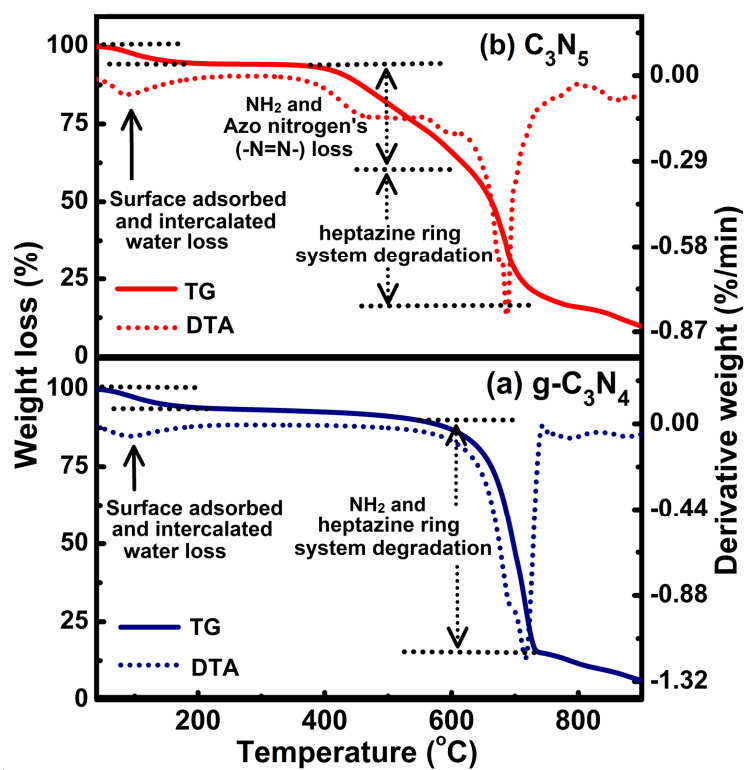


Figure S13. TGA thermogram of (a) g-C₃N₄ (blue) showing loss of NH₂ and heptazine ring system and (b) C₃N₅ (red) showing loss of NH₂ and azo nitrogens and heptazine ring system.

Formatted: Highlight

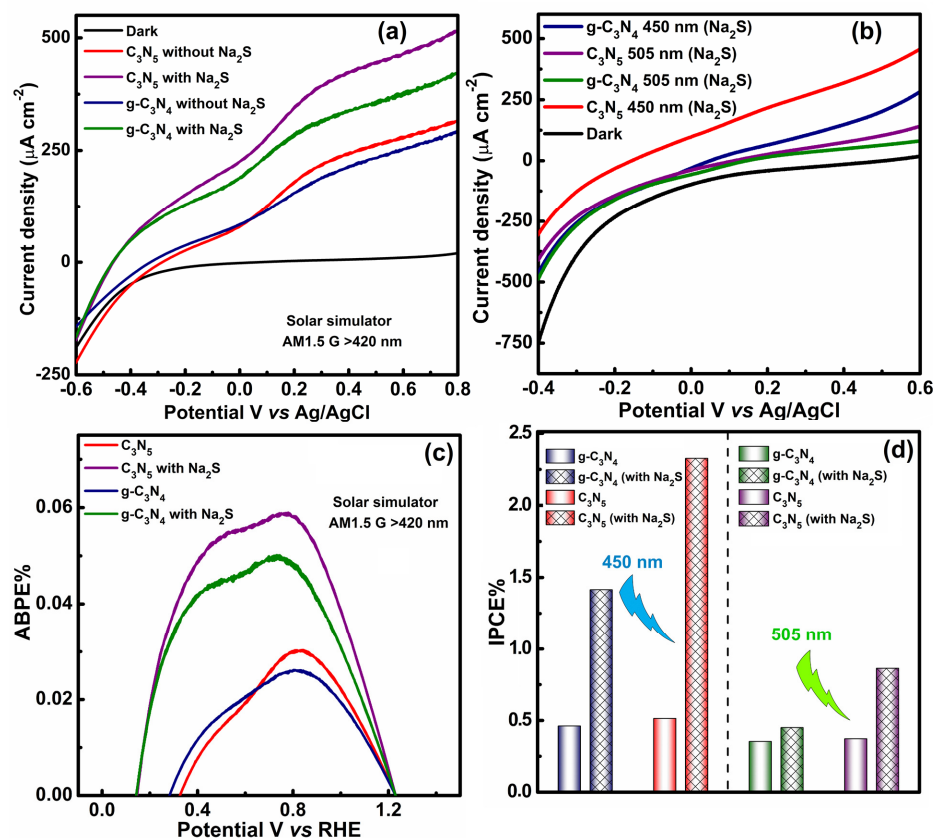


Figure S134. (a) Photocurrent density vs applied potential plot of C_3N_5 and $g-C_3N_4$ under dark conditions, under solar simulated AM1.5 G irradiation ($>420 nm$) with and without Na_2S . (b) Photocurrent density vs applied potential plot of C_3N_5 and $g-C_3N_4$ under dark conditions, under 450 nm LEDs irradiation (power density $54.15 mW cm^{-2}$), under 505 nm LEDs irradiation (power density $40.48 mW cm^{-2}$). (c) Plot between ABPE% vs potential (RHE) showing maximum ABPE% for C_3N_5 and $g-C_3N_4$ without and with Na_2S under solar simulated AM1.5 G irradiation ($>420 nm$). (d) IPCE of C_3N_5 and $g-C_3N_4$ under 450 nm LEDs irradiation (power density $54.15 mW cm^{-2}$), under 505 nm LEDs irradiation (power density $40.48 mW cm^{-2}$). All the measurements were carried out in 0.1 M Na_2SO_4 solution at a scan rate of 0.1 mV/sec). Colour legends: Dark (black), C_3N_5 without Na_2S (red), C_3N_5 with Na_2S (purple), $g-C_3N_4$ without Na_2S (blue) with Na_2S and 505 nm (green).

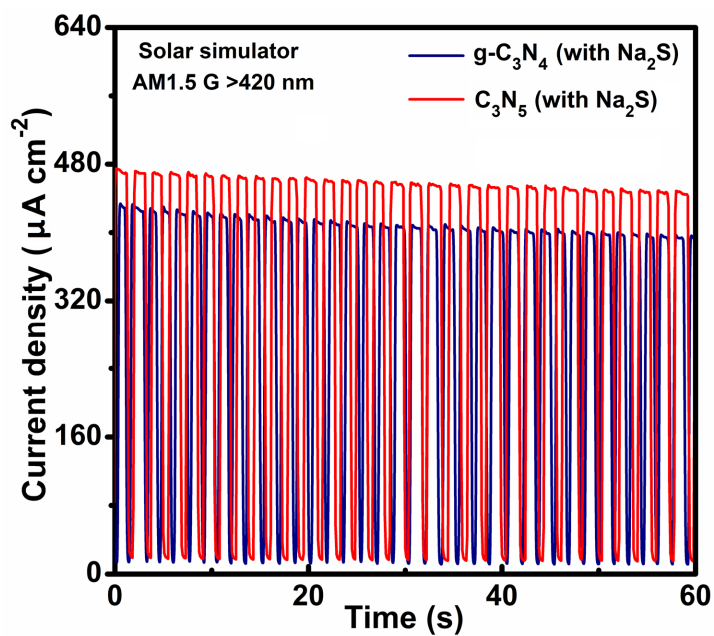


Figure S145. Photocurrent density vs time plot during light on-off cycle for $\text{g-C}_3\text{N}_4$ (blue) and C_3N_5 (red) and with 2.0 mM Na_2S at applied voltage bias +0.6 V vs Ag/AgCl.

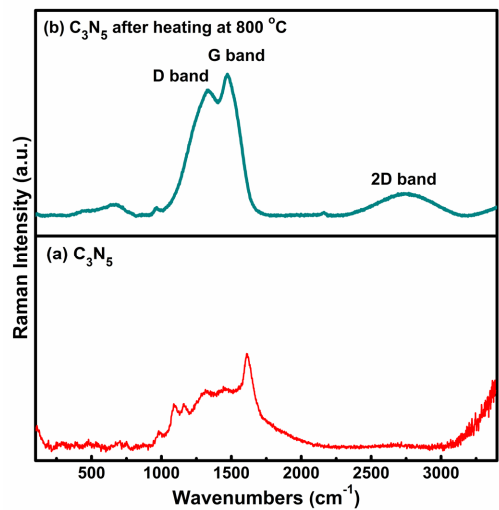


Figure S16. Raman spectra of (a) C_3N_5 and (b) C_3N_5 after annealing at 800 °C in sealed quartz tube showing specific D-, G bands and 2D band revealing transformation in N-graphene.

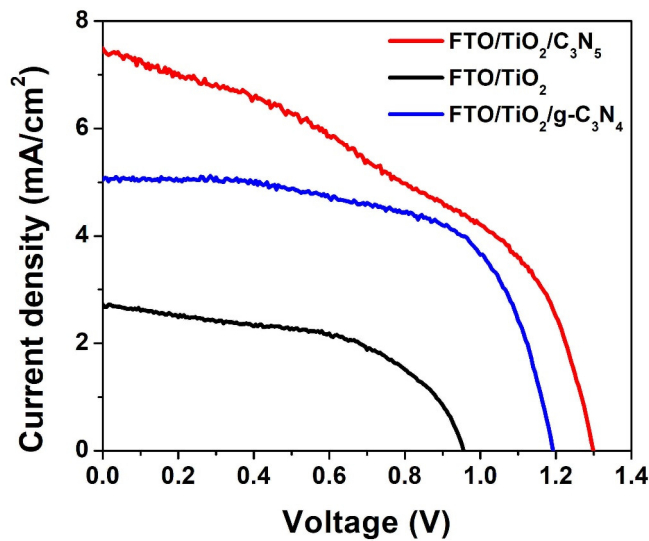


Figure S157. *J-V* characteristics under AM 1.5 one sun illumination of halide perovskite solar cells comprising an active layer of $MAPbBr_3$ and different electron transport layers – TiO_2 (black

curve), g-C₃N₄ (blue curve) and C₃N₅ (red curve). In every case, spiro-OMeTAD was used as the hole transport layer.

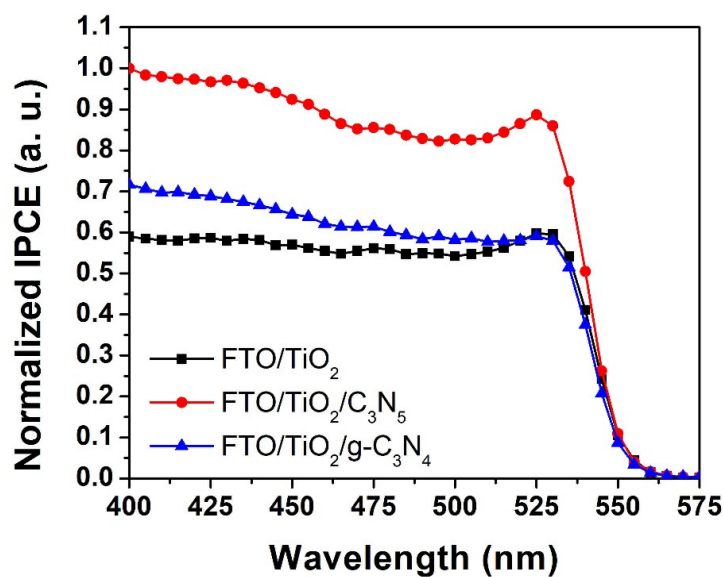


Figure S168. Action spectra showing the relative external quantum yields of halide perovskite solar cells comprising an active layer of MAPbBr₃ and different electron transport layers – TiO₂ (black curve), g-C₃N₄ (blue curve) and C₃N₅ (red curve). In every case, spiro-OMeTAD was used as the hole transport layer.

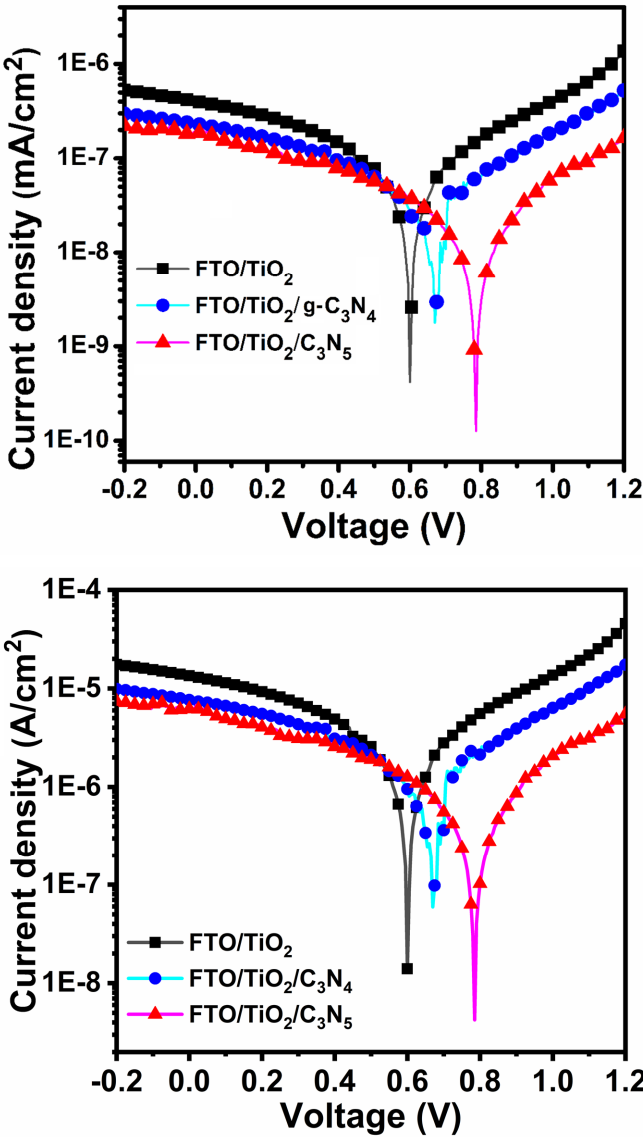


Figure S179. *J-V* characteristics in the dark of halide perovskite solar cells comprising an active layer of MAPbBr₃ and different electron transport layers – TiO₂ (black curve), g-C₃N₄ (blue curve) and C₃N₅ (red curve). In every case, spiro-OMeTAD was used as the hole transport layer.

Formatted: Highlight

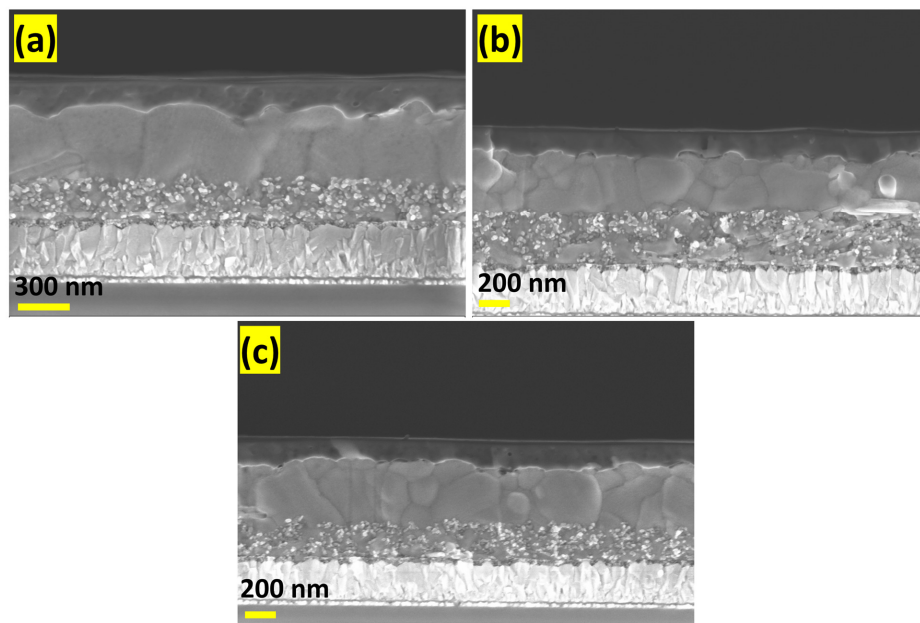


Figure S1820. Cross-sectional FE-SEM images of perovskite solar cell made composed of (a) perovskite layer with bare PbX₂, (b) with 4 wt% of g-C₃N₄ and (c) with 4 wt% of C₃N₅ in PbX₂ solution.

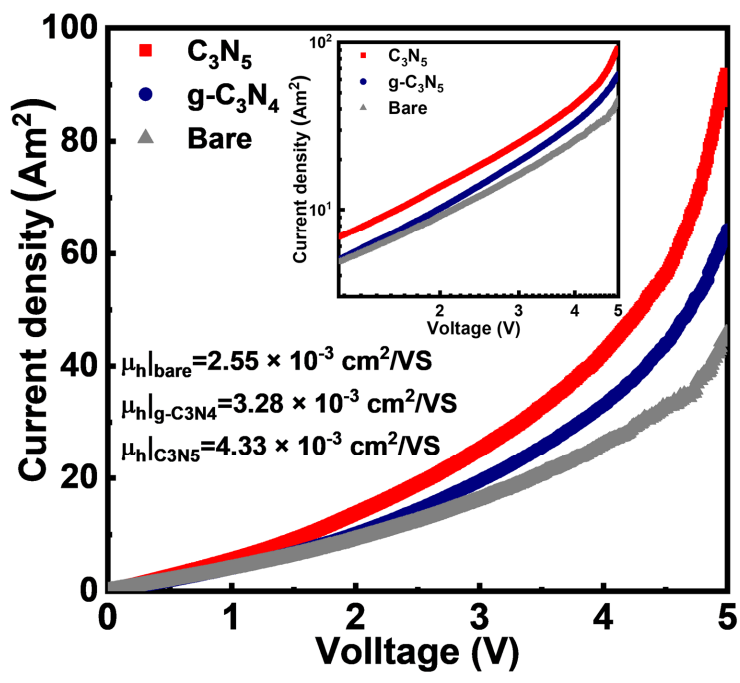


Figure S19. *J-V* curves of hole only device in linear scale (inset is in log-log scale) with the structure of FTO/PEDOT:PSS/Perovskite/Spiro-oMeTAD/Au

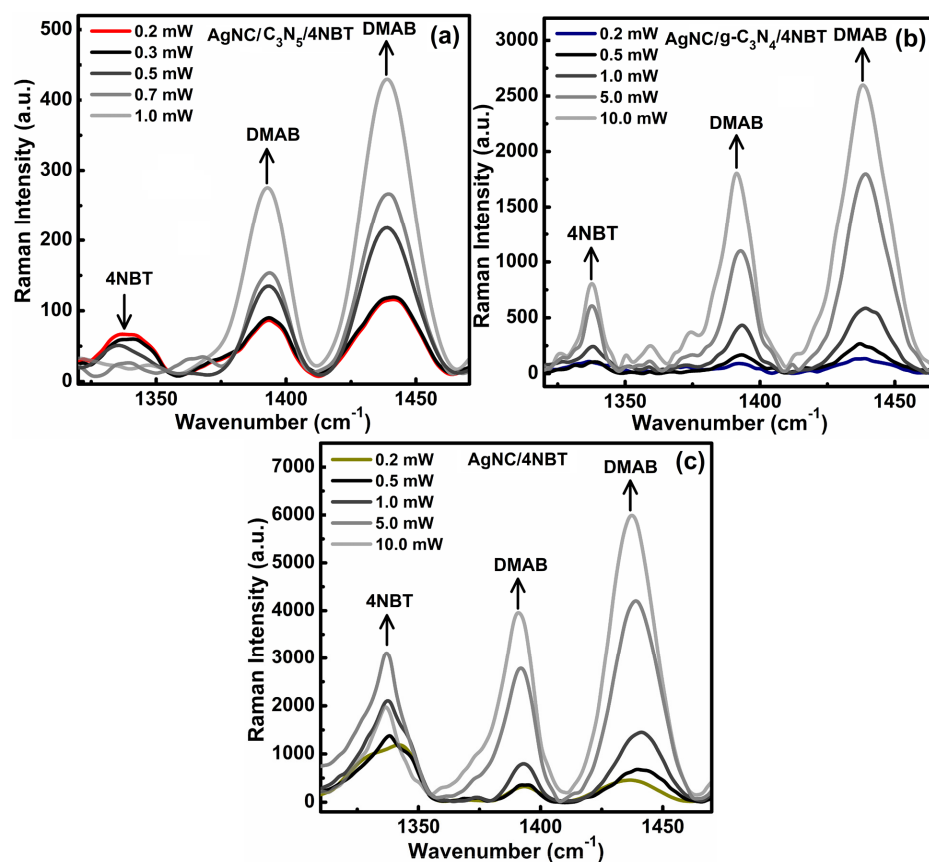


Figure S204. SERS spectra as function of laser power for plasmon-exciton co-induced surface catalytic transformation of 4NBT to DMAB magnified in 1270-1470 cm^{-1} region for (c) AgNC/C₃N₅ and (d) AgNC/g-C₃N₄. The 4NBT peak at 1332 cm^{-1} was decreasing for AgNC/C₃N₅ while increasing for AgNC/g-C₃N₄ as function of laser power and DMAB peaks increasing for both AgNC/C₃N₅ and AgNC/g-C₃N₄. This represent complete transformation of 4NBT to DMAB on AgNC/C₃N₅ even at lower laser power (1.0 mW) and sluggish transformation of 4NBT to DMAB on AgNC/C₃N₅ at high power (10 mW).

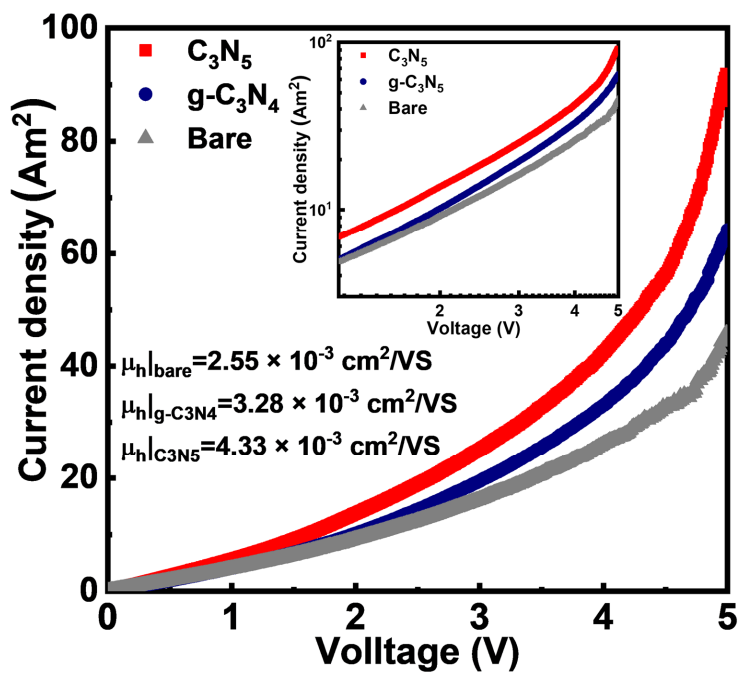


Figure S22. J V curves of hole-only device in linear scale (inset is in log-log scale) with the structure of FTO/PEDOT:PSS/Perovskite/Spiro-OMeTAD/Au

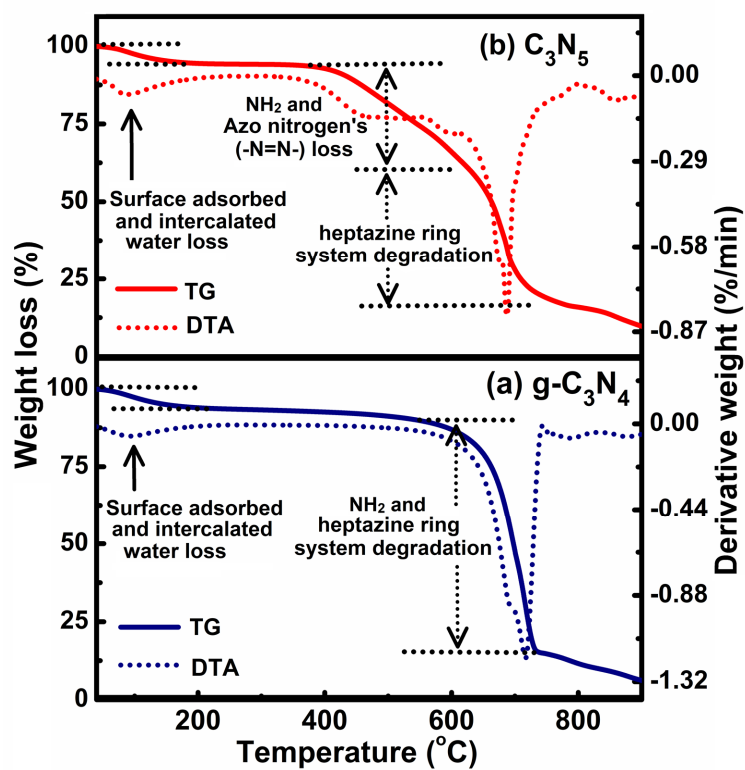


Figure S2113. TGA thermogram of (a) $g\text{-C}_3\text{N}_4$ (blue) showing loss of NH₂ and heptazine ring system and (b) C_3N_5 (red) showing loss of NH₂ and azo nitrogens and heptazine ring system.

Formatted: Not Highlight

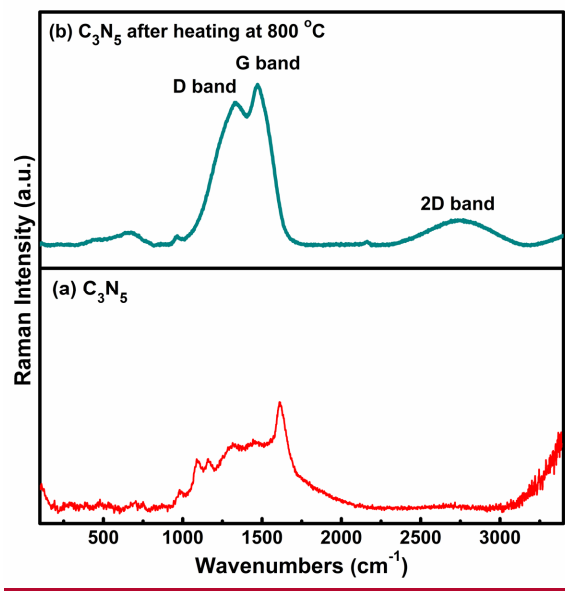


Figure S22. Raman spectra of (a) C_3N_5 and (b) C_3N_5 after annealing at 800 °C in sealed quartz tube showing specific D, G bands and 2D band revealing transformation in N-graphene.

Formatted: Justified, Space After: 0 pt, Line spacing: 1.5 lines, Don't adjust space between Latin and Asian text, Don't adjust space between Asian text and numbers

Formatted: Font: (Default) Times New Roman

References

1. — Pines, A.; Gibby, M.; Waugh, J.; Proton-enhanced nuclear induction spectroscopy. A method for high resolution NMR of dilute spins in solids. *The Journal of Chemical Physics* **1972**, *56* (4), 1776-1777.
2. — Bloch, F.; Nuclear induction. *Physical Review* **1946**, *70* (7-8), 460.
3. — (a) Sattler, A.; Schönberger, S.; Schnick, W.; Melemium Methylsulfonates HC₆N₇(NH₂)₃H₂C₆N₇(NH₂)₃(SO₃Me)₃·H₂O and H₂C₆N₇(NH₂)₃(SO₃Me)₂·H₂O. *Zeitschrift für Anorganische und Allgemeine Chemie* **2010**, *636* (3-4), 476-482; (b) Makowski, S. J.; Köstler, P.; Schnick, W.; Formation of a Hydrogen-Bonded Heptazine Framework by Self-Assembly of Melem into a Hexagonal Channel Structure. *Chemistry - A European Journal* **2012**, *18* (11), 3248-3257.
4. — Saplinova, T.; Bakumov, V.; Gmeiner, T.; Wagler, J.; Schwarz, M.; Kroke, E.; 2, 5, 8-Trihydrazino-s-heptazine: A Precursor for Heptazine-based Iminophosphoranes. *Zeitschrift für Anorganische und Allgemeine Chemie* **2009**, *635* (15), 2480-2487.
5. — Yan, S.; Li, Z.; Zou, Z.; Photodegradation performance of g-C₃N₄ fabricated by directly heating melamine. *Langmuir* **2009**, *25* (17), 10397-10401.
6. — Thakur, U. K.; Askar, A. M.; Kisslinger, R.; Wiltshire, B. D.; Kar, P.; Shankar, K.; Halide perovskite solar cells using monocrySTALLINE TiO₂ nanorod arrays as electron transport layers: Impact of nanorod morphology. *Nanotechnology* **2017**, *28* (27), 274001.
7. — Galińska, A.; Walendziewski, J.; Photocatalytic water splitting over Pt-TiO₂ in the presence of sacrificial reagents. *Energy & Fuels* **2005**, *19* (3), 1143-1147.
8. — (a) Yang, B.; Dyck, O.; Poplawsky, J.; Keum, J.; Paretzky, A.; Das, S.; Ivanov, I.; Rouleau, C.; Duscher, G.; Geohagan, D.; Xiao, K.; Perovskite Solar Cells with Near 100% Internal Quantum Efficiency Based on Large Single Crystalline Grains and Vertical Bulk Heterojunctions. *Journal of the American Chemical Society* **2015**, *137* (29), 9210-9213; (b) Ball, J. M.; Lee, M. M.; Hey, A.; Snaith, H. J.; Low temperature processed meso-superstructured thin film perovskite solar cells. *Energy & Environmental Science* **2013**, *6* (6), 1739-1743; (c) Chaudhary, D. K.; Kumar, P.; Kumar, L.; Evolution in surface coverage of CH₃NH₃PbI₃-XCl_x via heat-assisted solvent vapour treatment and their effects on photovoltaic performance of devices. *RSC Advances* **2016**, *6* (97), 94731-94738.
9. — Siekkinen, A. R.; McLellan, J. M.; Chen, J.; Xia, Y.; Rapid synthesis of small silver nanocubes by mediating polyol reduction with a trace amount of sodium sulfide or sodium hydrosulfide. *Chemical Physics Letters* **2006**, *432* (4-6), 491-496.
10. — Ding, Q.; Shi, Y.; Chen, M.; Li, H.; Yang, X.; Qu, Y.; Liang, W.; Sun, M.; Ultrafast dynamics of plasmon-exciton interaction of Ag nanowire-graphene hybrids for surface catalytic reactions. *Scientific Reports* **2016**, *6*, 32724.
11. — (a) Varghese, O. K.; Grimes, C. A.; Appropriate strategies for determining the photoconversion efficiency of water photoelectrolysis cells: a review with examples using titania nanotube array photoanodes. *Solar Energy Materials and Solar Cells* **2008**, *92* (4), 374-384; (b) Chen, Z.; Dinh, H. N.; Miller, E.; Photoelectrochemical water splitting. Springer: 2013.

Formatted: Font: (Default) Times New Roman

Field Code Changed

1
2
3
4
5
6
7
8
9
10
11
12
13
14
15
16
17
18
19
20
21
22
23
24
25
26
27
28
29
30
31
32
33
34
35
36
37
38
39
40
41
42
43
44
45
46
47
48
49
50
51
52
53
54
55
56
57
58
59
60

|